

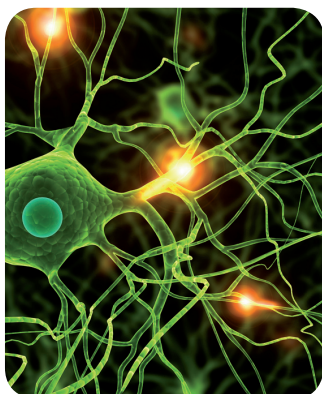
# MÁSTERES de la UAM

Facultad de Ciencias /12-13

Máster en Química  
Teórica y Modelización  
Computacional



**Attosecond  
interferometric  
spectroscopy of  
DES in helium**  
*Álvaro Jiménez Galán*



*“What I cannot create, I do not understand.”*

Richard P. Feynman

## *Acknowledgements*

This work would have never been possible without the effort, support, passion and knowledge of my supervisor. Luca, thank you for your teaching, for your endless patience, for being always accessible and kind and, most of all, thank you for making me love this work. The devotion and enthusiasm you transmit has been a constant motivation for me these last two years.

I also want to thank deeply my boss, Fernando Martín, for the confidence he deposited in me at the beginning, giving me the chance to work in this wonderful group. The clarity in all of his classes and his explanations have been an enormous source of inspiration for me.

I want to acknowledge as well the wonderful people I met at my stay in Paris. In particular, Prof. Alfred Maquet, Prof. Richard Taïeb and Dr. Jeremie Caillat for their hospitality and for giving me the chance to share my work with them, starting what I hope will be a very fruitful collaboration. Special thanks also to Catalin Miron, Pascal Salières and their teams for their amiability in showing me the facilities at Soleil and Saclay and making me feel very welcome.

A word also for the coordinators of the EMTCCM : Manuel Alcamí and Manuel Yáñez, as well as to Beatriz and Wilson for being always there to help with even the silliest problem. Of course, a very special and important thanks to all my friends from the master : Oriana, David, Juanjo, Estefanía, Patricia, Darek and Kathy, as well as to the actual and former habitants of the 501-A office: Lara and Ane. Thank you all for being such wonderful people and for making this job one of the most special and rewarding jobs anyone could hope for! Finally, I want to thank all the people I met from the Chemistry department at the Universidad Autónoma de Madrid, those who are still here and those who have left.

The research leading to these results has received primary funding from the ERA-Chemistry network under the project title “Visualización y control de la dinámica molecular electrónica en la escala de los attosegundos” (Ref.PIM2010EEC-00751) through the organism MINECO, to whom I express my gratitude. It has also received partial funding from the European Research Council under the European Union’s Seventh Framework Programme (FP7/2007-2013)/ERC grant agreement n° 290853.



**ERACHEMISTRY**



# *Original Contributions*

My original contributions to this master thesis can be summarized as follows:

- Implementation of the code that generates the Soft Photon Approximation (used in Sec.4.1).
- Implementation of the analytical two-photon perturbative model with intermediate autoionizing states (Sec.3.5.1).
- Implementation of the code for the above model (used in Sec.4.2.4.2).
- Use of the *ab-initio* code developed by Dr. Luca Argenti that solves the TDSE for the helium atom applying it to the cases of interest.
- Implementation of basic programs to extract different parameters from the above code (e.g., the phase shift).

# Contents

<b>Acknowledgements</b>	<b>ii</b>
<b>Original Contributions</b>	<b>iii</b>
<b>1 Introduction</b>	<b>1</b>
1.1 Generation of attosecond pulses. . . . .	2
1.2 Attosecond pulse metrology. . . . .	4
1.2.1 Attosecond pulse trains. The RABITT technique. . . . .	4
1.2.2 Single attosecond pulses. Streaking. . . . .	7
1.3 Atomic and molecular attosecond spectroscopy. . . . .	7
1.3.1 Autoionizing states. . . . .	8
1.3.2 Correlation and photoejection time delays. . . . .	8
1.4 Aim and outline of the thesis. . . . .	10
<b>2 Ab-initio theory</b>	<b>12</b>
2.1 Electrostatic field-free hamiltonian. . . . .	15
2.1.1 Symmetry and spin considerations. . . . .	15
2.1.2 Correlation in doubly excited states. . . . .	16
2.2 Close coupling basis. Eigenfunctions of the system. . . . .	20
2.2.0.1 Asymptotic limit of the wavefunction and Wigner time delay. . . . .	22
2.2.1 Extraction of photoelectron distributions. . . . .	22
2.2.1.1 Calculation of the scattering states. The K-matrix method.	22
2.3 Solution of the TDSE. . . . .	24
2.3.1 Interaction with an electromagnetic field. The minimal coupling hamiltonian. . . . .	25
2.3.2 Time evolution of the wavefunction. . . . .	27
2.3.2.1 Splitting scheme . . . . .	29
2.3.2.2 The Krylov method. . . . .	29
2.3.3 Absorption potential. . . . .	30
2.3.4 Extraction of photoelectron distributions. Projection on scatter- ing states. . . . .	31
<b>3 Theory models</b>	<b>32</b>
3.1 Volkov states. . . . .	33
3.2 The soft photon approximation. . . . .	34

3.2.1	Monochromatic soft-photon approximation. . . . .	35
3.2.2	Pulsed soft-photon approximation. . . . .	37
3.2.3	Frequency-comb limit. . . . .	39
3.3	Perturbation theory for RABITT . . . . .	42
3.3.1	RABITT for non-resonant intermediate states. . . . .	42
3.4	Fano model of autoionization. . . . .	42
3.5	Two photon perturbative model with intermediate autoionizing states. . .	44
3.5.1	Model. . . . .	45
3.5.2	Monochromatic vs Finite pulses. . . . .	48
<b>4</b>	<b>Results</b>	<b>49</b>
4.1	SPA to reproduce uncorrelated dynamics. . . . .	49
4.1.1	Single attosecond pulse case. . . . .	49
4.1.2	Attosecond pulse train case; effect of finite probe duration. . . . .	52
4.1.3	Attosecond pulse train case; effect of high probe intensity. . . . .	55
4.2	RABITT for the study of doubly excited states. . . . .	57
4.2.1	Intermediate bound state. . . . .	57
4.2.2	Measurable phase shift. . . . .	58
4.2.3	Photoelectron Angular Distributions. . . . .	61
4.2.4	Transitions with an intermediate resonant state. . . . .	62
4.2.4.1	Ab-initio simulations. . . . .	63
4.2.4.2	Monochromatic Model. . . . .	65
4.2.4.3	Separated pulses. . . . .	75
<b>5</b>	<b>Conclusions and perspectives</b>	<b>77</b>
<b>A</b>	<b>Monochromatic two photon perturbative model</b>	<b>79</b>
A.1	Scalar product of plane and spherical waves . . . . .	79
A.2	Explicit derivation . . . . .	80
A.2.1	CC matrix element . . . . .	80
A.2.2	CM matrix element . . . . .	81
A.2.3	CB matrix element . . . . .	82
A.2.4	MC matrix element . . . . .	82
A.2.5	MM matrix element . . . . .	84
A.2.6	MB matrix element . . . . .	85
A.2.7	BC matrix element . . . . .	86
A.2.8	BM matrix element . . . . .	86
A.2.9	BB matrix element . . . . .	87
	<b>Bibliography</b>	<b>88</b>

# Chapter 1

## Introduction

Imagine an extraterrestrial race that wants to study and control the human behaviour. Now imagine that this extraterrestrials can only interpret the images that get to their brains not in a time scale of several milliseconds like us, but of thousands of years. It is clear that this outer world race will know very little of our everyday life, and can seldom alter the course of our lives. If this race wants to study us in detail and ultimately control us, it needs to operate in our time scale. This is more or less what happens between electrons and us. The characteristic beating period of the ground state (1s) and first excited state (2p) of hydrogen is  $T = 2\pi/\omega_{2p-1s} = 24$  attoseconds. Electrons, thus, move in the time scale of attoseconds. Seven attoseconds are to one second what one second is to the age of the Earth. In our time scale, it is impossible to have a deep knowledge of how electrons move, they are just too fast. We still can affect the electron motion by perturbing it at uncontrolled stages of its evolution. In this case, we will still be able to see a final effect induced by such incoherent perturbation (the asymptotic limit). However, we will be unable to monitor or alter any given intermediate passage selectively. It is the information in these intermediate steps that has only recently started to be revealed with the advent of the so-called attosecond physics. Needless to say that a deep understanding of these dynamics will be essential to achieve control over electrons in atoms, molecules and nanodevices.

Ever since its theoretical explanation in 1905 [1], the photoelectric effect has been a major tool to study the structure and properties of atoms and molecules. Ordinary spectroscopic techniques in the stationary regime have been able to provide many information on electron dynamics interacting with light at an unprecedented level of detail thanks to high resolution x-ray sources [2] used in conjunction with advanced photofragment detection techniques such as velocity map imaging (VMI) [3] , COLTRIMS [4], time of

flight detectors (TOF) [5] or magnetic bottle coincidence spectrometers [6]. Observables such as the position and width of resonant peaks, for example, which indicate the energy and lifetime of transiently bound states, can be accurately measured. With these techniques it is also possible to retrieve molecular structure by exploiting effects such as Cohen Fano interference [7, 8] and intramolecular scattering [9, 10]. Such stationary methods, however, which rely on one-photon processes, cannot give a complete picture of the electron dynamics. This is because the full quantum mechanical information of a particle's dynamics is encoded not only in the absolute value of the wave function, but also in its phase, while one-photon time independent techniques are insensitive to the relative phases of transition amplitudes; hence, any information on coherent dynamics is lost. To recover this information, therefore, it is necessary to go beyond the absorption of a single photon and consider multiphoton or even non-perturbative processes instead. Furthermore, to extract any meaningful information on the phases of the system, the spectral and phase properties of the electromagnetic radiation used to induce the radiative transitions need to be fully characterized to start with. Lastly, these multiphoton transitions must occur on a time scale comparable to that of the electronic movement they are meant to highlight. All of these requisites are realized by novel attosecond pump-probe techniques [11].

## 1.1 Generation of attosecond pulses.

Electromagnetic pulses with the aforementioned characteristics have become accessible with the advent of phase-locked pulsed lasers like Ti:Sapphire [12]. These lasers are able to produce coherent light pulses at intensities of the order of  $I = 10^{16}$  W/cm<sup>2</sup>. When an atom or molecule interacts with electromagnetic fields that reach intensities comparable to the coulomb force that binds the electron in the atom ( $I \approx 1 \text{ a.u.} = 3.509 \cdot 10^{16} \text{ W/cm}^2$ ), a series of short and energetic electromagnetic pulses are created. This process is known as high harmonic generation [13], and it can be described classically with the three-step model [14]. According to the model, in the first step, the intense electromagnetic field distorts the Coulomb attractive potential, creating a barrier through which the electron can tunnel to the continuum. In the second step, the free electron is driven apart from the ion by the external field; as the field changes sign, the electron can invert its trajectory and be driven back to the ion, gaining a large kinetic energy. Lastly, the electron recollides with the initial parent ion, liberating the acquired energy in the form of a short electromagnetic pulse. This process is repeated every half period of the field, so that a coherent series of pulses are created. These pulses are separated by half the period of the electromagnetic field, thus forming a train of pulses, each with a duration

that is a small fraction of the field period. Due to the even spacing and alternating sign of the pulses in the train, only odd harmonics of the initial electromagnetic frequency are created. The intensity of the high harmonic spectrum reaches a plateau up to a maximum energy of  $E = 3.17U_p + I_p$ , where  $U_p$  is the ponderomotive energy of the field and  $I_p$  is the ionization potential of the atom or molecule. After the plateau, the spectrum drops off exponentially. The ponderomotive energy  $U_p$ , which is the mean kinetic energy of a free electron in the external field, is related to the field amplitude  $E_0$  and frequency  $\omega$  through the expression  $U_p = E_0^2/4\omega$ . The access to infrared pulsed lasers with intensities on focus as high as  $10^{15}$  W/cm<sup>2</sup> and a duration of 5 to 30 fs [15] permitted to generate short trains or even isolated extreme-ultraviolet (XUV) pulses with a duration of the order of 100 as [16, 17]. Such characteristics make high harmonic generation an ideal candidate to study electronic excitation and ionization in atoms and molecules (XUV range) at their intrinsic timescale (attoseconds). This is done with pump-probe techniques, in which both the generating IR laser and the XUV pulse (or pulse train) are used in conjunction. In these techniques, after the generation process, the XUV field is separated from the IR laser field, while a replica of the latter travels through an alternative optical path with a controllable time delay with respect to the path followed by the high harmonic light. In this way, it is possible to subsequently collimate the XUV and the IR pulses with any desired time delay within an accuracy of few attoseconds. Application of these techniques lead, to name a few, to the first movie of valence shell excited electronic states [18], to the time resolved study of the Auger cascade following the core ionization of rare gases [19, 20], to the monitoring of valence shell electron motion in Krypton ions [21] or to steer electronic motion [22, 23].

High harmonic generation is not an easily reproducible process. In particular, it is not granted that the high harmonics generated in the recollision combine to form an APT. For this to occur, the individual harmonics of the pulses must be in phase at some point in space and time (see Fig.(1.1)), and this circumstance cannot be ascertained by looking at the one-photon ionization spectrum alone, which only provides a measure of the intensity of the harmonics. Even if by virtue of the recollision mechanism, the harmonics are initially generated in phase, when the radiation passes through the filter in order to cut the lower frequency components and isolate the XUV frequency, the harmonics can lose their synchronization. To characterize the coherent pulse-train nature of the radiation, techniques such as frequency resolved optical gating (FROG) [24] and reconstruction of attosecond beating by interference of two photon transitions (RABITT) [25] were proposed. This latter technique proved useful not only to characterize high harmonic radiation, but also to study the electron dynamics. Indeed, RABITT forms the basis of the interferometric photoelectron techniques we devised in this thesis to investigate the ultrafast response of correlated electron dynamics to external pulses. Thus, the following

is devoted to illustrate this technique and how it can be used to extract information on radiative transitions in matter.

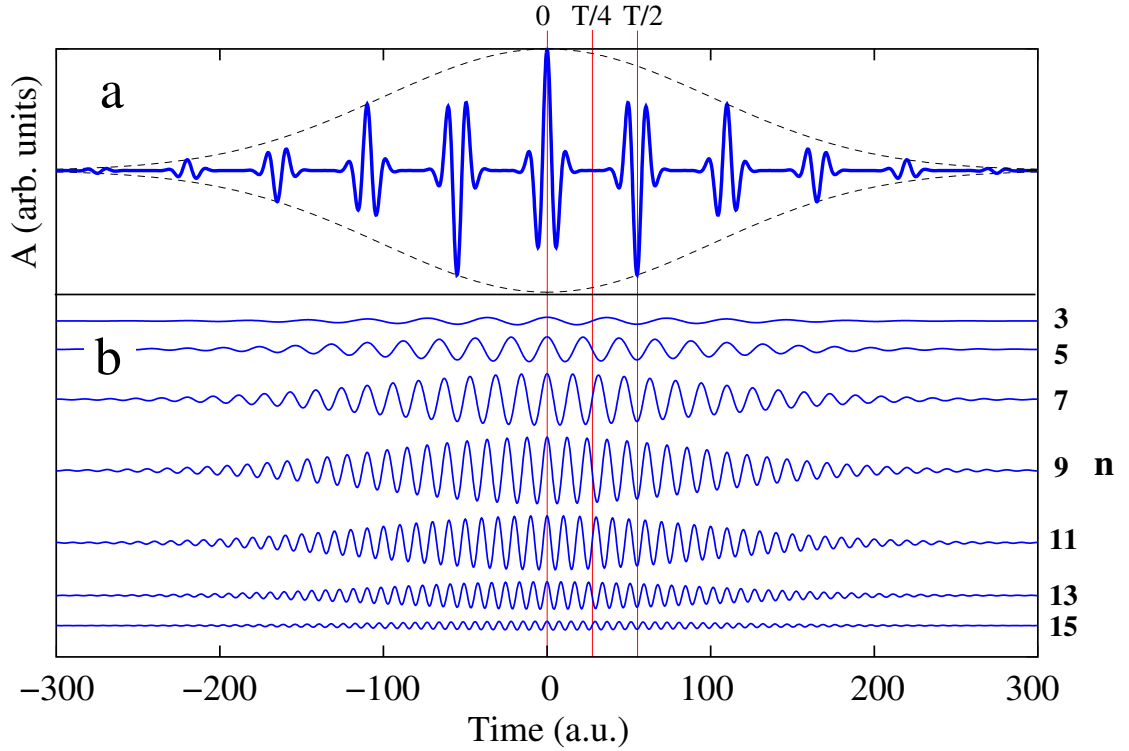


FIGURE 1.1: Schematic representation of an APT (a) and of its harmonic composition (b). When the harmonics are all in phase at a given point along their trajectory, they interfere constructively giving rise to a localized attosecond pulse ( $t=0$ ). At a distance of half an IR cycle  $T_{IR}/2$  in either space or time from this maximum, all the harmonics will be in phase again but with opposite sign, thus giving rise to a second attosecond pulse which is the mirror image of the first one with respect to the horizontal axis. At  $t = T_{IR}/4$ , all harmonics vanish and so does the train.

## 1.2 Attosecond pulse metrology.

### 1.2.1 Attosecond pulse trains. The RABITT technique.

In this technique, the isolated attosecond pulse train is superposed, with a controlled time delay, to a weak replica of the IR pulse used to generate it and employed to ionize a rare gas. Due to the weakness of both the XUV train and the IR pulse, the ionization process can be described at the level of the lowest order perturbation theory.

In absence of the IR, the XUV train alone will create a series of odd harmonic peaks at the photoelectron kinetic energies  $(2n + 1)\omega_{IR} - IP$ . This is a one-photon process and can be accounted for with a first order perturbative approach.

When the IR is present, two photon transitions corresponding to the absorption of

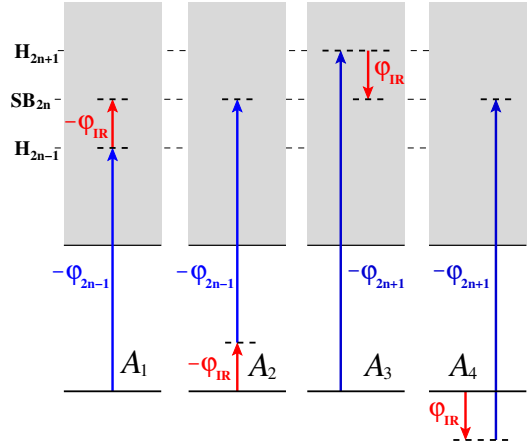


FIGURE 1.2: The four lowest-order two-photon transition amplitudes that give rise to the sideband  $2n$  in the RABITT scheme. Since both the absorption and stimulated emission of one photon carry the phase of the corresponding field, but with opposite signs, interference terms of the form  $\mathcal{A}_{1,2}^* \mathcal{A}_{3,4} + C.C.$  oscillate as  $2\varphi_{IR} = 2\omega_{IR} t_d$ , where  $t_d$  is the time delay between the IR pulse and the APT.

one XUV photon and to the exchange of one IR photon take place. As a consequence, photoelectron signals at energies  $2n\omega_{IR} - \text{IP}$ , the so-called sidebands, also appear. These sidebands are related to both the relative phase of the harmonics in the XUV train and to the intrinsic phases of electronic transitions involved.

Following standard lowest-order time-dependent perturbation theory [26], the total two-photon transition amplitude  $\mathcal{A}_{2n}^{(2)}$  giving rise to the sideband  $2n$  in the RABITT pump-probe scheme is the sum of the amplitudes for the four diagrams depicted in Figure 1.2, and can be readily written as

$$\begin{aligned} \mathcal{A}_{2n}^{(2)} &= \mathcal{A}_1 + \mathcal{A}_2 + \mathcal{A}_3 + \mathcal{A}_4 = \\ &\approx \frac{\pi}{2i} (A_{2n-1} A_{\text{IR}} \mathcal{M}_{2n-1} + A_{2n+1} A_{\text{IR}}^* \mathcal{M}_{2n+1}) \delta_T(E - \omega_g - 2n\omega). \end{aligned} \quad (1.1)$$

In (1.1) we introduced the two-photon transition matrix elements  $\mathcal{M}_{2n\pm 1}$  for the absorption of the  $2n \pm 1$  harmonics,

$$\mathcal{M}_{2n\pm 1} = \langle E | P [G_0^+(\omega_g \mp \omega) + G_0^+(\omega_g + \omega_{2n\pm 1})] P | i \rangle. \quad (1.2)$$

where  $|i\rangle$  is the initial state of the atom,  $|E\rangle$  is a final state in the continuum with appropriate symmetry,  $G_0^+(\omega) = (\omega - H_0 + i0^+)^{-1}$  is the retarded resolvent of the field-free atomic hamiltonian, and  $P$  is the total electronic canonical momentum along the field polarization axis (we assume collinear polarization for all the external fields). The two-photon transition matrix elements are complex quantities; their argument is known as *atomic phase*,  $\varphi_n^{\text{At}} = \arg \mathcal{M}_n$ . The factors  $A_{\text{IR}}$  and  $A_{2n\pm 1}$  are the peak amplitude of the vector potential of the IR and of the two harmonics. Finally, the special function

$\delta_T(\omega)$  is defined as

$$\delta_T(\omega) = \frac{\sin \omega T/2}{\pi \omega}, \quad \lim_{T \rightarrow \infty} \frac{2\pi}{T} \delta_T^2(\omega) = \delta(\omega). \quad (1.3)$$

The integral transition rate to a given sideband  $2n$ , therefore, is given by

$$\mathcal{W}_{2n}^{(2)} = \frac{1}{T} \int dE \left| \mathcal{A}_{2n}^{(2)}(E) \right|^2 = \frac{\pi}{8} |A_{2n-1} A_{\text{IR}} \mathcal{M}_{2n-1} + A_{2n+1} A_{\text{IR}}^* \mathcal{M}_{2n+1}|^2. \quad (1.4)$$

If we use the attosecond pulse train as a reference to define the temporal scale, and thus keep it fixed with respect to the time delay, then the phases of the harmonics field amplitudes do not change with the time delay, while the phase of the IR, which we can here assume to be very long, is linear with the time delay:

$$A_{2n\pm 1} = |A_{2n\pm 1}| e^{-i\phi_{2n\pm 1}}, \quad A_{\text{IR}} = |A_{\text{IR}}| e^{-i(\varphi_{\text{IR},0} + \omega\tau)}. \quad (1.5)$$

Inserting these latter parametrizations in the expression (1.4) for the transition rate to the sideband, and expressing the module of the vector potential amplitude in terms of the photon flux  $\Phi$

$$|A| = \frac{\sqrt{8\pi\Phi c}}{\omega}, \quad (1.6)$$

we finally get

$$\begin{aligned} \mathcal{W}_{2n\omega}^{(2)} &= \frac{8\pi^3}{\omega_{\text{IR}}} \Phi_{\text{IR}} \left\{ \Phi_{2n-1} |\mathcal{M}_{2n-1}|^2 + \Phi_{2n+1} |\mathcal{M}_{2n+1}|^2 + \right. \\ &\quad \left. + 2\sqrt{\Phi_{2n-1}\Phi_{2n+1}} |\mathcal{M}_{2n-1}\mathcal{M}_{2n+1}| \cos [\Delta\phi_{2n} + \Delta\varphi_{2n}^{\text{At}} - 2(\varphi_{\text{IR},0} + \omega_{\text{IR}}\tau)] \right\}, \end{aligned} \quad (1.7)$$

where  $\Delta\phi_{2n} \equiv \phi_{2n+1} - \phi_{2n-1}$  and  $\Delta\varphi_{2n}^{\text{At}} = \varphi_{2n+1}^{\text{At}} - \varphi_{2n-1}^{\text{At}}$ . If the properties of the ionization continuum do not change much across the energy span of few  $\omega$ 's, as it is generally the case for rare gases in the energy region far from the ionization threshold, on the one side, and far from autoionizing states, on the other side, then the two integrals  $\mathcal{M}_{2n+1}$  and  $\mathcal{M}_{2n-1}$  are similar both in absolute value and in phase. In particular, the atomic phase can be accurately linearized across the whole energy interval:  $\varphi_{2n-1}^{\text{At}} - \varphi_{2n+1}^{\text{At}} \simeq 2\omega_{\text{IR}} \partial_E \varphi_E^{\text{At}}$ . As a result, the phase of the sideband can be written as

$$\Phi_{2n} = \phi_{2n+1} - \phi_{2n-1} - \varphi_{\text{IR},0} - 2\omega_{\text{IR}} \partial \varphi_E^{\text{At}} / \partial E. \quad (1.8)$$

Both the absolute value of the IR phase and the (typically small) value of the atomic phase change are unknown constants. If these constants are known, then the individual differences  $\phi_{2n+1} - \phi_{2n-1}$  can be determined and, from these, by means of an inverse discrete Fourier transform, the envelope of each pulse within the train can be determined. Even if the absolute value of the IR phase or the energy derivative of the atomic phase

are unknown, it is still possible to determine the average shape of the envelope of an attosecond pulse in the train, and in particular its duration, from all the values of  $\Phi_{2n} - \Phi_{2n-2}$ .

RABITT spectroscopy was first used to characterize the structure of the attosecond train by assuming slowly varying continuum-continuum atomic matrix elements [27–29] and, in turn, devise manipulation techniques to minimize the duration of individual pulses [30, 31]. Alternatively, one can assume that the pulse characteristics are known and use RABITT to extract information on the underlying electron dynamics instead. This latter approach has already been applied to study the role of discrete intermediate states in the two-photon single ionization of helium [32] and that of intershell correlation effects in the valence photoionization of argon [33]. Therefore, the RABITT technique lends itself naturally to the study of radiative transitions within the ionization continuum which are not easily accessible with standard stationary photoelectron spectroscopies.

### 1.2.2 Single attosecond pulses. Streaking.

With the most recent experimental advances in laser technology, it is now possible to generate isolated single attosecond pulses (SAP) [16, 17, 34]. SAP provide access to a method to study atomic and/or molecular ionization dynamics called *streaking*, which consists in the photoionization of atoms or molecules by a single attosecond pulse in the presence of an intense IR field. As opposed to the perturbative regime in which RABITT works, streaking techniques are in the so-called strong field regime. Interpretation of the results now comes from a purely classical picture, or from non-perturbative quantum models such as the strong field or soft photon approximations. The idea of the technique is the following: a single attosecond XUV pulse ionizes the sample, populating a wide energy spectrum. When the IR is present, the photoelectrons will receive a momentum shear proportional to the vector field of the IR, according to the classical formula  $\Delta\vec{p} = -\alpha\vec{A}_{IR}(t)$ . Depending on the time delay between the two pulses, the momentum shift will have different values. In this way, one can achieve control over photoelectron ejection processes [22, 35].

## 1.3 Atomic and molecular attosecond spectroscopy.

In the past years, attention has shifted from the creation of novel ways to obtain and characterize attosecond pulses towards the use of these pulses to monitor and control electron dynamics, following the path of what was done with reaction dynamics in molecules with femtosecond lasers [36–38]. Part of the electron dynamics can be understood with single particle approximation methods. However, a lot is governed by electron correlation,

which occurs in the timescale of attoseconds. One of the most dramatic evidence of such correlation is autoionization, the process in which electron interaction leads to the spontaneous emission of one electron from a transiently bound state.

### 1.3.1 Autoionizing states.

Autoionizing states have been the subject of extensive investigation since Madden and Codling reported the asymmetric profile of helium doubly excited states in the first energy-resolved x-ray photoabsorption spectrum recorded using synchrotron radiation, a pioneering experiment which signed the birth of modern photoelectron spectroscopy [39]. Several years before, Fano had developed a model [40, 41] in which he explained the asymmetric profiles seen by Madden and Codling as interferences between two one-photon paths, one direct (ground-continuum) and another indirect (ground-bound-continuum). Synchrotron radiation gave access to the study of one-electron processes with unprecedented detail; the width and energy of several autoionizing states have been firmly established. Due to the characteristic properties of synchrotron radiation (incoherent highly monochromatized pulses with a duration of several picoseconds), the majority of available studies involving doubly excited states are based on one-photon stationary processes. With the advent of the highly intense laser technology, some authors addressed the problem of multiphoton transitions involving autoionizing states when in the presence of such strong laser fields [42]. These studies, however, are mostly based on formalism appropriate to long and/or incoherent laser fields which are not readily applicable to the recent time resolved techniques described in the previous section.

### 1.3.2 Correlation and photoejection time delays.

One important aspect that so far can only be studied with time resolved spectroscopy is photoejection time delays, i.e., the time it takes an electron to be ejected from a given localized state of the atom after absorbing a photon [43]. Photo-ejection time delay has gained much prominence lately due to its connection with electronic correlation. Schultze *et al.* conducted an attosecond streaking pump-probe experiment in which they measured the difference in the ejection time delay between the  $2s$  and  $2p$  shells of neon, finding that when the electron is released from the latter, the process takes 20 as longer [44]. Part of this delay is associated to the effective potentials the electron feels, and can be accounted for already in the independent particle approximation. Part is induced by the measurement itself, which uses a strong infrared field that perturbs the electron dynamics. Even when these effects are taken into account, though, a considerable residual delay remains. One possible cause of the time delay not explained by the single particle

approximation is the relaxation process that the non-ejected electrons undergo when one of the electrons is removed. This relaxation consists on a fast rearrangement of the electrons in the atom (normally of the order of few tens of attoseconds) [45]. When the ejection of the photoelectron takes place on a timescale comparable to the relaxation time, the two processes can influence each other: in figurative terms, the rearranging electrons *kick out* the photoelectron. This dynamical correlation can be measured as a time delay in the photoelectron emission.

In streaking, the time delay is measured as the separation between the baricenter of the photoelectron signals from different shells. In the case of rare gas ionization, however, the RABITT technique also proved useful to measure photoemission time delay. In this case, the time delay can be related to the atomic phase of the sideband signal as  $\tau_{at} = \phi_{2n}^{at}/2\omega$ . There is a close relation with the time delay measured in this way, the photoejection time delay and the time delay [43, 46, 47] experienced by a particle in elastic scattering. The latter is known as Wigner time delay, which is proportional to the derivative of the scattering phase shift with respect to energy and is thus a field-free quantity. In the case of uncoupled channels and under the assumption that all the relevant atomic matrix elements change smoothly across the energy separation between two sidebands, it has been shown [48] that the time delay  $\tau_{at}$  recorded with the RABITT technique incorporates two contributions,  $\tau_{at} = \tau_W + \tau_{CC}$ , the Wigner time delay  $\tau_W$  of the one-xuv-photon ionization and an additional continuum-continuum term  $\tau_{CC}$  due to the exchange of a photon between the atom and the IR field.

So far, most of the investigation on continuum-continuum transitions and photo-ejection time delays concentrated on energy regions where metastable states did not appear. However, transiently bound states are an important aspect of ionization dynamics and their influence on two photon transitions in the continuum and on photo-ejection time delays is still widely unexplored. Occasional discrepancies between existing experimental data and state-of-the-art theories for poly-electronic atoms [33, 49] indicate that accurate ab-initio investigation of smaller systems are still required to shed light on the relation between electronic correlation in the continuum and time delay. Helium is an ideal candidate in this respect, because it features most of the aspects of electronic correlation while permitting a virtually exact treatment from both a perturbative time-independent and a time-dependent point of view. In fact, a few works in these directions have already made their appearance in the literature [50–52]. Secs.3.5.1, 4.2.4.1 and 4.2.4.2 of this thesis will be devoted to investigate the effect of autoionizing states on the photoejection time delay in helium. It should be emphasized that the temporal features of the photoeffect indicated above, associated to either single particle or to correlated dynamics, are general. Most of the conclusions drawn for helium can thus be extended

to other multielectronic atoms. In larger systems, of course, many-body effects not observed in helium (e.g., Auger cascades) may appear as well.

## 1.4 Aim and outline of the thesis.

This thesis is aimed at explaining the coherent and time-resolved correlated electron dynamics in helium that are triggered, monitored and controlled with modern attosecond laser technologies. In particular, we propose the validity of the novel attosecond techniques previously described to analyze the role of autoionizing states in two-photon transitions in the continuum. We do so in two ways: with ab-initio calculations that come out from the exact numerical solution of the Time Dependent Schrödinger Equation [53], and with simplified models.

To isolate the background single-particle effects from those with many-body character, we extended the soft photon model [54], which is based on a single particle approximation, to treat realistic pulses both for streaking and RABITT techniques. With this tool, we studied in detail several effects of these techniques that could possibly lead to unexpected results, such as the pulse duration or the intensity of the fields. In this way, when the model is compared to the full ab-initio result, we can fully isolate the effects due uniquely to electronic correlation.

We then propose the RABITT technique as a valid candidate to give insight on the role of autoionizing states in continuum-continuum transitions by extracting information from the sideband phases in the photoelectron spectrum.

Finally, a parametrized model was developed that permits us to quantitatively predict the transition matrix elements of continuum-continuum transitions involving autoionizing states and relate it with a physical observable, i.e., the phases of the sidebands in the RABITT spectrum, which, as we mentioned, can be linked to the photo-ejection time delay. Used in conjunction with the experiment, this model will help shed light on correlated dynamics in the continuum.

The simulations were particularized to the multiphoton transitions occurring in the single ionization channel of the helium atom as a consequence of the interaction with a perturbative extreme ultraviolet (XUV) pulse or pulse train and an intense infrared (IR) field. Both pulses were used in conjunction and time delayed accordingly in order to reproduce the features of the pump-probe experiments described.

This thesis is structured as follows. In Chapter 2, we give an overview of the helium atom, introducing the hamiltonian of our system, and we describe the main characteristics of the ab-initio code used. Chapter 3 focuses on the description of the models that were developed: the extensions of the soft photon model and the two photon perturbative model with intermediate autoionizing states. Chapter 4 is dedicated to the

analysis of some characteristic attosecond pump-probe processes reproduced with direct ab-initio simulations and interpreted with the help of simplified models. Finally, we draw conclusions and future prospects and aims of this work.

## Chapter 2

# Ab-initio theory

“... it may happen that small differences in the initial conditions produce very great ones in the final phenomena. A small error in the former will produce an enormous error in the latter. Prediction becomes impossible, and we have the fortuitous phenomenon.”

[H. Poincaré, 1903]

Helium is the second lightest element and the smallest system featuring electronic correlation. Composed of two electrons and a nucleus, it has been a benchmark for correlation studies due to the fact that it is one of the few systems that can be solved numerically in a virtually exact way. Theoretical support can thus be used to explain accurately the different features seen in spectroscopic measurements and which are characteristic of a many-body system, like Auger decay and multiple-channel opening. Furthermore, helium is the quantum paradigm of the three body system, which is a non-integrable and, thus, classically chaotic system. Numerical methods are hence necessary for a full solution of an interacting three-body-system helium. If we neglect the interaction between the two electrons, the helium energy spectrum will be given by the sum of the spectra of two independent hydrogen atoms with an effective nuclear charge  $Z = 2$ . In particular, the bound part is

$$E_{N,n} = -\frac{Z^2}{2} \left( \frac{1}{N^2} + \frac{1}{n^2} \right). \quad (2.1)$$

where  $N = 1, 2, \dots$ , and  $n = N, N + 1, \dots$  are the principal quantum number of the two electrons, while the branches of the single-ionization continuum are

$$E_{N,\epsilon} = -\frac{Z^2}{2} \frac{1}{N^2} + \epsilon. \quad (2.2)$$

The smallest quantum number  $N$  indicates the principal quantum number of the  $\text{He}^+$  parent ion, while  $n$  indicates the excitation level of the outer electron. The non-interacting bound states thus form Rydberg series converging to the ionization thresholds of the  $\text{He}^+$  ion, in analogy with hydrogen. In (2.1), the energies below the  $N = 1$  threshold in particular, correspond to singly excited states, in which one electron remains in the ground state and the other electron is excited into a higher bound state. In absence of electronic repulsion, the  $1S^e$  ground-state energy is -4 a.u., well below the well-known Hartree-Fock limit of -2.86168 a.u. The huge difference between the two numbers is due to the mean interelectronic repulsion. In the presence of electron interaction, singly excited states can be treated as hydrogenic states in which the excited electron feels an asymptotic effective charge of  $Z_{ef.} = 1$  due to the shielding effect of the core electron. However, due its quantum nature, the electron can penetrate this shielding barrier. As a result of this short-range interaction, the energy levels are collectively shifted with their energy corrected by a quantity known as the quantum defect  $\mu$ ,

$$E_n = -\frac{1}{2(n - \mu)^2}, \quad (2.3)$$

which accounts for this effect.

Let us consider now the Rydberg series in the non-interacting electron model converging to the higher thresholds. Due to the large value of the first excitation energy of the parent ion ( $E_{N=2} - E_{N=1} = 1.5$  a.u.), even in the hypothetical case in which the interelectronic repulsion were absent, an infinite set of Rydberg series of bound states embedded in the continuum arises: the so-called doubly excited states (DES), in which both electrons are promoted out of the  $1s$  orbital of the ground state (see Fig.(2.1)). This circumstance remains true within the less drastic model of a mean-field single-particle approximation (e.g., those based on the Hartree-Fock model for the ground state). Due to interelectronic repulsion, energy displacements similar to those described for singly excited states alter the position of doubly excited states. Yet, this displacement is small with respect to the  $N=2 - N=1$  excitation energy. In the case of the ground state, if no mean-field approximations are made, the energy drops to the electrostatic limit -2.90372 a.u. This second change is due to *electron correlation*, i.e., to the fact that the wave function cannot be expressed as a single determinant. If for truly bound states, correlation manifests itself only in the form of a real energy shift, in the case of doubly excited states, it induces a strong mixing between DES (that we call long-range correlation) as well as a mixing between DES and continuum (short-range correlation) which causes the states to become unstable and decay spontaneously in a process known as autoionization or Auger decay. A second distinctive feature of multielectron atoms, if compared to hydrogenic atoms or single-active electron models, is channel-opening. Above  $N=2$ , for any given total symmetry, the asymptotically-free electron can be associated to several different states

of the parent ion, e.g.,  $1S$ ,  $2S$ ,  $2P$ . Furthermore, since the parent ion is not necessarily totally symmetric, the symmetry of the free electron is in general not fixed either. In particular, for  $N=2$ , the bound electron can be in any of the following  $(n, \ell)$  states :  $(1,0)$ ,  $(2,0)$ ,  $(2,1)$ . Thus, depending on the total symmetry of the system, the free electron can have, at least, two more opened channels (see Fig.(2.1)). As we go higher in energy and the value of the principal quantum number  $N$  increases, so do the number of open channels. For  $N \rightarrow \infty$ , we approach the double ionization threshold (D.I.T.), where both electrons can be released into the continuum, leaving a bare  $\text{He}^{2+}$  nucleus behind.

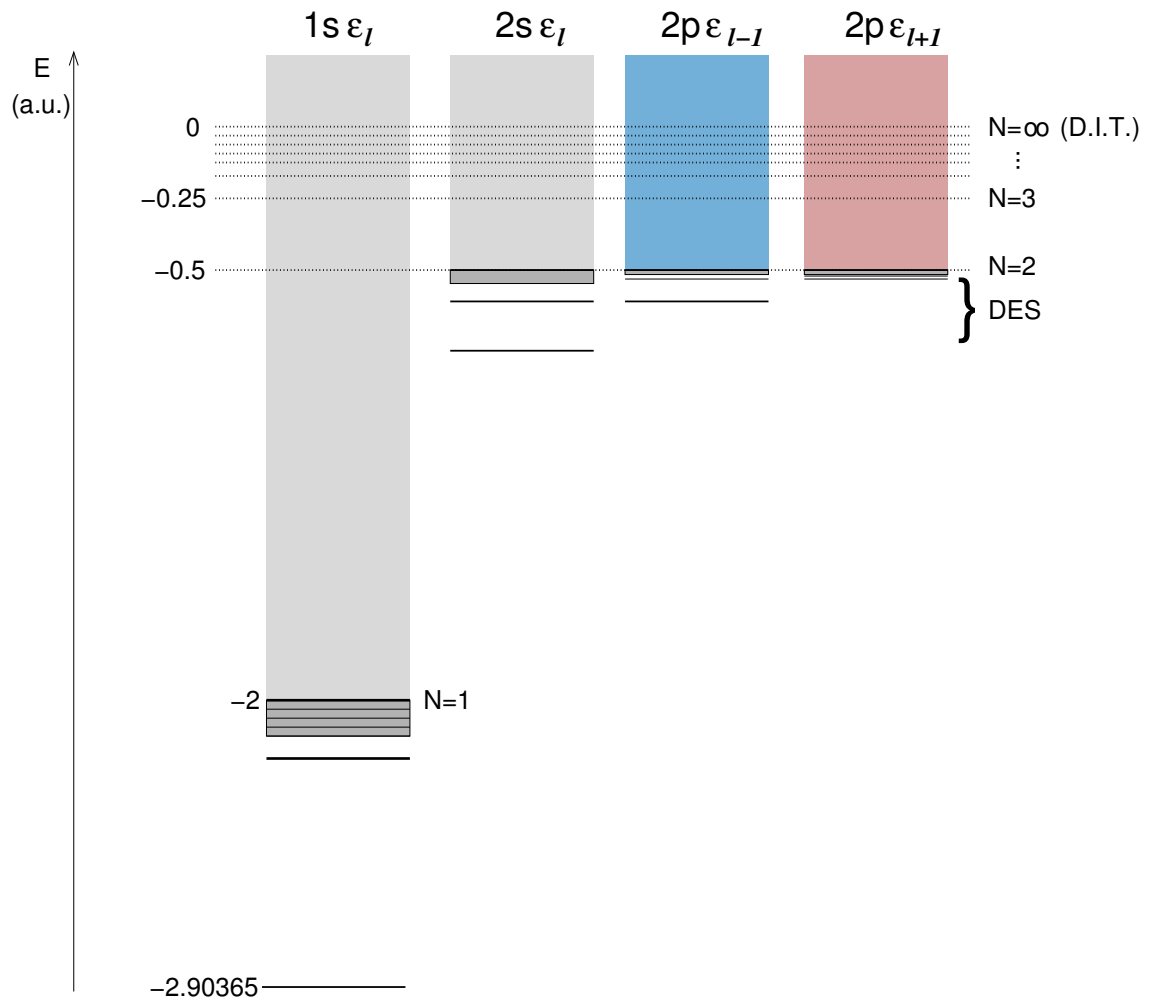


FIGURE 2.1: Helium energy scheme for a global symmetry with  $L=\ell$ , showing the single ionization channels which open at the  $N=1$  and  $N=2$  thresholds. The states below  $N=1$  are bound Rydberg states. The doubly-excited states associated to the  $N=2$  excited parent ion give rise to autoionizing states as a result of the interaction with the  $1s\epsilon_\ell$  continuum they are embedded in.  $N\ell$  specifies the state of the parent ion, while  $\epsilon_\ell$  refers to the energy and orbital angular momentum of the asymptotically free electron.

## 2.1 Electrostatic field-free hamiltonian.

The non-relativistic field-free electrostatic hamiltonian for the helium atom, neglecting mass polarization terms, reads

$$\mathbf{H}_{at} = \frac{\mathbf{p}_1^2}{2\mu} + \frac{\mathbf{p}_2^2}{2\mu} - \frac{Z}{r_1} - \frac{Z}{r_2} + \frac{1}{r_{12}}, \quad \mu = \frac{m_{He^+} \cdot m_{e^-}}{m_{He}} \quad (2.4)$$

where  $Z$  is the nuclear charge,  $\mathbf{p}_i$  and  $\mathbf{r}_i$  are the momentum and position operators of the individual particles,  $r_{12} = |\vec{r}_1 - \vec{r}_2|$  is the interelectronic distance, and  $\mu$  is the reduced mass of the electron - parent-ion binary system. For such a light system, either in isolation or in the dynamical regimes triggered by currently available attosecond light sources, relativistic and QED terms give rise to very small corrections which are beyond the scope of the current investigation and which can be safely neglected [55].

### 2.1.1 Symmetry and spin considerations.

(2.4) is not separable, i.e., one cannot find a complete set of commuting observables (C.S.C.O.); nonetheless, one still has conserved quantities.

Since we are not considering relativistic terms, the total orbital angular momentum and the spin are independently conserved,

$$\begin{aligned} [H, L_i] &= 0, [H, L^2] = 0 \\ [H, S_i] &= 0, [H, S^2] = 0 \end{aligned} \quad (2.5)$$

Due to inversion symmetry, parity ( $\pi$ ) must also be conserved,

$$[H, \Pi] = 0, \quad \Pi = \pi_1 + \pi_2, \quad \pi \vec{r} = -\vec{r} \quad (2.6)$$

These three observables are thus constants of motion <sup>1</sup>. Therefore, all eigenstates of the hamiltonian (2.4) can be labeled according to their quantum numbers,

$${}^{2S+1}L^\pi, \quad (2.7)$$

where  $2S + 1$  is the spin multiplicity,  $L = S, P, D, \dots$  is the total angular momentum and  $\pi = e/o$ , defines the even (e) or odd (o) parity of the state. If the parity of  $L$  is the same as  $\pi$ , then the state is said to be a *natural* state, e.g.,  ${}^1,3S^e$ ,  ${}^1,3P^o$ ,  ${}^1,3D^e$ , etc. If, on the contrary, the parity is not the same, then it is an *unnatural* state, e.g.  ${}^1,3P^e$ ,  ${}^1,3D^e$ , etc. (there are no odd S states for two-electron systems). Finally, of course, the

<sup>1</sup>It should be clear that the term *constant of motion* refers to the expectation value of the operator, not to the operator itself which, in the Schrödinger picture, is always independent of time.

energy is also conserved (the hamiltonian commutes with itself).

The Pauli principle dictates that the total wavefunction of a quantum system must be anti-symmetric with respect to arbitrary permutation of identical particles with half integer spin (as are the electrons). The permutational symmetry is preserved since the hamiltonian is totally symmetric under permutations. In the case of helium, which comprises just two electrons, the antisymmetry property can be enforced in a particularly simple way. This is because the symmetric group for two particles has just two irreducible representations, both monodimensional, the totally symmetric one and the totally antisymmetric one. Furthermore, the total spin operator is also totally symmetric. As a consequence, the spin functions with well defined total spin also have a well defined symmetry: singlet ( $S=0$ ) and triplet ( $S=1$ ) functions are anti-symmetric and symmetric, respectively. This means that the total wave function for a state with well-defined spin can be exactly factorized in a spin and a spatial component, both with well defined and opposite parity. The totally symmetric spatial wavefunction is normally called para, and the totally anti-symmetric is called ortho.

$$\begin{aligned}\mathcal{P}_{12}\Psi_s &= \Psi_s, & (para) \\ \mathcal{P}_{12}\Psi_{as} &= -\Psi_{as} & (ortho).\end{aligned}\tag{2.8}$$

$$\left. \begin{array}{l} \uparrow\uparrow \\ \downarrow\downarrow \\ \frac{1}{\sqrt{2}}(\uparrow\downarrow + \downarrow\uparrow) \end{array} \right\} S = 1 \quad (triplet)\tag{2.9}$$

$$\left. \frac{1}{\sqrt{2}}(\uparrow\downarrow - \downarrow\uparrow) \right\} S = 0 \quad (singlet)$$

### 2.1.2 Correlation in doubly excited states.

Doubly excited states are not easily classified due to the strong *correlation* between the two particles. At the most basic level, two particles are said to be correlated when their pair probability distribution,  $P_{12}(\vec{r}_1, \vec{r}_2)$ , does not factorize in the product of individual particle distributions, i.e.,  $P_{12}(\vec{r}_1, \vec{r}_2) \neq P_1(\vec{r}_1) \cdot P_2(\vec{r}_2)$ . Due to the antisymmetry requirement imposed by the Pauli principle on the wavefunction, however, it is convenient for electron to distinguish between two kinds of correlation: Fermi correlation and Coulomb correlation. Fermi correlation is due to the fact that electrons are indistinguishable. For example, in the simplest case of a single configuration, in which the wavefunction is the antisymmetrized product of two orbitals, the pair distribution is already non-factorizable. This correlation is already taken into account in a mean-field approximation. In this context, therefore, a correlated state will be one which needs

more than a single pair of orbitals to be described and which is induced by the non-mean-field component of the  $1/r_{12}$  electronic repulsion, i.e., the Coulomb correlation. In the case of the He doubly excited states, there is a special long-range correlation associated to the fact that the excited thresholds of  $\text{He}^+$ , a hydrogenic system, are degenerate. For example, below the  $N=2$  threshold, the states  $2snp$  and  $2pns$  are degenerate. As a consequence, the state that results from even the slightest interaction between them cannot possibly be described by a single reference determinant. Cooper *et al.* [56] realized that the electron-electron interaction removes this degeneracy, replacing the independent-particle configurations  $2snp$  and  $2pns$  with the pair

$$\Phi_{sp_n^\pm} = 2snp \pm 2pns. \quad (2.10)$$

This first type of correlation thus leads to the classification of DES in terms of the  $sp_n^\pm$  series. This kind of correlation does not lead by itself to Auger decay. The correlation which does lead to Auger decay is the one which couples these states to the open ionization channels. This term is negligible when the two electrons are far apart from each other, hence the alternative name short range correlation. A schematic diagram showing the two types of correlation is shown in Fig.(2.2).

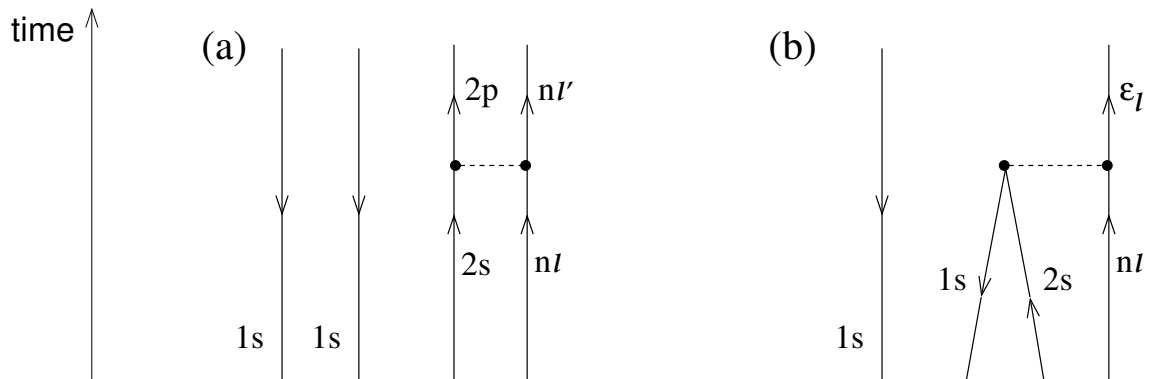


FIGURE 2.2: Diagram showing the two types of Coulomb correlation. (a). Long range correlation. Two holes in the 1S orbital and a doubly excited state with  $N = 2$ ,  $n = n$ . Due to the degeneracy between the  $2s$  and  $2p$  states, the states of the outer electron are strongly coupled. To lowest order, this coupling results in a correlation that is independent on the excitation of the outer electron. Yet the holes and electrons do not mix. (b). Short range correlation. Starting from the same configuration as in the previous case, the collision between the two electrons can result in a large energy exchange, leading to autoionization.

The effects of long-range and short-range Coulomb correlation are thus particularly evident for doubly excited states. In Fig.(2.3) we show the isosurface of the conditional probability density  $\rho^{(2)}(\vec{r}_1|\vec{r}_2)$ , defined as the probability density of finding electron 1 at a given position in space, once the position of the other electron is fixed.  $\rho^{(2)}(\vec{r}_1|\vec{r}_2)$  is

given by

$$\rho^{(2)}(\vec{r}_1|\vec{r}_2) = \frac{\rho^{(2)}(\vec{r}_1, \vec{r}_2)}{\rho^{(1)}(\vec{r}_2)} \quad (2.11)$$

where  $\rho^{(1)}(\vec{r})$  and  $\rho^{(2)}(\vec{r}_1, \vec{r}_2)$  are the electron density and the pair density, respectively.

In the case of helium:

$$\begin{aligned} \rho^{(2)}(\vec{r}_1, \vec{r}_2) &= \sum_{\xi_1, \xi_2} \Psi^*(x_1, x_2) \Psi(x_1, x_2) & \xi_i &= -\frac{1}{2}, \frac{1}{2} \\ \rho^{(1)}(\vec{r}) &= 2 \int d^3r' \rho^{(2)}(\vec{r}, \vec{r}') \end{aligned} \quad (2.12)$$

in which we have defined  $x_i = (\vec{r}_i, \xi_i)$ . To illustrate the nodal structure of the wave function, the interior part of the volume delimited by the isosurface is coloured according to the value of the real part of the wave function itself. In the left column, the fixed electron is fixed at a constant distance  $R$  from the nucleus, while the polar angle changes from 0 to  $\pi$ . In this case, the distribution is governed by long range (static) correlation. If we write the wavefunction for the doubly excited state of the  $sp_n^+$  series as

$$\Psi_{sp_n^+} = {}^1\Theta(\xi_1, \xi_2) \mathcal{S} [2s(\vec{r}_1)np(\vec{r}_2) + 2p(\vec{r}_1)ns(\vec{r}_2)] \quad (2.13)$$

where  ${}^1\Theta(\xi_1, \xi_2)$  is the singlet spin function and  $\mathcal{S}$  is the symmetrizer, and choose the position of the fixed electron such that the value of the parent-ion orbitals are negligible,  $2s(\vec{r}_2) \approx 0$  and  $2p(\vec{r}_2) \approx 0$ , then

$$\Psi_{sp_n^+} \cong \frac{1}{2} {}^1\Theta(\xi_1, \xi_2) [2s(\vec{r}_1)np(R \cdot \hat{z}) + 2p(\vec{r}_1)ns(R \cdot \hat{z})]. \quad (2.14)$$

This means that when  $\theta_2 = 0$ , the parent ion is strongly polarized upward, i.e., towards the outer electron, in a  $sp$  orbital; when  $\theta_2 = \pi/2$ , the parent ion is in a pure  $p$  state; finally, when  $\theta_2 = \pi$ , the parent ion is again strongly polarized towards the outer electron. In other terms, the polarization of the inner electron follows adiabatically the partition of the outer electron like a sunflower. At a closer inspection, one can see a clear asymmetry of the distribution; and this is because (2.14) does not account for the short-range correlation which, due to electronic repulsion, polarizes the electronic charge. Configuration mixing is large for DES, and the individual quantum numbers  $n_1$ ,  $n_2$ ,  $\ell_1$ ,  $\ell_2$  are not enough to identify the state [57].

The central and right columns illustrate the dramatic effect of short-range correlation, in which the distance between the fixed electron and the nucleus now varies.

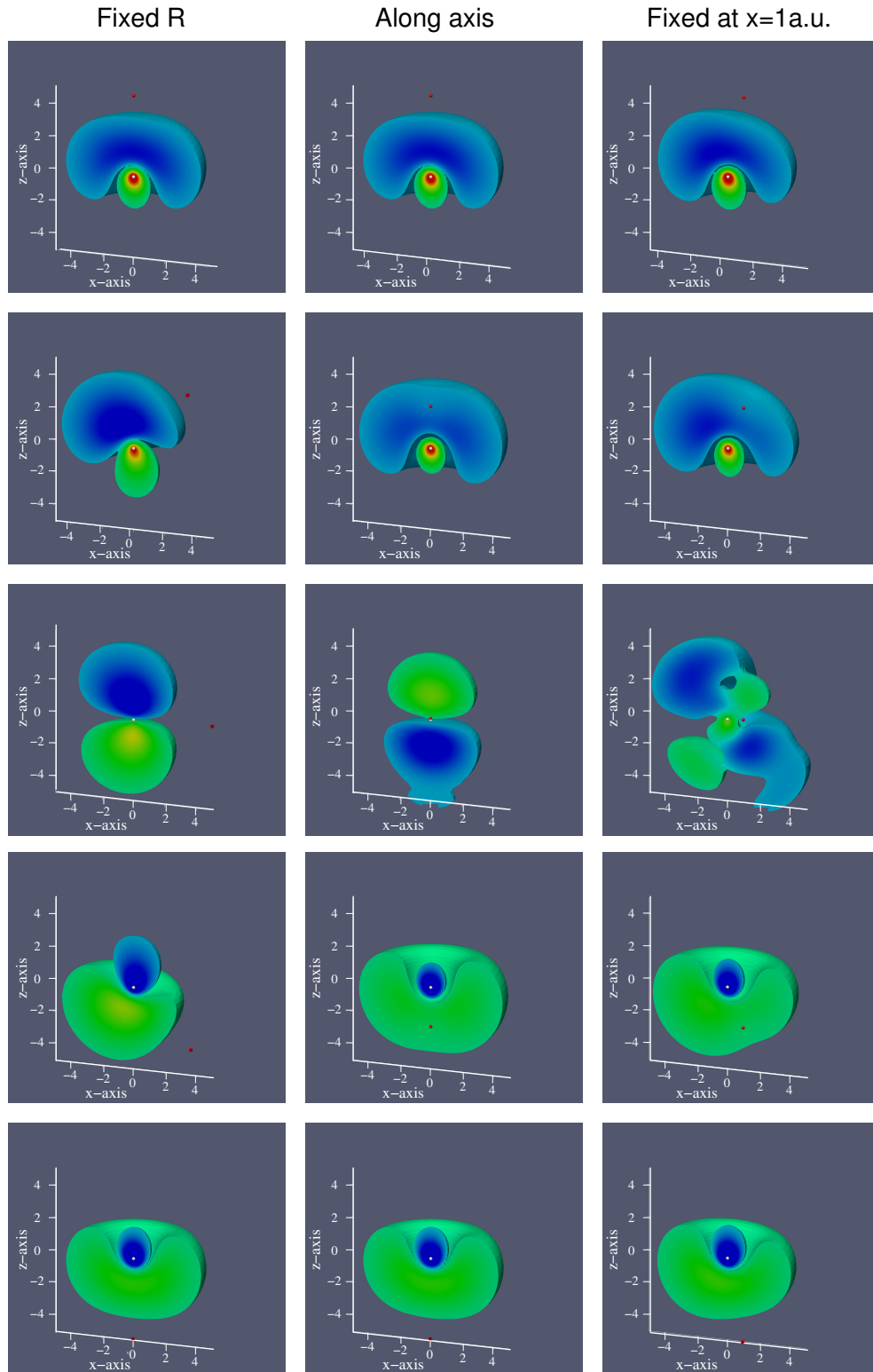


FIGURE 2.3: Conditional pair electron density for a superposition of doubly excited states in the  $1P^o sp_n^+$  series with  $M=0$  ( $z$  is the quantization axis). The position of the fixed electron is indicated by a red sphere. The nucleus, shown as a white sphere, is set at the origin. In the left column, the distance  $r_2$  of the fixed electron from the nucleus is kept constant while the polar angle  $\theta_2$  is, from top to bottom,  $0$ ,  $\pi/4$ ,  $\pi/2$ ,  $3\pi/4$ ,  $\pi$ . In the central column, we varied the position of the electron along the quantization axis. In the right column, the  $x$ -coordinate of the fixed electron is set at  $x=1$  a.u. while  $z$  changes from  $5$  to  $-5$ .

## 2.2 Close coupling basis. Eigenfunctions of the system.

We will be interested in the single ionization energy region, where the wavefunction must be asymptotically a linear combination of a parent ion in one of the permissible energy levels ( $E_n \leq E$ ) times an electron in the weak field of the ion with the residual energy  $\epsilon = E - E_n$ . For this reason, it is convenient to treat as an initial ansatz the states in which a parent ion is coupled to an electron to give rise to a state with well defined quantum numbers. Such factorization is referred to as the *close coupling* expansion. The close coupling basis is formed by various partial wave channels (PWC),

$$\phi_{\alpha E} = \mathcal{N} \hat{\mathcal{A}} \Theta_{S\Sigma} \mathcal{Y}_{L_\alpha \ell_\alpha}^{L0}(\Omega_1, \Omega_2) R_{N_\alpha L_\alpha}(r_1) \frac{f_{\alpha E}(r_2)}{r_2}, \quad (2.15)$$

where  $\alpha$  is an index that uniquely identifies the PWC,  $\Theta_{S\Sigma}$  is a two-electron spin function with total spin  $S$  and spin projection  $\Sigma$ , which in our case is  $\Theta_{00}$ .  $R_{N_\alpha L_\alpha}$  is the radial part of the frozen  $\text{He}^+$  parent ion state with principal quantum number  $N_\alpha$  and angular momentum  $L_\alpha$ .  $f_{\alpha E}$  is the radial function of the second electron, associated to the orbital angular momentum  $\ell_\alpha$  but otherwise unconstrained.  $\mathcal{Y}_{L_\alpha \ell_\alpha}^{L0}$  is a bipolar spherical harmonics [58] with total coupled angular momentum  $L$  and projection  $M = 0$ , defined as

$$\begin{aligned} \mathcal{Y}_{L_\alpha \ell_\alpha}^{LM}(\Omega_1, \Omega_2) &= \sum_{m_1, m_2} C_{\ell_1, m_1, \ell_2, m_2}^{LM} Y_{\ell_1, m_1}(\Omega_1) Y_{\ell_2, m_2}(\Omega_2) \\ &= (\langle \Omega_1 | \otimes \langle \Omega_2 |) | \ell_1 \ell_2 LM \rangle. \end{aligned} \quad (2.16)$$

Finally,  $\hat{\mathcal{A}}$  is the two particle antisymmetrizer,  $\hat{\mathcal{A}} = \frac{1}{2}(1 - \mathcal{P}_{12})$ , where  $\mathcal{P}_{12}$  is the permutation of particle 1 and 2 and  $\mathcal{N}$  is a normalization factor. The radial wavefunctions are expressed in terms of B-spline basis functions, which are capable of reproducing bound and continuum states of atomic and molecular wavefunctions with high accuracy [59].

In numerical computation, the PWC expansion needs to be truncated and, thus, it is not possible to include all single ionization channels of helium. Moreover, the set of bound states of the parent ion is not complete in the first place. The closed channels excluded in the truncated close-coupling expansion contribute to the short range correlation between the two electrons. This contribution, however, decays exponentially with the distance between them. Therefore, to take it into account, it is sufficient to include in the basis a *full-CI* pseudo-state localized channel (LC) composed of a large number of normalized two-electron functions built from localized orbitals. In this way, we effectively complete the functional space required to represent the eigenspace of the full time-independent hamiltonian in any given single-ionization spectral region, attaining both convergence

State	$E_{lit}$	$E_{code}$
1S	-2.903 724 377	-2.903 602 759
2S	-2.145 974 046	-2.145 966 683
2P	-2.123 843 086	-2.123 832 661
3S	-2.061 271 989	-2.061 269 940
3P	-2.055 146 362	-2.055 142 999
3D	-2.055 620 732	-2.055 620 575
4S	-2.033 586 717	-2.033 585 860

TABLE 2.1: Eigenvalues of the first seven bound states in helium. Comparison between the values obtained from the literature [55],  $E_{lit}$ , and the values of our calculation,  $E_{code}$ .

and good accuracy.

The final basis is thus built from linearly independent PWC and LC basis functions with well defined  $S$ ,  $\Sigma$ ,  $L$  and  $\Pi$ .

Since we are focusing on an energy region well below the  $N = 3$  level of the  $\text{He}^+$  parent ion, we limit the close coupling expansion to the PWCs with  $N \leq 2$ :  $1sE_L$ ,  $2sE_L$ ,  $2pE_{L+1}$  and  $2pE_{L-1}$  (the latter being present only for non-zero total angular momentum  $L$ ). At the moderate IR intensities considered here ( $I_{IR} \leq 10^{13} \text{ W/cm}^2$ ), a total angular momentum up to  $L = 9$  is sufficient to ensure convergence. Short-range correlation in the energy region of interest was found to be adequately taken into account by constructing the LC from orbitals with maximum radius  $R_{loc} = 40$  a.u. and with a maximum angular momentum  $L_{max} = 5$  for  $L \leq 2$  and  $L_{max} = 4$  for  $3 \leq L \leq 8$ . Short-range correlation states for  $L = 9$  were neglected altogether. The number of linearly independent PWC and LC basis functions with well defined  $S$ ,  $\Sigma$ ,  $L$ ,  $M$  and parity obtained with this choice of parameters is comprised between a minimum of 9064 for the  $^1S^e$  symmetry and a maximum of 13498 for the  $^1D^e$  symmetry.

Each eigenstate  $^1L^\pi$  of the field-free electrostatic hamiltonian  $H_0$  of the atom,

$$H_0 = \frac{p_1^2}{2} + \frac{p_2^2}{2} - \frac{2}{r_1} - \frac{2}{r_2} + \frac{1}{r_{12}} \quad (2.17)$$

is fully diagonalised and the matrix elements of the dipole operator  $\vec{P} = \vec{p}_1 + \vec{p}_2$  are computed for both the PWC and the LC basis. This full diagonalization is appropriate to compute the bound states of the system. The use of partial wave channels permits to compute at a comparatively little cost several Rydberg states. The eigenstates of  $H_0$  thus obtained form the basis for the time propagation of the atomic state under the action of external fields. The good accuracy of the calculations can be seen in Table (2.1) where we compare some energies with values from the literature.

### 2.2.0.1 Asymptotic limit of the wavefunction and Wigner time delay.

Photoelectrons created from a neutral atom are subject to the long-range Coulomb potential of the remaining ion plus a short range potential due to electron-electron interaction. For large values of  $kr$ , the wavefunctions  $f_{\alpha E}(r_2)$  in (2.15) approaches a shifted Coulomb function,

$$F_{\ell}(\nu, kr) \underset{r \rightarrow \infty}{\sim} \sin \left( kr - \frac{1}{2} \ell \pi + \frac{Z \ln 2kr}{k} + \sigma_{\ell} + \delta_{\ell} \right), \quad (2.18)$$

where  $\ell$  and  $k$  are the angular momentum and the wavenumber of the free electron, respectively.  $\sigma_{\ell} = \arg \Gamma(\ell + 1 + i\eta)$  is the Coulomb phase shift,  $\Gamma(z)$  is the Gamma function, and  $\delta_{\ell}$  is the additional phase shift that appears due to the electron-electron interaction (see Fig. (2.4)). All these phases are related to a time delay experienced by an almost monochromatic electron wavepacket as it scatters off the parent ion, as presented in the introduction.

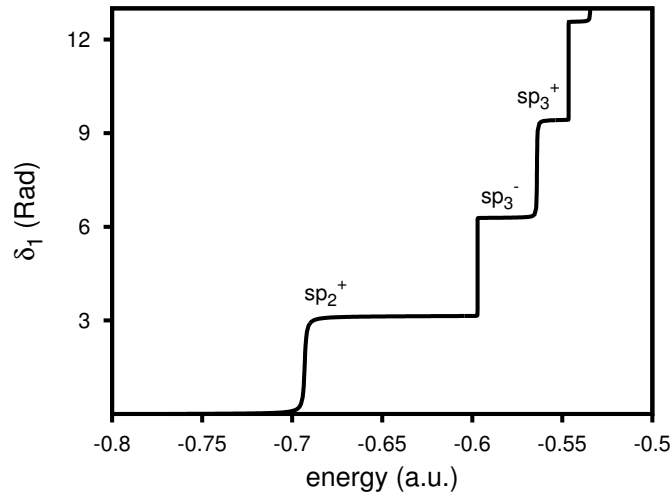


FIGURE 2.4: Scattering phase for the  $1P^o$  symmetry.  $\pi$  jumps are observed in correspondence to every doubly excited state with this symmetry.

## 2.2.1 Extraction of photoelectron distributions.

### 2.2.1.1 Calculation of the scattering states. The K-matrix method.

The single ionization scattering states of helium are the solutions of the secular problem

$$H\Psi_{\alpha E}^{\pm} = E\Psi_{\alpha E}^{\pm} \quad (2.19)$$

which satisfy prescribed boundary conditions. Traditionally, the requirement is that the incoming/outgoing component of the complete solution  $\Psi_{\alpha E}^{\pm}$  coincides with the incoming/outgoing component of a reference channel function  $\Phi_{\alpha E}$ .

$$[\Psi_{\alpha E}^{\pm}]_{in/out} = [\Phi_{\alpha E}]_{in/out}, \quad \langle \Psi_{\alpha E}^{\pm} | \Psi_{\beta E'}^{\pm} \rangle = \delta_{\alpha\beta} \delta(E - E'). \quad (2.20)$$

The  $\Phi_{\alpha E}$  are the eigenfunctions of a reference hamiltonian  $H_r$ , obtained by projecting the total hamiltonian on the individual partial wave channels

$$H_r = \sum_{\gamma} P_{\gamma} H P_{\gamma}, \quad H_r \Phi_{\alpha E} = E \Phi_{\alpha E}, \quad \langle \Phi_{\alpha E} | \Phi_{\beta E'} \rangle = \delta_{\alpha\beta} \delta(E - E') \quad (2.21)$$

Such scattering solutions can be expressed in terms of a linear combination of PWC and LC functions by means of the Lippman-Schwinger equation

$$\Psi_{\alpha E}^{\pm} = \Phi_{\alpha E} + \frac{1}{E - H_r} (H - H_r) \Psi_{\alpha E}^{\pm} \quad (2.22)$$

where the index  $\alpha$  runs over the channels which are open at energy  $E$ . By introducing the resolution of the identity and the off-shell T matrix,

$$\mathbf{T}_{\gamma\epsilon, \alpha E}^{\pm} = \langle \Phi_{\gamma\epsilon} | H - H_r | \Psi_{\alpha E}^{\pm} \rangle, \quad (2.23)$$

we can write

$$\Psi_{\alpha E}^{\pm} = \Phi_{\alpha E} + \sum_{\gamma} \int d\epsilon \Phi_{\gamma\epsilon} \frac{1}{E - \epsilon \pm i0^+} \mathbf{T}_{\gamma\epsilon, \alpha E}^{\pm}. \quad (2.24)$$

where the index  $\gamma$  runs over all open and closed channels, including the localized one. By treating the T matrix as an unknown set of coefficients and requiring that (2.19) holds, the system of integral equations

$$\mathbf{T}_{\gamma\epsilon, \alpha E} - \sum_{\beta} \int d\epsilon' V_{\gamma E'; \beta\epsilon} \frac{\mathbf{T}_{\beta\epsilon', \alpha E}}{E - \epsilon' \pm i0^+} = V_{\gamma E'; \alpha\epsilon} \quad (2.25)$$

is obtained. Since the system is invariant under time inversion, we can cast the problem in an alternative form. We look for stationary solutions as opposed to solutions that fulfill incoming and outgoing boundary conditions, and thus (2.24) now reads,

$$\Psi_{\alpha E}^P = \Phi_{\alpha E} + \sum_{\gamma} \int d\epsilon \Phi_{\gamma\epsilon} P \frac{1}{E - \epsilon} \mathbf{K}_{\gamma\epsilon, \alpha E} \quad (2.26)$$

where P indicates the principal part and

$$\mathbf{K}_{\gamma\epsilon, \alpha E} = \langle \phi_{\gamma\epsilon} | H - H_r | \Psi_{\alpha E}^P \rangle \quad (2.27)$$

being  $\Psi_{\alpha E}^P$  stationary solutions instead of the scattering functions. To find  $\Psi_{\alpha E}^P$  numerically, the expression (2.26) is inserted in (2.19), projected on the full numerical basis, the integrals are discretized and the resulting linear system is solved for the unknown coefficients  $\mathbf{K}_{\gamma\epsilon,\alpha E}$  by means of traditional numerical linear-algebra routines. The scattering states with definite spherical symmetry  $\Psi_{\alpha E}^-$  are then computed as

$$\tilde{\Psi}_{\alpha E}^{\pm} = \sum_{\beta} \Psi_{\beta E}^P \left[ \frac{1}{\mathbf{1} \pm i\pi \mathbf{K}(E)} \right]_{\beta\alpha} e^{\pm i(\sigma_{\ell\alpha} + \delta_{\alpha} - \ell_{\alpha}\pi/2)}, \quad (2.28)$$

where  $\mathbf{K}_{\alpha\beta}(E) \equiv \mathbf{K}_{\alpha E, \beta E}$  is the on-shell reactance matrix (§7.2.3 in [60]) which is hermitian, while  $\sigma_{\ell\alpha}$  and  $\delta_{\alpha}$  are the phase shifts introduced in 2.2.0.1. The stationary solutions  $\Psi_{\alpha E}^P$  are not normalized, while  $\Psi_{\alpha E}^{\pm}$  are. Finally, the scattering states which correspond to Coulomb plane waves associated with a parent ion in a given state A, are given by

$$\psi_{A,E\Omega\sigma}^- = \sum_{\alpha}^{L_{\alpha}=L_A, N_{\alpha}=N_A} C_{L_A M_A, \ell m}^{LM} C_{\frac{1}{2}\Sigma_A, \frac{1}{2}\sigma}^{S\Sigma} Y_{\ell m}^*(\Omega) \tilde{\Psi}_{\alpha E}^-, \quad (2.29)$$

where  $L_A$ ,  $M_A$ , and  $\Sigma_A$  indicate the angular momentum and spin of the parent ion,  $\Omega$  and  $\sigma$  indicate the asymptotic photoelectron's direction and spin, and  $C_{a\alpha, b\beta}^{c\gamma}$  are Clebsch-Gordan coefficients. The states  $\psi_{A,E\Omega\sigma}^-$  are normalized according to

$$\langle \psi_{A,E\Omega\sigma}^- | \psi_{B,E'\Omega'\sigma'}^- \rangle = \delta_{AB} \delta_{\sigma\sigma'} \delta(E - E') \delta(\Omega - \Omega'). \quad (2.30)$$

### 2.3 Solution of the TDSE.

The TDSE dictates the temporal evolution of the system, either in absence of external pulses or due to the interaction with weak as well as strong external time-dependent perturbations,

$$\begin{aligned} i\partial_t \Psi(t) &= H(t)\Psi(t) & H &= H_0 + H'(t) \\ \lim_{t \rightarrow -\infty} e^{iE_g t} \Psi(t) &= \Psi_g \end{aligned} \quad (2.31)$$

where  $H_0$  is the field free hamiltonian and  $H'(t)$  is the time-dependent perturbation,  $E_g$  is the energy of the ground state and  $\Psi_g$  is the ground state. The calculation of the interaction hamiltonian of the system will be the scope of the next section.

### 2.3.1 Interaction with an electromagnetic field. The minimal coupling hamiltonian.

To describe the interaction with the electromagnetic field, we will use a semiclassical approach, in which the electromagnetic field is treated classically while the atom-laser interaction is quantized. The electromagnetic field then obeys Maxwell's equations [61], which in absence of sources and in Coulomb gauge can be written in terms of the vector and scalar potentials  $\vec{A}$  and  $\Phi$  as

$$\begin{aligned}\nabla^2 \vec{A} - \frac{1}{c^2} \frac{\partial^2 \vec{A}}{\partial t^2} &= 0, \\ \Phi &= 0.\end{aligned}\tag{2.32}$$

Under these assumptions, the vector potential  $\vec{A}$  provides the transverse electric and magnetic field  $\vec{E}$  and  $\vec{B}$ , by

$$\begin{aligned}\vec{E} &= -\frac{1}{c} \frac{\partial \vec{A}}{\partial t}, \\ \vec{B} &= \nabla \times \vec{A}.\end{aligned}\tag{2.33}$$

It should be noted that  $\vec{A}$  and  $\Phi$ , that are gauge-dependent quantities [61], were introduced for mathematical convenience. The observable quantities remain the electric and magnetic fields, which indeed do not depend on the gauge. A pulse of plane-wave radiation can be represented by a superposition of monochromatic plane waves around a certain frequency,  $\Delta\omega$ , each with the same direction of propagation  $\hat{k}$  and polarization  $\hat{\epsilon}$ ,

$$\vec{A}(\vec{r}, t) = \int_{\Delta\omega} A_0(\omega) \hat{\epsilon} \left[ \exp[i(\vec{k} \cdot \vec{r} - \omega t + \delta_\omega)] + c.c. \right] d\omega,\tag{2.34}$$

where  $A(\vec{r}, t)$  is the vector potential of the field,  $\delta_\omega$  represents a real phase and *c.c.* the complex conjugate. When treating problems in which the wavelength of the radiation is much larger than the distance over which the photon absorption takes place, it is common to use the *dipole approximation*, in which the radial part of the vector potential  $\vec{A}$  is taken to be constant. This is our case, since the wavelengths we will be using are typically of several hundreds of atomic units, while the distance of interaction with the atom is of the order of 1 a.u. With this, we can write,

$$\vec{A}(t) = \int_{\Delta\omega} A_0(\omega) \hat{\epsilon} \left[ \exp[-i(\omega t - \delta_\omega)] + c.c. \right] d\omega.\tag{2.35}$$

Using (2.33) we can derive the frequency-domain relation

$$E(\omega) = -i \frac{\omega}{c} A(\omega).\tag{2.36}$$

The classical interaction between matter and radiation is described by the Lorentz force,  $\vec{F} = q \left( \vec{E} + \frac{\vec{v}}{c} \times \vec{B} \right)$ . Quantizing the classical light-matter interaction hamiltonian with appropriate generalized coordinates and conjugated momenta, we arrive to the *minimal-coupling* hamiltonian, which for one particle in velocity gauge reads [62],

$$\mathbf{H}_{mc}^v = \frac{p^2}{2} + \alpha \vec{p} \cdot \vec{A}(t), \quad (2.37)$$

where  $\alpha$  is the fine-structure constant. In atomic units,  $\alpha = 1/c \simeq 1/137$ . The interaction hamiltonian can be converted to the familiar length-gauge by means of the unitary transformation  $\Psi_v \rightarrow \Psi_L \equiv e^{i\vec{A}(t) \cdot \vec{r}} \Psi_v$ ,

$$\mathbf{H}_{mc}^L = \frac{p^2}{2} - \vec{E} \cdot \vec{r}. \quad (2.38)$$

We can connect the transition matrix elements for the *minimal coupling* hamiltonian in velocity gauge of Eq.(2.37) with those in the length gauge. Indeed, using the relation  $[H_0, \hat{\mathbf{R}}] = -i\hat{\mathbf{P}}$ ,

$$\langle \Psi_f | \mathbf{p} | \Psi_i \rangle = i[\langle \Psi_f | H_0 \mathbf{r} | \Psi_i \rangle - \langle \Psi_f | \mathbf{r} H_0 | \Psi_i \rangle]. \quad (2.39)$$

If the eigenstates are exact, then  $H_0 \Psi_{i/f} = E_{i/f} \Psi_{i/f}$ , and we can write

$$\langle \Psi_f | \mathbf{p} | \Psi_i \rangle = i(E_i - E_j) \langle \Psi_f | \mathbf{r} | \Psi_i \rangle \quad (2.40)$$

where  $\langle \Psi_f | \mathbf{r} | \Psi_i \rangle$  are the transition matrix elements in length gauge. It is worth noticing that, for our final solutions to be gauge invariant, we need to have very accurate eigenstates. Conversely, the gauge invariance of the results of a calculation is a useful cross-check of the convergence of the basis.

If we replace the kinetic term in the field-free hamiltonian with the velocity-gauge term in Eq. (2.37), we arrive to the final hamiltonian,

$$H_{tot} = H_{at} + H_{mc}^v = \frac{p_1^2}{2} + \frac{p_2^2}{2} - \frac{Z}{r_1} - \frac{Z}{r_2} + \frac{1}{r_{12}} + \frac{1}{c} (\vec{p}_1 + \vec{p}_2) \cdot A(t). \quad (2.41)$$

By neglecting relativistic corrections, which are of the order of  $\alpha^2$ , the time dependent hamiltonian remains spin independent. Transitions between singlet and triplet states (intercombination lines) are thus prohibited. Since our initial state will always be the  $1S^e$  ground state of helium, we need to consider only singlet intermediate and final states (para spatial wave functions).

Moreover, the dipole selection rules that come from the Wigner Eckhart theorem applied

to the matrix elements  $\langle \Psi_f | \hat{\varepsilon} \cdot \vec{p} | \Psi_i \rangle$ , give the following angular constraints,

$$\Delta\ell = \pm 1, 0 \quad \Delta m = 0, \pm 1. \quad (2.42)$$

In addition, to simplify the theoretical treatment, we will consider only light that is linearly polarized along a common direction ( $\hat{z}$ ). Our problem then presents cylindrical symmetry and the total z-projection of the angular momentum,  $m$ , will not change ( $\Delta m = 0$ ). As a consequence,  $\Delta\ell = 0$  transitions are prohibited and unnatural states cannot be populated either. For one- and two-photon processes starting from the  $1S^e$  ground state of helium, for example, the only possible symmetries we can populate are  $1S^e$ ,  $1P^o$  and  $1D^e$ .

### 2.3.2 Time evolution of the wavefunction.

The solution of the TDSE can be formally expressed in terms of the unitary time-evolution operator  $U(t, t_0)$  [63] :

$$|\Psi(t)\rangle = U(t, t_0) |\Psi(t_0)\rangle \quad (2.43)$$

This operator can be expressed also in the form of the Dyson series,

$$U(t, t_0) = \sum_{n=0}^{\infty} U_n(t, t_0), \quad \text{where} \quad (2.44)$$

$$U_n(t, t_0) = (-i)^n \int_{t_0}^t dt_1 \int_{t_0}^{t_1} dt_2 \dots \int_{t_0}^{t_{n-1}} dt_n H(t_1) H(t_2) \dots H(t_n).$$

Conversely, the Dyson series can be expressed in the formal T-exponential form,

$$U(t, t_0) = \hat{T} \exp \left[ -i \int_{t_0}^t d\tau H(\tau) \right], \quad (2.45)$$

where  $\hat{T}$  is the time ordering operator, which ensures the operators act in chronological order. Eq. (2.45) is at the basis of the perturbative expansion of the transition amplitude from an initial state  $|i\rangle$  to a final state  $|f\rangle$ .

$$\mathcal{A}_{f \leftarrow i} = \mathcal{A}_{f \leftarrow i}^{(0)} + \mathcal{A}_{f \leftarrow i}^{(1)} + \mathcal{A}_{f \leftarrow i}^{(2)} + \dots, \quad \text{where} \quad \mathcal{A}_{f \leftarrow i}^{(n)} = \langle f | U^{(n)}(t, t_0) | i \rangle. \quad (2.46)$$

For weak external potentials, the perturbative expansion converges rapidly and will be useful in the next chapter to derive some model results. The first order transition amplitude between two eigenstates of the field free hamiltonian  $H_0$ ,  $|i\rangle$  and  $|f\rangle$ , is linear with the perturbation  $H'(t)$ . Let us assume that  $H'(t)$  is given by the product of a

time-dependent field factor  $F(t)$  and of a time-independent operator  $\mathcal{O}$ ,

$$H'(t) = F(t)\mathcal{O}. \quad (2.47)$$

It is convenient to cast the TDSE in the interaction representation I,

$$i\partial_t \Psi_I(t) = H'_I(t)\Psi_I(t), \quad \Psi_I(t) = e^{iH_0 t} \Psi(t). \quad (2.48)$$

The first order transition amplitude then reads

$$\mathcal{A}_{f \leftarrow i}^{(1)} = \frac{1}{i} \int_{-\infty}^{+\infty} \langle f | H'_I(t') | i \rangle dt' = \mathcal{O}_{fi} \frac{1}{i} \underbrace{\int_{-\infty}^{+\infty} e^{i\omega_{fi} t} F(t) dt}_{\sqrt{2\pi} \tilde{F}(-\omega_{fi})}, \quad (2.49)$$

where  $\omega_{fi} = \omega_f - \omega_i$ . Proceeding to second order, the expression reads,

$$\begin{aligned} \mathcal{A}_{f \leftarrow i}^{(2)} &= - \int_{-\infty}^{+\infty} dt' \int_{-\infty}^{t'} dt'' e^{i\omega_{ft}'} F(t') F(t'') \langle f | \mathcal{O} e^{iH_0(t'-t'')} \mathcal{O} | i \rangle e^{i\omega_i t''} = \\ &= - \sum_j \mathcal{O}_{fj} \mathcal{O}_{ji} \int_{-\infty}^{+\infty} dt' e^{i\omega_{fj} t'} F(t') \int_{-\infty}^{t'} dt'' F(t'') e^{i\omega_{ji} t''}. \end{aligned} \quad (2.50)$$

If we consider that the two photons are absorbed in sequence, take the square module, and divide it by the exposure time  $T$ , we obtain the second order transition rate,

$$\mathcal{W}_{fi}^{(2)} = \frac{\pi F_{\omega_1}^2 F_{\omega_2}^2}{8} |\langle f | \mathcal{O} G_0^+(\omega_i + \omega) \mathcal{O} | i \rangle|^2 \delta(\omega_{fi} - \omega_1 - \omega_2). \quad (2.51)$$

where we have introduced the (retarded) resolvent operator, defined as

$$G_0^+(E) = \frac{1}{E - H_0 + i0^+}. \quad (2.52)$$

In the case of complicated matrix elements, of multiphoton resonant transitions, or of intense fields, the perturbative approach becomes impractical or even inapplicable. Furthermore, in the case of ultrashort pulses, non-perturbative stationary methods, like Floquet theory, may be inapplicable as well. In these cases, the best approach is the direct solution of the TDSE, made possible by large computational power available today. For this, first of all, the time interval during which the driven evolution takes place can be divided in  $N$  subintervals,

$$U(t, t_0) = \prod_{i=1}^n U(t_i, t_{i-1}) \quad t = t_n. \quad (2.53)$$

Let's assume for simplicity that the time steps are all equal

$$t_i = t_{i-1} + dt \quad dt = (t - t_0)/n. \quad (2.54)$$

We can now apply the Dyson expansion to each step-propagator

$$U(t_i, t_{i-1}) = \sum_{n=0}^{\infty} U^{(n)}(t_i, t_{i-1}). \quad (2.55)$$

We notice that when the Dyson series is truncated, the resulting propagator is not unitary and, therefore, it does not conserve the norm of the wavefunction. If the time step is sufficiently small, however, we can approximate the hamiltonian with its initial value in the middle of the interval. The Dyson series is then immediately integrated and the result is:

$$\tilde{U}(t_i, t_{i-1}) = e^{-idtH(t_i+dt/2)}. \quad (2.56)$$

### 2.3.2.1 Splitting scheme

Based on the previous ideas, we can now compute the evolution operator. Using Strang splitting, we can write the operator as

$$U = \exp[-iH_0dt/2] \exp[-iH'(t + dt/2)dt] \exp[-iH_0dt/2] + o(dt^3). \quad (2.57)$$

In practical implementations, the propagator and the wavefunctions are projected on the eigenstates of the field-free hamiltonian within the numerical B-spline close coupling basis. Hence,  $H_0$  is diagonal. The expansion coefficients can then be propagated using the following expression

$$C_j(t + dt) = \exp[-iE_jdt/2] \sum_j \{ \exp[-iH'(t + dt/2)dt] \}_{ij} \exp[-iE_jdt/2] C_j(t) + o(dt^3). \quad (2.58)$$

### 2.3.2.2 The Krylov method.

As (2.58) suggests, to compute the result of a time-step, we do not really need to know the whole exponential of  $iA = iH'(t + dt/2)dt$ . It is sufficient to know the result of the action of the exponential on a given vector,

$$\Psi' = \exp[-iA]\Psi. \quad (2.59)$$

To compute this quantity, we can follow a fast converging iterative procedure. The starting point is the construction of a Krylov space, which is generated by the subsequent

action of  $A$  on the state  $\Psi$ . In our case,

$$\begin{aligned}
\phi_1 &= \Psi \\
\phi_2 &= A\Psi \\
\phi_3 &= A^2\Psi \\
&\dots \\
\phi_{N+1} &= A^N\Psi
\end{aligned} \tag{2.60}$$

The set of vectors  $\{\phi_i\}$  thus generated is not orthogonal, and is orthonormalized by a Gram-Schmidt procedure  $\{\phi_i\} \rightarrow \{\varphi_i\}$ . In this way, we get the orthonormalized Krylov basis  $\{\varphi_i\}$ . The hamiltonian is then approximated as an  $(N+1) \times (N+1)$  matrix in this basis,

$$\begin{aligned}
A \sim A^N &= \sum_{ij} |\varphi_i\rangle A_{ij}^N \langle \varphi_j| \\
A_{ij}^N &= \langle \varphi_i | A | \varphi_j \rangle
\end{aligned} \tag{2.61}$$

In the limit  $N \rightarrow \infty$ , the eigenvalues and eigenvectors of the approximated hamiltonian will converge to those of the real hamiltonian. A direct diagonalization of such matrices can then be easily performed,

$$A \simeq \sum_i |\chi_i^N\rangle e^{-i\lambda_i^N} \langle \chi_i^N| \tag{2.62}$$

where  $\chi_i^N$  are the eigenvectors and  $\lambda_i^N$  the eigenvalues of the operator  $A^N$ . The operator in (2.59) is then substituted with the Krylov operator  $A^N$ , yielding

$$\Psi' = \exp[-iA]\Psi = \sum_i |\chi_i^N\rangle e^{-i\lambda_i^N} \langle \chi_i^N | \Psi \rangle \tag{2.63}$$

The numerical algorithm implemented is an Arnoldi algorithm, which is also suited to deal with non-hermitian matrices.

### 2.3.3 Absorption potential.

In order to avoid unphysical reflections of the wavefunction from the box, we added a complex absorption potential,  $V_{abs}$ , to the total time-dependent hamiltonian which effectively kills the wavefunction as it reaches the boundaries of the box. It is defined as,

$$\begin{aligned}
V_{abs}(\vec{r}_1, \vec{r}_2) &= v_{abs}(r_1) + v_{abs}(r_2) \\
v_{abs}(r) &= -ic_{abs}\theta(r - R_{abs})(r - R_{abs})^2,
\end{aligned} \tag{2.64}$$

where  $\theta(x)$  is the Heaviside step function. For our calculations, the values of  $c_{abs} = 5 \cdot 10^{-5}$  a.u. and  $R_{abs} = 1100$  a.u. were used.

### 2.3.4 Extraction of photoelectron distributions. Projection on scattering states.

In order to extract channel resolved photoelectron distributions, the final wavefunction is projected on the complete set of multi-channel scattering states,

$$\begin{aligned} \frac{dP_{AE\alpha\sigma}}{dE} &= |\langle \Psi_{AE\alpha\sigma}^- | \Psi(t) \rangle|^2, \\ \frac{dP_{AE\alpha\Omega\sigma}}{dEd\Omega} &= |\langle \Psi_{A\alpha\Omega\sigma}^- | \Psi(t) \rangle|^2. \end{aligned} \tag{2.65}$$

## Chapter 3

# Theory models

Due to the still comparatively low intensity of the sub-femtosecond XUV pulses [64] obtained with high-harmonic generation (HHG) [65], table-top experiments that investigate ultra-fast dynamics generally involve pump-probe schemes comprising a sequence of one or more XUV pulses in conjunction with a replica of the intense compressed Ti-Sapphire IR pulse used to create them [66–68] (see Sec.1.1). As a result of the interaction with the field, an atomic or molecular target is ionized and the fragments emerging from the reaction centre are collected. The spectral and angular distribution of the photo fragments encode information about all steps of the process triggered by light: the initial excitation out of the original bound state, the field-free evolution of coherent superpositions of states in the continuum during the time gap between pump and probe pulse, the dressed-state dynamics within the IR field as well as further transitions between excited states induced by the probe. Disentangling the contribution of these steps from the experimental result is a hard task which often requires assistance by theory. Indeed, since non-stationary non-perturbative transitions between highly-excited states may be involved, direct solution of the time-dependent Schrödinger equation (TDSE) is often needed to reproduce the experiment in all its aspects and in a quantitative way. Freezing of selected degrees of freedom in the system, fine tuning of the laser parameters and wave-packet inspection can be used to characterize the underlying ionization mechanism. Yet, these are time-consuming procedures. The analysis of both experiments and theoretical simulations is thus greatly facilitated if major aspects of the results can be explained by simplified models. In the case of atomic photoionization, a most prominent example is the strong-field approximation [69–71], a model which is able to reproduce well broad features of the photoelectron spectrum and which provided valuable insight into several non-perturbative processes triggered by radiation (see, e.g., [72, 73] and references therein). For resonant perturbative transitions in the continuum, the role of transiently bound states can be accounted for by the Fano model of autoionizing

states [41]. Despite the extensive interest that autoionizing states in interaction with external fields has attracted across the last three decades, it is only recently that the characteristic manifestation of metastable states in attosecond experiments has started to be appreciated. On the light of the most recent developments in time-resolved study of Auger decay and of continuum-continuum coherent transitions, a generalization of existing models to current ultrafast time-resolved laser schemes is needed.

In this chapter, we detail the models we developed. In Section 3.1 we review the action of an electromagnetic field on a free electron, introducing the Volkov states which is the basis of Soft Photon Approximation (SPA), that is described in Section 3.2. SPA has gained enormous importance in the last years due to its suitability to describe pump probe experiments, in which the pump pulse can be treated perturbatively, but the probe cannot. The SPA is introduced and extended to treat realistic effects in current experiments; in particular, finite probe pulse durations and intensity effects on the RABITT technique. The following sections (3.3, 3.4) are devoted to describe the RABITT technique in a perturbative approach for non-resonant continuum states and to review Fano's theory of autoionization [41]. Finally, in the last section, we introduce a two photon perturbative model for the RABITT technique with intermediate resonant states. Used in conjunction with attosecond pump probe experiments, this model is meant to provide a set of meaningful parameters that describe the influence of configuration interaction on coherent continuum-continuum radiative transitions and of time delay in laser-assisted scattering processes.

### 3.1 Volkov states.

For a free electron in an electromagnetic field, the minimal coupling hamiltonian is given by Eq. (2.37), and the Schrödinger equation reads

$$i\partial_t\Psi(t) = \left[\frac{p^2}{2} + \frac{1}{c}\vec{p}\cdot\vec{A}(t)\right]\Psi(t) \quad (3.1)$$

Since the hamiltonian is a function of the linear momentum  $\vec{p}$ , its eigenfunctions are plane waves with the following time dependence,

$$\Psi_{\vec{k}}^V(t) = \chi_{\vec{k}}(\vec{r}) \exp\left[-i\frac{k^2}{2}t - i\Theta(t)\right], \quad (3.2)$$

where

$$\chi_{\vec{k}}(\vec{r}) = \frac{1}{(2\pi)^{3/2}}e^{i\vec{k}\cdot\vec{r}} \quad (3.3)$$

are the plane waves, and

$$\Theta(t) = \alpha \vec{k} \cdot \int_0^t d\tau \vec{A}_{IR}(\tau). \quad (3.4)$$

Eq.(3.2) is the solution of a free electron in an electromagnetic field, and is known as a Volkov state.

### 3.2 The soft photon approximation.

Consider an atom A in its ground state  $|\phi_g\rangle$  subject to a strong IR pulse and a weak XUV pulse (or pulse train) triggering the ionization process

$$A + \gamma_{XUV} \pm n\gamma_{IR} \rightarrow A^+ + e_{\vec{k}}^-, \quad (3.5)$$

where  $\vec{k}$  is the momentum of the ejected photoelectron. The evolution of the system is described by the minimal-coupling time-dependent hamiltonian which, in dipole approximation and in velocity gauge [74], reads

$$H(t) = H_0 + \alpha \left[ \vec{A}_{IR}(t) + \vec{A}_{XUV}(t) \right] \cdot \vec{P} \quad (3.6)$$

where  $H_0$  is the field-free time-independent atomic potential,  $\alpha$  is the fine-structure constant,  $\vec{A}_{XUV}(t)$  and  $\vec{A}_{IR}$  are the transverse vector potentials of the XUV and IR pulses, respectively, and  $\vec{P}$  is the total electronic canonical momentum.

Since the XUV field is assumed to be weak, its effects can be treated at the level of the first-order time-dependent perturbation theory. If the intensity of the IR field is to take on large values, however, the interaction of the atom with it must be treated non-perturbatively. Therefore, the transition amplitude  $\mathcal{A}_{\lambda \leftarrow 0}$  from the initial state  $|\phi_g\rangle$  to a final scattering state  $|\phi_\lambda^-\rangle$  of the time-independent hamiltonian  $H_0$  (the minus and  $\lambda$  indexes in the final state stand for incoming boundary conditions and for a complete set of appropriate asymptotic quantum numbers, respectively) is given by the generalized expression

$$\mathcal{A}_{\lambda \leftarrow g} = -i \int_{-\infty}^{+\infty} \langle \psi_\lambda^-(t) | \alpha \vec{A}_{XUV}(t) \cdot \vec{P} | \psi_g^+(t) \rangle dt, \quad (3.7)$$

where  $|\psi_g^+(t)\rangle$  and  $|\psi_\lambda^-(t)\rangle$  are the dressed states of the time-dependent hamiltonian

$$H_F(t) = H_0 + \alpha \vec{A}_{IR}(t) \cdot \vec{P} \quad (3.8)$$

which fulfil assigned asymptotic conditions at  $t \rightarrow \mp\infty$ , respectively,

$$i\partial_t |\psi_g^+\rangle = H_F(t) |\psi_g^+\rangle, \quad \lim_{t \rightarrow -\infty} e^{iE_g t} |\psi_g^+(t)\rangle = |\phi_g\rangle, \quad (3.9)$$

$$i\partial_t|\psi_\lambda^-\rangle = H_F(t)|\psi_\lambda^-\rangle \quad \lim_{t \rightarrow +\infty} e^{iE_\lambda t}|\psi_\lambda^-(t)\rangle = |\phi_\lambda^-\rangle, \quad (3.10)$$

where  $E_g$  and  $E_\lambda$  are the initial and final energy, respectively.

We will now concentrate on the process of laser-assisted photoionization in the soft-photon approximation (SPA), i.e., the central frequency of the XUV pulse is assumed to be sufficiently high to drive the photoelectron well above the ionization threshold so that the IR field dresses the atom, thus generating multiphoton transitions between continuum states, but the final photoelectron spectrum still lies well above the ionization threshold and recollision is excluded. To evaluate this amplitude within the soft-photon model, we make three approximations.

- The ground state  $|\phi_g\rangle$  is unaffected by the IR field,  $|\psi_g^+(t)\rangle = e^{-iE_g t}|\phi_g(t)\rangle$  identically.
- The atom behaves as an hydrogenic system which is ionized from the  $1s$  orbital.
- The interaction of the emitted photoelectron with the parent ion is neglected altogether.

Less severe approximation which account for the interaction of the bound state with the dressing field [75], and for the interaction of the continuum state with the parent ion [76, 77] at a perturbative level have been considered in the past. These investigations confirm that if the neutral atom has large excitation energies, as it is certainly the case for helium, and the final energy of the photoelectrons are sufficiently far from the ionization threshold, these are reasonable approximations at the laser intensities realized for current compressed compressed Ti-Sapphire pulses. Under these assumptions, the final state  $|\psi_\lambda^-(t)\rangle$  in (3.7) reduces to a Volkov state (Eq.(3.2)).

### 3.2.1 Monochromatic soft-photon approximation.

For a monochromatic IR field,

$$\vec{A}_{\text{IR}}(t) = A_0 \cos(\omega_{\text{IR}}t + \varphi_{\text{IR}})\hat{e}, \quad (3.11)$$

where  $A_0$ ,  $\omega_{\text{IR}}$ ,  $\varphi_{\text{IR}}$ , and  $\hat{e}$  are the field amplitude, frequency, phase and polarization, respectively. The time-dependent phase  $\Theta(t)$ , therefore, reads

$$\Theta(t) = \vec{\alpha}_0 \cdot \vec{k} \sin(\omega_{\text{IR}}t + \varphi_{\text{IR}}) - \vec{\alpha}_0 \cdot \vec{k} \sin(\varphi_{\text{IR}}), \quad (3.12)$$

where we introduced the free-electron excursion amplitude  $\vec{\alpha}_0 = \alpha\omega_{\text{IR}}^{-1}A_0\hat{\epsilon}$ . The second term on the RHS of (3.12) results in a time-independent phase factor in the wave function, equivalent to an intensity-dependent phase convention for the plane wave basis, which disappears when taking the square module of the transition amplitudes to compute observable quantities. Therefore, in the following we will simply neglect it. We can apply, as usual, the Jacobi-Anger expansion [78] to obtain

$$|\Psi_{\vec{k}}(t; \vec{\alpha}_0)\rangle = |\vec{k}\rangle \sum_{n=-\infty}^{\infty} J_n(\vec{\alpha}_0 \cdot \vec{k}) \exp[-i(k^2/2 + n\omega_{\text{IR}})t - in\varphi_{\text{IR}}] \quad (3.13)$$

where  $J_n$  are Bessel functions and  $|\vec{k}\rangle$  is a plane wave,  $\langle \vec{r} | \vec{k} \rangle = (2\pi)^{-3/2} \exp(i\vec{k} \cdot \vec{r})$ . If we substitute (3.13) in (3.7), we obtain

$$\mathcal{A}_{\vec{k} \leftarrow g} \cong -i\sqrt{2\pi} \alpha (\vec{k} \cdot \hat{\epsilon}) \phi_g(k) \sum_{n=-\infty}^{+\infty} J_n(\xi x) e^{in\varphi_{\text{IR}}} \tilde{A}_{\text{XUV}}(E_g - k^2/2 - n\omega_{\text{IR}}), \quad (3.14)$$

where  $\phi_g(k)$  is the momentum representation of a 1s orbital with effective charge  $Z$  [63],

$$\phi_{1s}(k) = \frac{2\sqrt{2}Z^{5/2}}{\pi[k^2 + Z^2]^2}, \quad (3.15)$$

$x$  is the cosine of the angle formed by the photoelectron momentum and the laser polarization, and where we introduced the reduced field strengths  $\xi = \alpha_0 k$ . The reduced field strength, formulated in terms of the photoelectron energy  $E_e$  and of the IR intensity  $I_{\text{IR}}$  expressed in TW/cm<sup>2</sup>,

$$\xi = \frac{4\sqrt{\pi\alpha} E_e^{1/2}}{\omega_{\text{IR}}^2} \sqrt{\frac{I_{\text{IR}}(\text{TW}/\text{cm}^2)}{3.51 \cdot 10^4 \text{ TW}/\text{cm}^2}}, \quad (3.16)$$

is a very convenient quantity in the context of attosecond pump-probe experiments, since,  $E_e = 1$  a.u., an intensity  $I_{\text{IR}} = 1$  TW/cm<sup>2</sup>, and a driving laser frequency  $\omega_{\text{IR}} = 0.05712$  a.u. (a common order of magnitude for compressed Ti-Sapphire pulses), corresponds to  $\xi \simeq 0.99$ , i.e., it is essentially equivalent to one reduced field strength unit. In Equation (3.14) as well as in the following, the character tilda on top of a symbol indicates the Fourier transform of the corresponding time-dependent variable, e.g.,

$$\tilde{A}_{\text{XUV}}(\omega) = \frac{1}{\sqrt{2\pi}} \int_{-\infty}^{+\infty} e^{-i\omega t} A_{\text{XUV}}(t) dt. \quad (3.17)$$

Equation (3.14) can be directly used to compute the photoelectron distribution as

$$\frac{dP_{E\hat{\Omega} \leftarrow g}}{dE d\Omega} = k \left| \mathcal{A}_{\vec{k} \leftarrow g} \right|^2 \quad (3.18)$$

and applied to several cases of interest. In the following chapter we will examine a few. For monochromatic XUV pulses, further simplifications of (3.18) are possible [71, 73, 75]. Here, however, we are more interested on broadband XUV pulses in general, and on APTs in particular. First we will specialize the formula for the transition amplitude (3.14) to the RABITT technique. Next we will see how the case of a finite IR pulse can be simulated with a polychromatic Volkov state.

An idealized APT can be expressed as a modulated infinite sequence of identical pulses

$$A_{\text{XUV}}(t) = A_0 g(t) \sum_{n=-\infty}^{+\infty} (-1)^n f(t - n\pi/\omega_{\text{IR}}), \quad (3.19)$$

where  $g(t)$  is the envelope of the train and  $f(t)$  is the (dimensionless) profile, centred at the time origin, of each single pulse in the train. Alternatively, the same train can also be expressed as a combination of in-phase harmonics of the fundamental IR frequency (see Figure 1.1),

$$A_{\text{XUV}}(t) = \sqrt{\frac{8}{\pi}} \omega_{\text{IR}} A_0 g(t) \sum_{k=0}^{\infty} |\tilde{f}_{2k+1}| \cos[(2k+1)\omega_{\text{IR}}t + \phi_{2k+1}] \quad (3.20)$$

where the index  $k$  runs now over the harmonics, and we introduced the notation  $\tilde{f}_n = \tilde{f}(n\omega_{\text{IR}})$ ,  $\phi_n = \arg f_n$ . The spectrum of this field thus reads,

$$\tilde{A}_{\text{XUV}}(\omega) = \sqrt{\frac{2}{\pi}} A_0 \omega_{\text{IR}} \sum_{k=-\infty}^{+\infty} \tilde{f}_{2k+1} \tilde{g}[\omega - (2k+1)\omega_{\text{IR}}]. \quad (3.21)$$

In the following we will consider only the case of in-phase harmonics. However, in this latter formulation, the individual harmonic phases  $\phi_{2k+1}$  can be freely changed, so all the considerations in this work can be straightforwardly extended to treat arbitrary cases.

### 3.2.2 Pulsed soft-photon approximation.

To the best of our knowledge, the SPA has only been used in the monochromatic IR version outlined in the previous paragraph. This approximation, however, is justified only if the envelope of this dressing pulse does not change significantly across the duration of the XUV field. This is certainly the case of SAPs, where the full width at half-maximum (fwhm) of the XUV does not exceed a half period of the IR (streaking conditions). It is generally the case in the RABITT method as well, since common IR pulses have a duration of few tens of femtoseconds, which is longer than the common duration of an APT. Yet, compressed IR pulses with a duration of only a few femtoseconds are routinely produced [16, 17] and it is in principle not hard to devise an experiment

where an APT is aligned to a compressed replica of the IR pulse used to generate it and which could easily be as short as the APT itself. Furthermore, use of short IR pulses is common practice when solving the TDSE to limit the cost of computation, or even to render the simulation possible altogether. The IR modulation can be appropriately accounted for with a truncated cosine-square envelope:

$$\vec{A}_{\text{IR}}(t) = \begin{cases} A_0 \hat{\epsilon} \cos^2[\Omega(t - t_{\text{IR}})] \cos[\omega_{\text{IR}}(t - t_{\text{IR}}) + \varphi_{\text{IR}}], & \text{for } |t - t_{\text{IR}}| < \frac{\pi}{2\Omega} \\ \vec{0}, & \text{otherwise} \end{cases} \quad (3.22)$$

Since in the SPA model we are dealing with a structureless continuum, the multi-photon transition amplitudes which involve the absorption of at least one photon from the XUV field rapidly vanish as soon as the XUV and the IR pulses do not overlap. As a consequence, to examine the influence of a finite duration of the IR dressing field, one can replace the cosine-square single IR pulse (3.22) by a cosine-square *periodic* envelope,

$$\vec{A}_{\text{IR}}(t) = A_0 \hat{\epsilon} \cos^2[\Omega(t - t_{\text{IR}})] \cos[\omega_{\text{IR}}(t - t_{\text{IR}}) + \varphi_{\text{IR}}] \quad \forall t, \quad (3.23)$$

which corresponds to a non-truncated trichromatic IR field with well defined phase and intensity relation between the three frequency components. As long as all the XUV pulses lie well within the region  $|t - t_{\text{IR}}| < \frac{\pi}{2\Omega}$ , the contributions to the signal that come from the other oscillations of the IR envelope can be safely neglected. This periodic configuration for the IR dressing field, therefore, is appropriate to simulate the case of a finite IR pulse. With this choice, the free photoelectron will be indefinitely driven by the IR field, with no consequences other than an irrelevant phase factor due to forward Compton scattering. The phase  $\Theta(t)$  in (3.2) for the Volkov state in the presence of a modulated IR is

$$\Theta(t) = \vec{\alpha}_0 \cdot \vec{k} \cos^2[\Omega(t - t_{\text{IR}})] \sin[\omega_{\text{IR}}(t - t_{\text{IR}}) + \varphi_{\text{IR}}] + o(\Omega/\omega_{\text{IR}}) + \text{const}. \quad (3.24)$$

The time-independent term *const* can be ignored, as we did in the case of Equation (3.12). The higher-order correction  $o(\Omega/\omega_{\text{IR}})$  alters slightly the proportions of the monochromatic components of the zeroth-order term. If needed, it can be taken into account exactly; yet, it can generally be safely neglected. If we do so, the three frequency components of  $\Theta(t)$  are

$$\Theta(t) \simeq \frac{\vec{\alpha}_0 \cdot \vec{k}}{4} \left\{ 2 \sin [\omega_{\text{IR}}(t - t_{\text{IR}}) + \varphi_{\text{IR}}] + \sin [(\omega_{\text{IR}} + 2\Omega)(t - t_{\text{IR}}) + \varphi_{\text{IR}}] + \sin [(\omega_{\text{IR}} - 2\Omega)(t - t_{\text{IR}}) + \varphi_{\text{IR}}] \right\}, \quad (3.25)$$

so the Volkov phase factor for such field is just the product of the Volkov factors for the three individual monochromatic field components [see (3.13)]

$$\begin{aligned} \Psi_{\vec{k}}(\vec{r}, t) &\cong |\vec{k}\rangle \exp\left(-i\frac{k^2}{2}t\right) \sum_{\{n_i\}} J_{n_1}\left(\frac{x\xi}{2}\right) J_{n_2}\left(\frac{x\xi}{4}\right) J_{n_3}\left(\frac{x\xi}{4}\right) \times \\ &\times \exp\{-in_{\text{tot}}[\omega_{\text{IR}}(t - t_{\text{IR}}) + \varphi_{\text{IR}}]\} \exp[-4i(n_3 - n_2)\Omega(t - t_{\text{IR}})] \end{aligned} \quad (3.26)$$

where the sum runs over all positive and negative integer values of the three  $n_i$  indexes,  $n_{\text{tot}} = n_1 + n_2 + n_3$ . The transition amplitude is finally

$$A_{\vec{k}\leftarrow 0} \cong -i\sqrt{2\pi} \alpha x k \phi_g(k) \sum_{\{n_i\}} J_{n_1}\left(\frac{x\xi}{2}\right) J_{n_2}\left(\frac{x\xi}{4}\right) J_{n_3}\left(\frac{x\xi}{4}\right) \times \quad (3.27)$$

$$\begin{aligned} &\times \exp[in_{\text{tot}}(\varphi_{\text{IR}} + \omega_{\text{IR}}t_{\text{IR}}) - 2i(n_3 - n_2)\Omega t_{\text{IR}}] \times \\ &\times \tilde{A}_{\text{XUV}} \left[ E_g - \frac{k^2}{2} - n_{\text{tot}}\omega_{\text{IR}} + 2(n_2 - n_3)\Omega \right]. \end{aligned} \quad (3.28)$$

In the low intensity limit, we recover the two-photon transition amplitude from the lowest-order perturbative treatment in the plane-wave approximation. The integrated sideband signal is given by

$$I_{2n} = \int_{E_-}^{E_+} dE \int d\Omega \sqrt{2E} |\mathcal{A}_{\vec{k}\leftarrow g}|^2, \quad E_{\pm} = E_g + \frac{4n \pm 1}{2} \omega_{\text{IR}} \quad (3.29)$$

### 3.2.3 Frequency-comb limit.

Key to the standard application of the RABITT technique is the perturbative approximation where only one IR photon is assumed to be exchanged with the atom. At intensities of the order of 1TW/cm<sup>2</sup>, however, additional paths that imply the exchange of two or more IR photons become important. As a consequence, several transition matrix elements contribute to give rise to the variation of the photoelectron sideband intensity as a function of the time delay. In particular, on the side to the fundamental RABITT frequency  $2\omega_{\text{IR}}$ , several overtones  $2n\omega_{\text{IR}}$  appear, which have an involved relation with the phases of the harmonics in the train. For this reason, high intensities are generally considered detrimental to the resolution with which the RABITT technique can reconstruct the average profile of an attosecond pulse within the train [79]. This does not have to be necessarily the case, however, if a reliable correspondence between the sideband signal and the underlying harmonics beyond the perturbative regime can be established. To gain insight on the dependence of the sideband signal on the intensity of the dressing laser, let us consider the limiting case of a frequency comb [80], i.e., of a very long sequence of very narrow XUV pulses. In this case, the spectrum of the field is locally given by a series of equally spaced narrow peaks with similar height. We can extrapolate the SPA to this limit, and obtain an analytical expression for the intensity

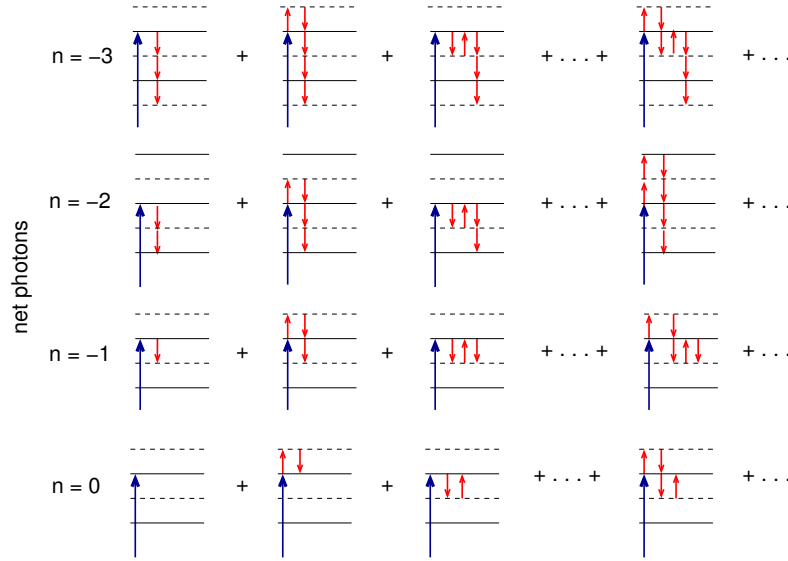


FIGURE 3.1: For intense dressing fields, several IR photons can be exchanged. For each amplitude that corresponds to a net number of IR photons absorbed or emitted, an infinite number of diagrams contribute. The soft-photon approximation adds up to infinite order the contribution of all the time-ordered diagrams where the first absorbed photon is from the XUV field. The amplitude for a net exchange of  $n$  IR photons carries the phase  $n\varphi_{\text{IR}} = n\omega_{\text{IR}}t_{\text{d}} + \varphi_{\text{IR},0}$ . As a consequence, overtones at all even multiples  $2m\omega_{\text{IR}}$  of the dressing-laser fundamental frequency will appear in the time-delay dependence of the sideband intensity (only amplitudes with an odd net number of exchanged IR photons can contribute to sidebands).

of all the discrete frequency components of the sidebands as a function of the time delay. Let us assume that the comb Fourier spectrum has the following expression,

$$\tilde{\mathcal{A}}_{\text{XUV}}(\omega) = A_0 \omega_{\text{IR}} \sum_{i=-\infty}^{+\infty} \tilde{g}[\omega - (2i+1)\omega_{\text{IR}}], \quad (3.30)$$

where  $\tilde{g}(\omega)$  is a sharp function centred in a small neighbourhood of  $\omega = 0$ . If we focus on the sideband  $2m$ , the photoelectron signal is negligible unless the electron final kinetic energy lies in the close vicinity of  $E_{\text{g}} + 2m\omega_{\text{IR}}$ ,  $k^2/2 = E_{\text{g}} + 2m\omega_{\text{IR}} + \varepsilon$ . When inserted in (3.14), therefore, equation (3.30) gives rise to factors of the form

$$\tilde{g}[-(2m+n+2i+1)\omega_{\text{IR}} + \varepsilon], \quad (3.31)$$

which are non-negligible only if  $2m+n+2i+1 = 0$ . As a consequence, only net exchanges of an odd number  $n$  of IR photons can contribute. The amplitude in (3.14) is then,

$$\mathcal{A}_{\vec{k} \leftarrow 0} \cong -i A_0 \omega_{\text{IR}} \sqrt{2\pi} \alpha k_{2m} \phi_{\text{g}}(k_{2m}) \tilde{g}(\varepsilon) \sum_n^{\text{odd}} x J_n(\xi x) e^{in\varphi_{\text{IR}}}, \quad (3.32)$$

where  $x$  is the cosine of the angle formed by  $\vec{\alpha}_0$  and  $\vec{k}_{2m}$ , and  $k_{2m} = (4m\omega_{\text{IR}} + 2E_{\text{g}})^{1/2}$ . Both the pre factor and the argument of the integral in (3.32) are smooth functions of the electron energy: consecutive sidebands have almost identical qualitative behavior. In the following, therefore, for the sake of conciseness, we render the dependence on the final energy implicit, drop the sideband index and refer to a generic sideband instead. The integral of the sideband signal is thus

$$I_{\text{SB}} = \beta \int_{-1}^1 x^2 dx \left| \sum_n^{\text{odd}} J_n(\xi x) e^{in\varphi_{\text{IR}}} \right|^2, \quad (3.33)$$

where  $\beta$  collects the fixed factors that depend on the details of the XUV spectrum but not on the IR intensity,

$$\beta = 2\pi |\alpha \omega_{\text{IR}} A_0 k_{2m} \phi_{\text{g}}(k_{2m})|^2 \int_0^\infty \sqrt{2\varepsilon} d\varepsilon |\tilde{g}(\varepsilon)|^2. \quad (3.34)$$

The integral in (3.33) determines the frequency composition of each and every sideband in the frequency-comb limit, due to the interference of the contributions arising from the net exchange of an arbitrary odd number of IR photons (see Figure 3.1). We can reformulate the expression (3.33) by factorizing the dependence on the IR phase  $\varphi_{\text{IR}} = \omega_{\text{IR}} t_{\text{d}}$  (we assume a zero absolute IR phase  $\varphi_{\text{IR},0}$ ),

$$I_{\text{SB}} = \beta \sum_{j=0}^{\infty} C_j(\xi) \cos(2j \omega_{\text{IR}} t_{\text{d}}), \quad (3.35)$$

$$C_j(\xi) = \int_{-1}^1 \frac{2x^2 dx}{1 + \delta_{j0}} \sum_n^{\text{odd}} J_n(\xi x) J_{n+2j}(\xi x) \quad (3.36)$$

where the index  $j$  designates the sideband harmonic component, namely: average signal ( $j = 0$ ); fundamental RABITT frequency ( $j = 1$ ); first overtone ( $j = 2$ ); second overtone ( $j = 3$ ), etc. Equations (3.35),(3.36) completely characterize the temporal profile of sideband intensities in the idealized case of a frequency comb pump sequence as a function of both the time delay and the IR intensity. The integral in (3.36) could be expressed in closed form in terms of special functions. The result, however, is rather lengthy and does not seem to provide further insight. As will be discussed in more detail in the following chapter, a major feature of the  $C_j(\xi)$  coefficients is that, for  $j > 0$ , they oscillate around zero as a function of  $\xi$ , crossing the axis for different values of the reduced field strength. This means that not only the relative proportion of the frequency-component amplitudes of the sideband changes with the intensity. In fact, the fundamental RABITT component periodically vanishes altogether, a condition in which overtones dominate.

### 3.3 Perturbation theory for RABITT

#### 3.3.1 RABITT for non-resonant intermediate states.

In Sections 1.2.1 and 1.3.2 we commented that the RABITT technique can be used to access the parameters of continuum-continuum radiative transitions in atoms and, in particular, the time delay in photoelectron emission and in electron - parent-ion collisions associated to the continuum structure, e.g., autoionizing states. In the case of a structureless continuum, i.e., for a free electron, the two-photon transition matrix element  $M_{2n\pm 1}$  defined in (1.2),

$$\mathcal{M}_{2n\pm 1} = \langle E|P[G_0^+(\omega_g \mp \omega) + G_0^+(\omega_g + \omega_{2n\pm 1})]P|i\rangle. \quad (3.37)$$

can be explicitly evaluated

$$\mathcal{M}_{2n\pm 1} = \pm \frac{\sqrt{4\pi}}{3\omega} Y_{10}^2 \phi_0(\vec{k}), \quad (3.38)$$

where we considered that the transition corresponding to an IR photon first is negligible<sup>1</sup>. We made use of the relations

$$G_0^+(\omega) = \int d^3k \frac{|\vec{k}\rangle \langle \vec{k}|}{\omega - \frac{k^2}{2} + i0^+}, \quad \vec{p}|\vec{k}\rangle = \vec{k}|\vec{k}\rangle \quad (3.39)$$

and we defined  $\phi_0(\vec{k}) = \langle \vec{k}|\vec{\phi}_g\rangle$ . As anticipated above, the transition matrix element is real, i.e.,  $\varphi_n^{at.} = 0, \pi$ .

In the following, we will address the more interesting case in which an intermediate resonant state is present. In Section 3.5.1 we develop a model that permits us to extract intrinsic information on the autoionizing state and on its dipole transition matrix element with the continuum it is embedded in, from the phase shift that can be measured with the RABITT scheme. For this, it is convenient to briefly review the main aspects of Fano's theory of configuration interaction in the continuum.

### 3.4 Fano model of autoionization.

To describe the wavefunction of a system with a state embedded in the atomic continuum we follow Fano's theory of configuration interaction. Let us consider a time independent

<sup>1</sup>This approximation is valid from the ground state since the frequency of the IR is typically  $\omega_{\text{IR}} \approx 0.055$  a.u., and the difference between the ground and the first excited states in, for example, helium, is of the order of 0.75 a.u.

hamiltonian, separated into the sum of a reference hamiltonian  $H_0$  and a perturbation  $V$ ,

$$H = H_0 + V \quad (3.40)$$

By hypothesis,  $H_0$  has a set of continuum eigenstates  $|E\rangle$ , starting at the threshold  $E_{th}$ , and two bound eigenstates, the ground state  $|0\rangle$  and another state  $|a\rangle$  that lies above the ionization threshold,  $E_a > E_{th}$ ,

$$H_0|0\rangle = |0\rangle E_0, \quad H_0|a\rangle = |a\rangle E_a, \quad H_0|E\rangle = |E\rangle E \quad \forall E \geq E_{th}. \quad (3.41)$$

The eigenstates of  $H_0$  are orthogonal and normalized as

$$\langle 0|0\rangle = \langle a|a\rangle = 1, \quad \langle E|E'\rangle = \delta(E - E') \quad \forall E, E' \geq E_{th}. \quad (3.42)$$

We further assume that the only effect of the perturbation potential  $V$  is to couple the state  $|a\rangle$  to the continuum states

$$V_{aE} = \langle a|V|E\rangle = \langle E|V|a\rangle^* \quad (3.43)$$

All the other matrix elements of  $V$  being zero. We seek to find the eigenfunctions,  $|\psi_E\rangle$ , of the complete hamiltonian,

$$(E - H)|\psi_E\rangle = 0. \quad (3.44)$$

By projecting the secular equation on the complete set of unperturbed eigenstates and using standard properties of generalized functions (distributions), it is possible to show that the solutions to this problem are given by,

$$|\psi_E\rangle = |E\rangle + |a\rangle \frac{V_{aE}}{E - \tilde{E}_a(E)} + \int d\varepsilon |\varepsilon\rangle \frac{V_{\varepsilon a}}{E - \varepsilon + i0^+} \frac{V_{aE}}{E - \tilde{E}_a(E)}. \quad (3.45)$$

which are called the Fano wavefunctions. We introduced the *complex resonance energy*  $\tilde{E}_a(E)$  as

$$\tilde{E}_a(E) = E_a + \Delta_a(E) - \frac{i}{2}\Gamma_a(E). \quad (3.46)$$

in which the energy shift  $\Delta_a(E)$  and resonance width  $\Gamma_a(E)$  of the state  $|a\rangle$  are defined as

$$\Delta_a(E) = P \int \frac{V_{a\varepsilon} V_{\varepsilon a}}{E - \varepsilon} d\varepsilon, \quad \Gamma_a(E) = 2\pi |V_{aE}|^2. \quad (3.47)$$

The resonance width  $\Gamma_a$ , which is the inverse of the lifetime of the resonance, measures the coupling strength between the state  $|a\rangle$  and the continuum.  $\Gamma_a$  can be seen as the rate constant for the first-order reaction,



A stronger coupling between the transiently bound state and the continuum clearly leads to a faster autoionization process, thus decreasing the lifetime of the doubly excited state. To simplify the expression, we can further define a dressed resonance  $|\tilde{a}\rangle$ ,

$$|\tilde{a}\rangle = |a\rangle + P \int d\varepsilon |\varepsilon\rangle \frac{V_{\varepsilon a}}{E - \varepsilon}, \quad (3.49)$$

and the normalized distance to the center of the resonance,

$$\epsilon(E) \equiv \frac{E - \tilde{E}_a^R(E)}{\Gamma_a(E)/2}. \quad (3.50)$$

In this way, the Fano wave function takes the more compact form

$$|\psi_E\rangle = |E\rangle \frac{\epsilon}{\epsilon + i} + |\tilde{a}\rangle \frac{1}{\pi V_{Ea}} \frac{1}{\epsilon + i}. \quad (3.51)$$

The final wave function depends on both the energy shift and resonance width which, in turn, depend on the energy  $E$ . However, it is generally the case that the coupling term  $V_{aE}$  changes smoothly across a large energy interval; therefore we can approximate both parameters to their value at the resonance energy  $E = E_a$ , for which the experimental values are widely known.

### 3.5 Two photon perturbative model with intermediate autoionizing states.

In the extension of the perturbative non-resonant RABITT treatment, we consider a structured intermediate continuum. More specifically, a continuum which features an isolated Fano-type resonance in P symmetry as a result of the interaction between a localised state  $|a\rangle$  and the plane-wave continuum. The intermediate states are thus solutions of the single-channel Fano scattering problem given by Eq. (3.45). The unperturbed continuum wavefunctions of the final states as well as of the first term in Eq. (3.45) will be described by spherical free waves,

$$\langle \vec{r} | k' \ell m \rangle = \sqrt{\frac{2k'^2}{\pi}} Y_{\ell m}(\hat{r}) j_{\ell}(k' r), \quad \langle k \ell m | k' \ell' m' \rangle = \delta_{\ell \ell'} \delta_{m m'} \delta(k - k') \quad (3.52)$$

which as we will see in the following chapter, reproduce with high accuracy the results of pump-probe spectroscopic experiments in a non-resonant background.

### 3.5.1 Model.

To evaluate the transition matrix element from an initial S state within these assumptions, it is convenient to express the resolvent in spherical coordinates

$$G_0^+(\omega) \equiv \frac{1}{\omega - H_0 + i0^+} = \sum_{\ell m} G_{0,\ell m}^+, \quad G_{0,\ell m}^+ = \sum_{\ell} \int dE \frac{|\Psi_{\ell m E}^+\rangle \langle \Psi_{\ell m E}^+|}{\omega - E + i0^+} + \frac{|1s\rangle \langle 1s|}{\omega - \omega_i} \quad (3.53)$$

where we indicated with  $\Psi_{\ell m E}^+$  a complete set of scattering states of the hamiltonian (we assume that the ground is the only bound state of the system),

$$\begin{aligned} H_0 |\Psi_{\ell m E}^+\rangle &= E |\Psi_{\ell m E}^+\rangle, & \langle \Psi_{\ell m k}^+ | \Psi_{\ell' m' E'} \rangle &= \delta_{\ell \ell'} \delta_{m m'} \delta(E - E') \\ L^2 |\Psi_{\ell m E}^+\rangle &= \ell(\ell + 1) |\Psi_{\ell m E}^+\rangle, & L_z |\Psi_{\ell m E}^+\rangle &= m |\Psi_{\ell m E}^+\rangle, \end{aligned} \quad (3.54)$$

To compute the two-photon transition matrix elements in (1.2) in the case of collinear fields, we only need the  $G_{0,10}^+$  component of such resolvent. For simplicity, in the following we will not indicate the  $\ell m$  indexes for the intermediate states understanding that they are 1 and 0, respectively,

$$G_0^+(\omega) = \int dE \frac{|\Psi_E^+\rangle \langle \Psi_E^+|}{\omega - E + i0^+}. \quad (3.55)$$

According to our assumptions, the intermediate P states are given by the Fano solutions to the scattering problem 3.54 (Eq. (3.45)). We should now substitute (3.55) in (1.2). To simplify the treatment we will drop the second resolvent component in each transition amplitude  $M$ , which corresponds to the non-resonant initial absorption/emission of an IR photon from the ground state and which is normally much smaller than the contribution of the diagram with opposite time ordering,

$$M_{2n\pm 1} \cong \int dE \frac{\langle E_f \ell 0 | \mathcal{O} | \Psi_E^+ \rangle \langle \Psi_E^+ | \mathcal{O} | i \rangle}{\omega_i + \omega_{2n\pm 1} - E + i0^+}. \quad (3.56)$$

The matrix element from the intermediate to the final state assumes the following form,

$$\begin{aligned} \langle E_f \ell 0 | P_z | \Psi_E^+ \rangle &= \langle E_f \ell 0 | P_z | E10 \rangle + \int dE' \frac{V_{E'a}}{E - E' + i0^+} \frac{V_{aE}}{E - E_a + i\Gamma_a/2} \\ &+ \langle E_f \ell 0 | P_z | a \rangle \frac{V_{aE}}{E - E_a + i\Gamma_a/2}, \end{aligned} \quad (3.57)$$

where  $E_f$  is the final energy, while that for monochromatic fields can be written as  $E_f = \omega_i + \omega_{2n}$ , with  $\omega_i = -IP$  and  $\omega_{2n} = 2n\omega_{ir}$ ,  $n$  being an integer that corresponds to the sideband order. For symmetry reasons, the angular dependence of the matrix

element  $\langle E_f \ell 0 | P_z | a \rangle$  can comprise only a rank 0 and a rank 2 component

$$\langle E_f \ell 0 | P_z | a \rangle = Y_{00}(\hat{k}) \phi_{aS}(k) + Y_{20}(\hat{k}) \phi_{aD}(k). \quad (3.58)$$

The functions  $\phi_{aS}(k)$  and  $\phi_{aD}(k)$  dictate the photoelectron angular distribution and must be seen as unknown new parameters in the model. Indeed, there is no consistent way of deriving such parameters within the single-particle picture. For simplicity, let us unite these two parameters in a single one, containing also the angular dependence, which is the radiative transition matrix element from the bound component  $|a\rangle$  to the continuum. We call  $\langle E_f \ell 0 | P_z | a \rangle = \mathcal{O}_{E_f a}^\ell$ .

After computing explicitly the continuum-continuum matrix element between spherical free waves, we are left with

$$\begin{aligned} \langle E00 | P_z | \Psi_E^+ \rangle = & -\frac{i}{\sqrt{3}} \sqrt{2E_f} \left[ \underbrace{\delta(E - E_f)}_C + \overbrace{\frac{V_{E_f a}}{E - E_f + i0^+} \frac{V_{aE}}{E - E_a + i\Gamma_a/2}}^M \right] + \\ & + \underbrace{\mathcal{O}_{E_f a}^S \frac{V_{aE}}{E - E_a + i\Gamma_a/2}}_B, \end{aligned} \quad (3.59)$$

$$\begin{aligned} \langle E20 | P_z | \Psi_E^+ \rangle = & i\sqrt{\frac{4}{15}} \sqrt{2E_f} \left[ \delta(E - E_f) + \frac{V_{E_f a}}{E - E_f + i0^+} \frac{V_{aE}}{E - E_a + i\Gamma_a/2} \right] + \\ & + \mathcal{O}_{E_f a}^D \frac{V_{aE}}{E - E_a + i\Gamma_a/2}. \end{aligned}$$

As we see from the above expression, the contributions of the S and D final waves differ by a factor  $-2/\sqrt{5}$  and by the value of the coupling matrix element  $\mathcal{O}_{E_f a}^\ell$ . Due to this simple correspondence, in the following we will give the expressions for a final S symmetry only, since the extension to the D wave is straightforward. The other matrix element, corresponding to the transition between the ground  $|i\rangle$  and the intermediate state, reads

$$\begin{aligned} \langle \Psi_E^+ | P_z | i \rangle = & \langle E10 | P_z | i \rangle + \int dE' \langle E'10 | P_z | i \rangle \frac{V_{aE'}}{E - E' - i0^+} \frac{V_{Ea}}{E - E_a - i\Gamma_a/2} + \\ & + \mathcal{O}_{ai} \frac{V_{Ea}}{E - E_a - i\Gamma_a/2}, \end{aligned} \quad (3.60)$$

where  $\mathcal{O}_{ai}$  is the transition matrix element  $\langle a | P_z | i \rangle$  from the initial state to the bound component of the autoionizing state, which is related to Fano's  $q$ -parameter,  $q = \frac{\mathcal{O}_{i\tilde{a}}}{\pi V_{Ea} \mathcal{O}_{iE}}$ , where  $\tilde{a}$  is defined in Eq. (3.49). By replacing in Eq. (3.60) the dipole transition matrix element from the initial state to the unperturbed continuum, we obtain the final

expression

$$\begin{aligned} \langle \Psi_E^+ | P_z | i \rangle = & i \sqrt{\frac{4\pi}{3}} \left[ \overbrace{(2E)^{3/4} \phi_0(\sqrt{2E})}^C + \overbrace{\int dE' \frac{(2E')^{3/4} \phi_0(\sqrt{2E'}) V_{aE'}}{E - E' - i0^+} \frac{V_{Ea}}{E - E_a - i\Gamma_a/2}}^M \right] + \\ & + \overbrace{\mathcal{O}_{ai} \frac{V_{Ea}}{E - E_a - i\Gamma_a/2}}^B, \end{aligned} \quad (3.61)$$

where  $\phi_0(x)$  is the 1S hydrogenic function in momentum space. Each matrix element has three components, corresponding to the three components of the Fano function, i.e., the continuum (C), modified continuum (M) and bound (B) component. The two-photon transition matrix element, which comprise the product of the two matrix elements (3.60) and (3.59), can thus be written as the sum of nine terms:  $M_{2n\pm 1} = M^{CC} + M^{CM} + M^{CB} + M^{MC} + M^{MM} + M^{MB} + M^{BC} + M^{BM} + M^{BB}$ . We will designate each component with two superscripts accounting for the incoming (right) and the outgoing (left) amplitude. For example,  $M^{BC}$  will correspond to the transition from the ground to the continuum part of the Fano scattering state, and from the bound part of this state to the final state. The interested reader can find the explicit expression of the nine terms and their derivation in Appendix A. Here we give the final expression of the monochromatic two-photon matrix element,

$$\begin{aligned} \mathcal{M}_{2n\pm 1} = & \frac{\alpha^2 (2E_f)^{5/4} \phi_0(\sqrt{2E_f}) \sqrt{\pi} \omega_{ir}^{-1}}{3} \left[ \pm 2 + \frac{2i\Gamma_a}{E_f - E_a + i\Gamma_a/2} \left( \frac{\omega_{ir}}{\omega_i + \omega_{2n\pm 1} - E_a + i\Gamma_a/2} \mp 1 \right) \pm \right. \\ & \left. \pm \frac{i\Gamma_a}{\omega_i + \omega_{2n\pm 1} - E_a + i\Gamma_a/2} \right] + \frac{\alpha^2}{\omega_i + \omega_{2n\pm 1} - E_a + i\Gamma_a/2} \times \\ & \times \left[ \mp i \sqrt{\frac{2E_f}{3}} \mathcal{O}_{ai} \sqrt{\frac{\Gamma_a}{2\pi}} \omega_{ir}^{-1} + \pi \mathcal{O}_{E_f a}^S \sqrt{\frac{2\Gamma_a}{3}} (2E_f)^{3/4} \phi_0(\sqrt{2E_f}) + \mathcal{O}_{E_f a}^S \mathcal{O}_{ai} \right]. \end{aligned} \quad (3.62)$$

This expression contains the nine terms discussed, some of which have been cast in a simplified form and merged. From the nine initial terms, we have arrived at an expression with six final terms which are, by order of appearance in Eq. (3.62):  $M^{CC}$ ,  $M^{MC}$ ,  $M^{CM/MM}$ ,  $M^{CB/MB}$ ,  $M^{BC/BM}$  and  $M^{BB}$ . To obtain this expression we have assumed that the interaction between the bound and continuum,  $V_{aE}$ , as well as the radiative one-photon transition matrix elements  $\mathcal{O}_{ai}$ ,  $\mathcal{O}_{E_f a}^\ell$ ,  $\mathcal{O}_{E_f E}$  and  $\mathcal{O}_{Ei}$ , vary smoothly with energy across an interval of  $\Delta E \approx 2\omega_{ir}$ . In this way, we have reached an expression in which the only unknown parameters are the transitions to and from the bound part of the autoionizing state,  $\mathcal{O}_{ai}$  and  $\mathcal{O}_{E_f a}^\ell$ . Furthermore, as it was commented earlier,  $\mathcal{O}_{ai}$  is related to the Fano  $q$ -parameter, which is well-known for a vast majority of doubly-excited states.

Hence, the model only adds one extra parameter, namely, the strength of the transition between the bound part of the autoionizing state and the unperturbed continuum,  $\mathcal{O}_{E_f a}^\ell$ . Both of these transitions,  $\mathcal{O}_{ai}$  and  $\mathcal{O}_{E_f a}^\ell$ , are forbidden at the independent particle level because the dipole is a single-particle operator and its matrix elements between wave functions that differ by a double excitation, which is of course the case of doubly-excited states in helium, vanish. The reason why doubly-excited states are populated is because the wavefunction is not described by a single determinant, but by a mixture of configurations. Non-vanishing transition matrix elements to and from the bound components of the wavefunction are, thus, a measure of the correlation of the system.

### 3.5.2 Monochromatic vs Finite pulses.

When the radiation is monochromatic, then the atomic phase can be directly computed as was shown in Section 1.2.1,

$$\varphi_{2n\pm 1}^{at.} = \arg M_{2n\pm 1}. \quad (3.63)$$

When we have finite overlapping pulses, a wide energy spectrum  $\Delta\omega$  will be populated in the upper and lower harmonic as well as in the final sideband. This leads to many interfering quantum paths. To account for this, we need to make the convolution of both pulses. Assuming that the only relevant phase in the transition is the atomic phase,  $\varphi^{At.}$ ,

$$\begin{aligned} A_{2n\pm 1}^{(2)} &= -2i\pi \int d\omega A_{\text{IR}, \omega_{E_f g} - \omega}^* A_{\text{XUV}, 2n\pm 1, \omega} e^{-i\omega\tau_d} M_{2n\pm 1} \equiv \\ &\equiv |A^\pm| e^{i\varphi_{2n\pm 1}^{At.}}. \end{aligned} \quad (3.64)$$

$A_{\text{IR}/\text{XUV}, \omega}$  is the vector potential of the IR/XUV field,  $\omega_{E_f g} = E_f - E_g$  is the energy difference between the final state and the ground state, and  $\tau_d$  is the time delay between the center of the pulses.

The atomic time delay for both cases is given by

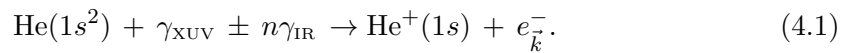
$$\tau_{at} = \varphi_{2n}^{At.} / 2\omega. \quad (3.65)$$

# Chapter 4

## Results

### 4.1 SPA to reproduce uncorrelated dynamics.

Here we will apply the methods described in Sec. 2.2 and Sec. 3.2 to compute the photoelectron energy and angularly resolved distribution for the photoionization of the helium atom from the  $1s^2$  ground state to the  $1s$  channel of the  $\text{He}^+$  parent ion in the energy region across the  $N = 2$  excitation threshold, within XUV-pump IR-probe schemes,



We will consider two cases: that of an XUV SAP and that of an APT.

#### 4.1.1 Single attosecond pulse case.

Let us consider the case of an isolated sub-femtosecond XUV pulse overlapped with an intense IR pulse first. A characteristic feature of such experiments is the streaking effect, i.e., an overall shift  $\Delta\vec{p} = -\alpha\vec{A}_{\text{IR}}(t)$  of the momentum distribution of the photoelectron generated by an attosecond XUV pulse centred at time  $t$ . The streaking effect, which has a purely classical explanation, has been one of the first means to achieve control over the photoelectron ejection process [22]. For XUV pulses with duration larger than the period of the IR dressing field, a transition from the streaking picture to the sideband picture, characteristic of monochromatic XUV fields [81], is observed. Kazansky *et al* [82] recently examined in detail this transition within the strong-field approximation. Here, we employ an XUV pulse with  $\text{fwhm}_{\text{XUV}} = 709$  as, comparable to a quarter of the

IR period,

$$\vec{A}_{\text{XUV}}(t) = A_{\text{XUV},0} \hat{\epsilon} \frac{\exp\left[-\frac{(t-t_{\text{XUV}})^2}{2\sigma_{\text{XUV}}^2}\right]}{\sqrt{2\pi}\sigma_{\text{XUV}}} \cos(\omega_{\text{XUV}}t), \quad \sigma_{\text{XUV}} = (8 \ln 2)^{-1/2} \text{fwhm}_{\text{XUV}}, \quad (4.2)$$

a choice situated at the boundary between the streaking and the side-band limits. The other pulse parameters used in the simulation are:  $\omega_{\text{XUV}} = 61.8$  eV,  $I_{\text{XUV}} = 0.1$  TW/cm<sup>2</sup>,  $\omega_{\text{IR}} = 1.55$  eV,  $I_{\text{IR}} = 1$  TW/cm<sup>2</sup>,  $\text{fwhm}_{\text{IR}} = 4.46$  fs. Both pulses are linearly polarized along the  $\hat{z}$  direction. We conducted simulations for three values of the carrier-envelope phase (CEP) of the IR pulse: 0°, 45°, and 90°. In the three cases, the centers of the XUV and the IR pulse coincide (zero time-delay). Since the duration of the XUV pulse is much shorter than the fwhm of the IR pulse, by changing the CEP we reproduce the case of a longer IR pulse where the time delay is changed instead. This approach is useful when conducting computationally-intensive simulations because it permits one to use short IR pulses thus keeping the overall propagation time to a minimum. The predictions of the SPA model were computed using the same set of parameters as in the simulation, with the exception of the fwhm of the IR field, which in this case is assumed to be monochromatic. In Fig 4.1 we compare the photoelectron spectra resulting from the *ab initio* calculations (Figure 4.1a-f) with those from the SPA model (Figure 4.1g-i). The latter have been scaled by a common factor to closely match the absolute value obtained from the simulation. In all cases, the colour-code corresponds to a logarithmic scale. The three panels on the left column (Figure 4.1a-c) show the photoelectron distribution in the  $(p_x, p_z)$  plane as it would appear after reconstruction [83] from experimental data recorded with a velocity-map imaging detector [3]. A dashed circle on top of the data, centred on the white cross along the vertical axis, indicates the expected position of the signal predicted by the streaking formula. To better appreciate the distribution details, the panels in the middle column (Figure 4.1d-f) illustrate the same quantity as in the left column in a energy vs.  $\cos\theta$  representation, where  $\theta$  is the photoelectron ejection angle with respect to the laser polarization. We can recognize four characteristic features. (I) Two dominant lobes, centred at  $\omega_{\text{XUV}} - IP$  in the case of CEP=0°, which (II) follow a clear streaking trajectory as the CEP of the dressing field is changed. In this representation and for the current IR intensity, the streaking effect appears as a tilt in the distribution. The prediction of the streaking formula is indicated with a dashed line. (III) For the case where the streaking is largest (Figure 4.1f), sidebands appear below the left and above the right lobe. Finally, (IV) narrow horizontal resonant features, due to the presence of doubly excited states, are visible. It is worth noting that, despite the opening of the 2*s* and 2*p* channels at  $E_e = 1.5$  a.u., the 1*s* spectrum is remarkably smooth across threshold. The three panels in the right column (Figure 4.1g-i) show the prediction of the SPA. The first three-dominant features of the *ab initio* angularly

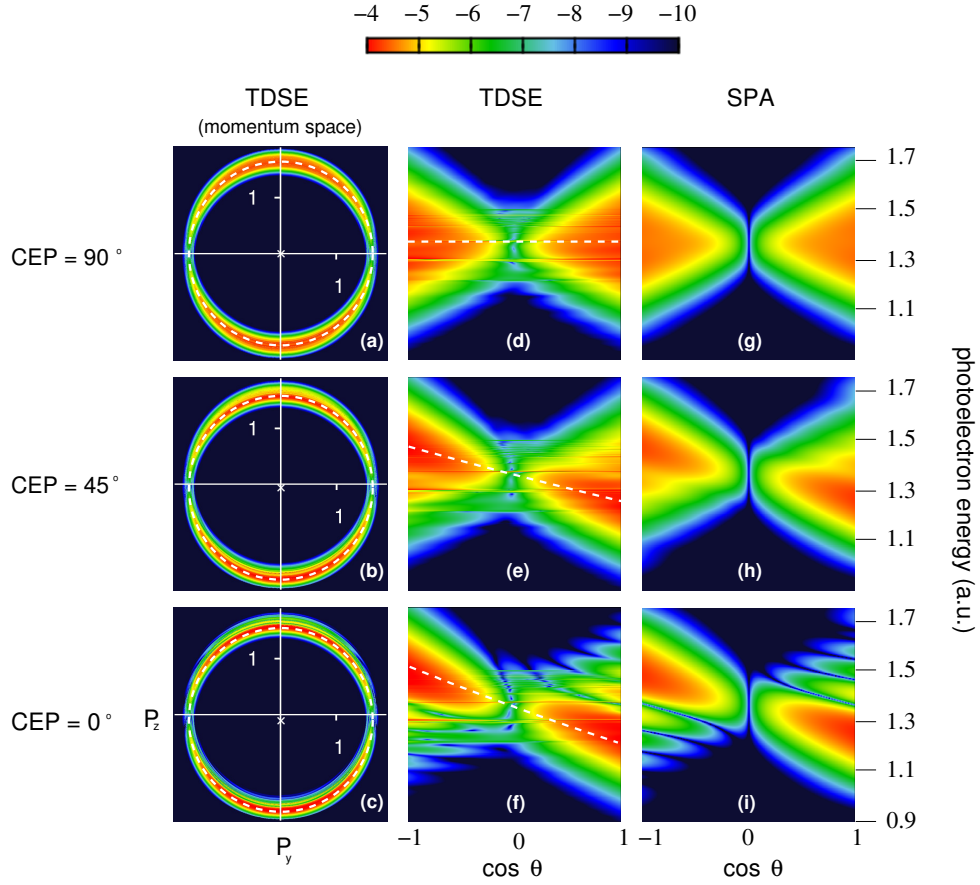


FIGURE 4.1: Comparison of photoelectron spectra in the 1s channel obtained by direct integration of the TDSE (a-f) with the prediction of the SPA (g-i) for the case where a helium atom is ionized by a SAP with central energy 61eV in the presence of an IR field ( $\lambda_{\text{IR}} = 800\text{nm}$ ,  $I_{\text{IR}}=1 \text{ TW/cm}^2$ ) at zero time delay. The three panel rows correspond to three different value of the cosine-modulated IR CEP:  $90^\circ$ ,  $45^\circ$ ,  $0^\circ$ . First column: section of the photoelectron momentum distribution in the  $xz$  plane. Second column: same distribution as in the first column but in the representation photoelectron energy vs. cosine of the photoelectron ejection angle with respect to the laser polarization. Third column: prediction of the monochromatic SPA. The color code is on a  $\log_{10}$  scale. The reported signal is a probability density per unit of cubic linear momentum (first column) or per unit of energy (second and third column), in atomic units.

resolved spectra, (I-III), are accurately reproduced. In particular, the sidebands in Fig 4.1f are an interference effect of quantum streaking (Figure 4.1i is analogous to Figure 4a in [84]) instead of a consequence of the presence of intermediate doubly excited states. Such interference effect is due to the fact that, if the duration of the SAP used in the pump-probe ionization is comparable to half period of the IR, the streaking is not uniform across the pulse. When the center of the XUV pulse coincides with the zero of the vector potential (Figs. 4.1a,d,g), the IR accelerates the photoelectrons ejected in any given direction upward during the first half of the XUV pulse and downwards during the second half. As a consequence, the spectrum of the photoelectron is widened. Furthermore, the wave-packet in the upward direction acquires a negative chirp (not

visible in the energy-resolved signal) while the one heading downward acquires a positive chirp. In the case the centre of the XUV pulse coincides with the maximum of the vector potential (Figs. 4.1c,f,i), the energy bandwidth in either the lower or the upper lobe is smaller than in the previous case. The ionization amplitude generated at times  $t_1 = t_{\text{XUV}} - \Delta t/2$  and  $t_2 = t_{\text{XUV}} + \Delta t/2$  which are symmetric with respect to the XUV pulse centre are equally streaked by the IR, leading to the interference fringes above the upper and below the lower lobe. This example illustrates how the SPA can be used to reproduce with remarkable accuracy all background features of photoelectron angular distributions in realistic systems, even in the presence of transiently bound states. Since the optical transition to these states from the ground state is forbidden at the level of the independent particle model, their influence in the spectrum is comparatively minor.

#### 4.1.2 Attosecond pulse train case; effect of finite probe duration.

Let us now consider the case of a train of attosecond pulses comprising a sequence of Gaussian XUV pulses, with central energy  $\omega_{\text{XUV}} = 60.29$  eV and fwhm=192 as, separated by half the period of the IR probe pulse and with alternating sign; the train envelope has a duration of 6 fs and a maximum intensity  $I_{\text{XUV}} = 0.1$  TW/cm<sup>2</sup>. As in the SAP, we conduct the *ab initio* simulation with a short (fwhm<sub>IR</sub> = 5.36 fs) moderately intense ( $I_{\text{IR}} = 1$  TW/cm<sup>2</sup>) IR pulse. On the one hand, as anticipated in previous sections, the use of a short IR pulse significantly reduces the computational burden while at the same time reproducing most of the feature observed in realistic experiments, in which the length of the IR pulse associated to XUV trains is often larger. On the other hand, since the duration of the XUV train and the IR pulse are now comparable, some effects due to the fact that the IR intensity is not uniform across the train are to be expected. For a meaningful comparison with the experiment, therefore, it is important to be able to identify and factor out such effects. In Figure 4.2 we compare the photoelectron angular distribution for a fixed time delay  $t_d = -T_{\text{IR}}/4 = -0.666$  fs computed with: (a) *ab initio* simulation, (b) SPA model with a monochromatic IR field, and (c) SPA model with a pulsed IR field. All three methods predict a minimum in the harmonic signal at  $\sim 60^\circ$  from the polarization axis. This is an extreme example of the angular broadening observed experimentally and reproduced with single-active-electron simulations by Guyetand *et al.* [85]. In [86], the phenomenon was justified on the basis of the perturbative limit of the soft-photon approximation. Indeed, third-order corrections to the harmonic amplitude that come from the absorption or emission of two IR photons have an angular distribution proportional to  $\cos^3 \theta$ . The interference term with the first-order amplitude, which is proportional to  $\cos \theta$ , therefore, gives rise to a  $\cos^4 \theta$  term which alters the harmonic signal predominantly along the polarization

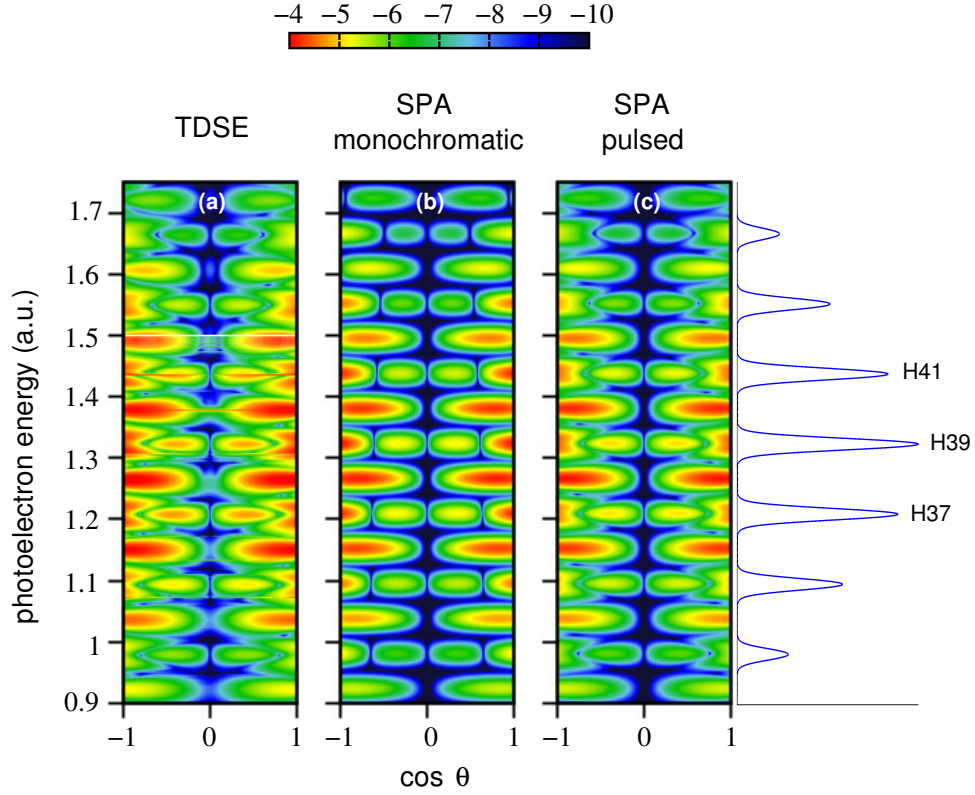


FIGURE 4.2: Calculated photoelectron spectra for the case where a helium atom is ionized by an attosecond pulse train with energy 61eV in the presence of an IR field ( $\lambda_{\text{IR}} = 800\text{nm}$ ,  $I_{\text{IR}} = 1 \text{ TW}/\text{cm}^2$ ). Panel (a) represents the full calculation of the TDSE, using a cosine-square envelope for the IR probe pulse, while panels (b) and (c) were calculated using the SPA for: (b) a monochromatic IR pulse and (c) a cosine-square modulated IR pulse.

axis. The agreement of the monochromatic model (Figure 4.2b) with the simulation (Figure 4.2a), however, is not as impressive as for the SAP. In the simulation, the odd-harmonics signals next to the polarization axis are clearly split, a feature that the monochromatic model does not reproduce. That this feature is due to the finite duration of the probe pulse and not to the correlated electron dynamics in the atom is clearly demonstrated by the impressive agreement with the third panel, obtained with the pulsed SPA model. Indeed, apart from the missing narrow resonant lines associated to He doubly-excited states, the pulsed model is able to reproduce all the background features of the simulated spectrum. This splitting affects both the angular and the energy distribution of the harmonic signal. Therefore, it should be taken into account when assessing the effects of multi photon transitions and Coulomb corrections to the soft-photon model with short pulsed radiation.

Figure 4.3 compares the angularly-integrated photoelectron spectra computed with *ab initio* simulations and with the pulsed SPA model for five different time delays between

the two pulses:  $-1.33$  fs,  $-0.67$  fs,  $0$  fs,  $0.67$  fs, and  $1.33$  fs (Figs. 4.3a through e, respectively). Again, apart from the resonant features, the agreement between model and simulation is very good across the whole IR period and energy range. In conclusion, the

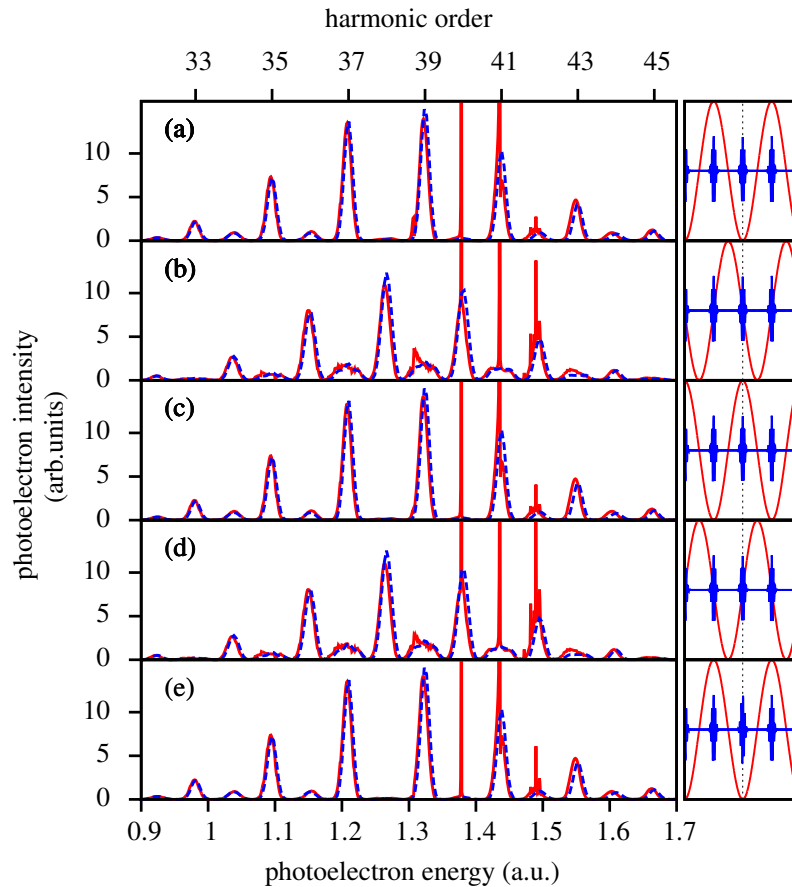


FIGURE 4.3: Total photoelectron distribution of a helium atom ionized by an attosecond XUV pulse train of central frequency  $61\text{eV}$  in the presence of an IR dressing pulse ( $\lambda_{\text{IR}} = 800\text{nm}$ ,  $I_{\text{IR}} = 1\text{ TW/cm}^2$ ) for five different time stages: (a) XUV at the minimum of the vector potential; (b) XUV at inflection point; (c) XUV at maximum of vector potential; (d) XUV at inflection point (half an IR period later than case (b)); (e) XUV at minimum of vector potential (one IR period later than in case (a)). Red solid line: numerical solution of the TDSE. Blue dashed line: pulsed SPA model.

pulsed version of the SPA model is able to reproduce the consequences of a finite duration of the IR dressing pulse on the fully differential photoelectron distribution. Possible application of such extended model include interpretation of photoelectron angular distributions in real experiments, refinements of the RABITT protocol, and assistance in the interpretation of *ab initio* simulation in the presence of features beyond the reach of a single-active-electron model, like autoionizing states and above-threshold multi-channel interactions. This last point has been used in this work to help isolate the features of doubly excited states in Sec.(4.2).

### 4.1.3 Attosecond pulse train case; effect of high probe intensity.

The variation of sideband intensity as a function of the time delay is a major observable in pump-probe experiments based on the use of attosecond pulse trains. In the following, we shall examine how such variation is affected by the intensity of the dressing field. To focus on this aspect without the interference of either finite-pulse or correlation effects, we will consider the monochromatic version of the SPA model only. As long as the IR pulse is longer than 3 – 4 times the APT duration, this approximation is justified. In Figure 4.4 we report the photoelectron spectrum computed with the monochromatic and pulsed version of the SPA model in the case of an APT with the same parameters as in Figure 4.3b but where the IR pulse has a much larger duration,  $\text{fwhm}_{\text{IR}} = 21.78$  fs. In these conditions, the consequences of a finite duration of the IR pulse are indeed sufficiently small to leave the most prominent features of the photoelectron spectrum dependence on laser intensity unaltered.

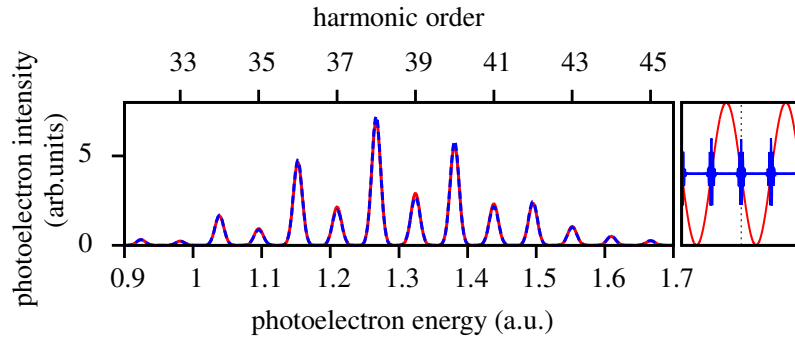


FIGURE 4.4: Photoelectron energy spectrum for the ionization of the helium atom from the ground state by means of a RABITT pump-probe scheme, computed with two different models: monochromatic SPA (red solid line) and pulsed SPA (blue dashed line). The pulse parameters are the same as in Figure 4.3 except for the modulation of the IR field in the pulsed model, which here reproduces an IR pulse with duration much larger than that of the APT,  $\text{fwhm}_{\text{IR}} = 21.78$  fs,  $\text{fwhm}_{\text{APT}} = 6$  fs. In these conditions, the boundary effects associated to the finite duration of the dressing field (pulsed case) are negligible: the spectrum is well reproduced within the infinite-pulse approximation (monochromatic case).

In the perturbative limit, the sideband signal is known to oscillate at the fundamental RABITT angular frequency  $2\omega_{\text{IR}}$ . As discussed in Sec. 3.2.3, however, as the intensity of the dressing field is raised, overtone components with angular frequency  $2n\omega_{\text{IR}}$  start to appear. Figures 4.5a-e (left panels) show the integrated intensity of a central sideband as a function of the time delay across half a period of the IR for several values of the IR reduced field strengths  $\xi$ . For each intensity, three curves are plotted: one obtained with the analytical formulas in the frequency-comb limit, and two others computed with the monochromatic SPA model with parameters chosen either to approach the

frequency-comb limit ( $\text{fwhm}_{\text{XUV}} = 50$  as,  $\text{fwhm}_{\text{APT}} = 24$  fs) or to reproduce ordinary experimental APT parameters ( $\text{fwhm}_{\text{XUV}} = 263$  as,  $\text{fwhm}_{\text{APT}} = 11$  fs). Even for moderate

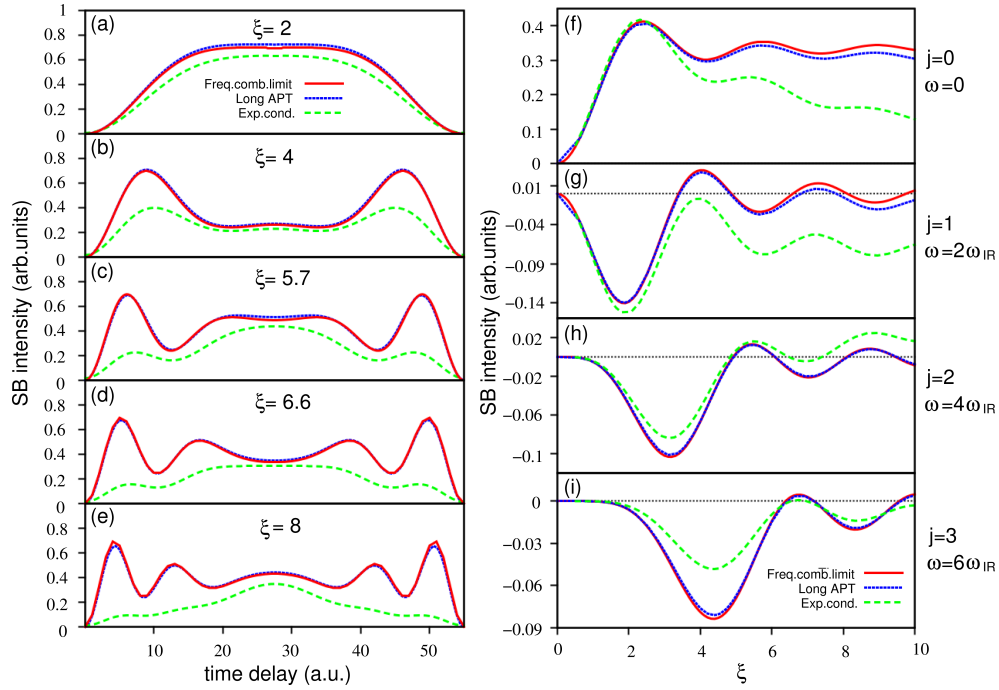


FIGURE 4.5: Left panels (a-e): energy integrated photoelectron signal of a central sideband as a function of the time delay between an XUV APT and a monochromatic IR probe for five different values of the reduced field strength  $\xi$ ; from top to bottom:  $\xi = 2$  a.u., 4 a.u., 5.7 a.u., 6.6 a.u., 8 a.u., corresponding to IR intensities, for a photoelectron with  $E_e = 1$  a.u., of 4.08 TW/cm<sup>2</sup>, 16.3 TW/cm<sup>2</sup>, 33.1 TW/cm<sup>2</sup>, 44.4 TW/cm<sup>2</sup>, and 65.3 TW/cm<sup>2</sup>, respectively. Frequency comb limit: solid red line; SPA for an XUV APT in close to the frequency comb limit (train duration=24fs, pulse duration=50as): dotted blue line; SPA for an XUV APT with common experimental parameters (train duration=11fs, pulse duration=263as). Right panels (f-i): coefficients  $C_j(\xi)$ ,  $j = 0, 1, 2, 3$  (top to bottom) of the harmonic components of the time-dependent integrated sideband signal (see text), as functions of the reduced field strength  $\xi$ , for the same three models as in the left panels.

field strengths, the time-delay dependence of the sideband signal deviates significantly from the characteristic sinusoidal modulation of the perturbative limit (1.7). For values of the reduced field strength of the order of 3 ( $I_{\text{IR}} \sim 10$  TW/cm<sup>2</sup> at  $E_e = 1$  a.u.), multiple maxima start to appear. In the case of a realistic APT, the sharp modulations predicted in the frequency-comb limit are somewhat washed out as a consequence of the finite energy span and duration of the APT. Yet, even with these realistic pulses, the qualitative change of the profile is still clearly visible.

The time dependence of the sidebands can be parametrized in terms of a discrete Fourier series which, for parity reasons, comprises only even multiples of the IR fundamental

frequency (see Equation (3.35))

$$I_{\text{SB}}(t; \xi) \propto \sum_{j=0} \cos(2j\omega_{\text{IR}}t) C_j(\xi). \quad (4.3)$$

In Sec. 3.2.3 we derived an analytical expression for the amplitudes  $C_j(\xi)$  of the harmonic components in the frequency comb limit. Figures 4.5.f-i (right panels) show the coefficients of the average sideband signal  $C_0$ , of the fundamental RABITT modulation  $C_1$ , and of the first two overtones  $C_2$  and  $C_3$ , as a function of the reduced field strength for the same three models used in the left panels. The most striking feature of these plots is that all  $C_j(\xi)$  amplitudes are predicted to oscillate periodically as the intensity of the laser increases. In particular, the fundamental modulation  $C_1$  below  $\xi = 10$  ( $I_{\text{IR}} \simeq 10^{14}$  W/cm<sup>2</sup> for  $E_e = 1$  a.u.) changes sign five times in the frequency comb limit, and even for the shortest APT it vanishes almost entirely for  $\xi \simeq 4$  ( $I_{\text{IR}} \simeq 1.6 \cdot 10^{13}$  W/cm<sup>2</sup> for  $E_e = 1$  a.u.). Close to these intensities, overtones dominate. In [79], L'Huillier and co-workers reported measurements of the phase of the  $4\omega_{\text{IR}}$  and of the  $6\omega_{\text{IR}}$  overtones. Therefore, even if the authors did not report or comment on the dependence of the amplitude of the overtone components on the laser intensity, the determination of the oscillations shown in Figure 4.5.b should be well within the reach of current laser technology. In [79], the authors concluded that the appearance of overtones was to be associated to a loss of accuracy and a bias towards artificially compressed attosecond pulses in the RABITT reconstruction protocol. In fact, within the soft-photon approximation it is possible to keep track of all sideband frequency components even for large intensities, as soon as the experimental contrast and time-delay resolution is sufficiently high. The frequency-comb limit of the SPA can thus conceivably be the basis for an extension of the RABITT protocol to non-perturbative regimes.

## 4.2 RABITT for the study of doubly excited states.

In the following, we apply the methods described in Sec. 2.2 and Sec. 3.5 to analyze the radiative continuum-continuum transitions in the presence of autoionizing states from the phases of the sidebands obtained by means of a RABITT pump-probe scheme. In the same way that in the previous section, we concentrate on the photoionization of the helium atom below the N=2 ionization threshold.

### 4.2.1 Intermediate bound state.

Fig.(2.4) in Sec. 2.2.0.1 showed that the atomic phase  $\eta_\ell$  changed by  $\pi$  as the energy crossed a transiently bound state. If we consider first the simple case of a two-photon

transition from the ground to a final continuum state passing through an intermediate Rydberg state, then, the phase of the sideband will be given by the resolvent phase,

$$\arg[G_0^+(E)] = -\pi/2 + \arctan\left(\frac{E - E^{\mathcal{R}}}{\Gamma/2}\right), \quad (4.4)$$

which indeed exhibits a  $\pi$  phase shift modulated by the width of the state, like that of Fig.(2.4). A RABITT scheme involving an intermediate Rydberg state in one path and an intermediate continuum state in the other, should exhibit the described phase behaviour. A first experimental confirmation of this prediction was provided by Swoboda *et al.* [32] in 2010. In the same basis, Caillat *et al.* showed that the same behaviour can be observed in correspondance of a shape resonances in the N<sub>2</sub> molecule [87]. Starting from these premises, we performed the study for autoionizing states. Of course, for DES, theoretical methods to describe the full solution can no longer rely on the Single Active Electron approximation (SAE), where ionization is described as a one electron process in which all the remaining (non-ejected) electrons act as frozen spectators. Here, we give the full solution of the TDSE for two photon transitions with autoionizing states as well as the solution of the analytical monochromatic model presented in the previous chapter.

As in the previous section, we will consider a helium atom singly ionized by an XUV pulse train in the presence of a dressing IR field, in the usual RABITT scheme. We carried out several simulations in which we varied the laser frequency in order to analyze various transitions and to show the variation of the phase as a function of the detuning from the resonance. Examples of possible transitions can be seen in Fig.(4.6).

### 4.2.2 Measurable phase shift.

To begin the study, we consider the same pump-probe scheme as in Sec.(4.1.2). The IR laser frequency was set to  $\omega_{\text{IR}} = 0.05711986$  a.u., which permitted to populate the doubly excited states  $\text{sp}_2^+$  ( $E_r = -0.693$  a.u.,  $\Gamma = 1.37 \cdot 10^{-3}$  a.u. [88]) and  $\text{sp}_3^+$  ( $E_r = -0.564$  a.u.,  $\Gamma = 3 \cdot 10^{-4}$  a.u. [88]) in harmonics 39 and 41 with detunings of  $1.7 \cdot 10^{-2}$  a.u. and  $2.3 \cdot 10^{-3}$  a.u., respectively. In addition, sideband 40 populates the doubly excited state  $2\text{p}^2$  ( $E_r = -0.622$  a.u.,  $\Gamma = 2 \cdot 10^{-4}$  a.u. [89]) with a detuning of  $3.1 \cdot 10^{-3}$  (sidebands populate states with even symmetry). The full width at half maximum (fwhm) of the IR pulse was 5.36 fs, and was simulated using a cosine-square envelope. For the XUV train, the fwhm was 6 fs corresponding to a spectral bandwidth of  $\Delta\omega \approx 0.02$  a.u., and was simulated using a gaussian envelope. The populated spectrum ranged from a value of  $E=0.9$  a.u. to  $E=1.5$  a.u. of the photoelectron energy. We chose this system to conduct a preliminary study since it contained all relevant transitions: C-C-C for SB 36, C-C-R for SB 38, R-R-R for SB 40, R-R-MC for SB 42, where MC stands for multichannel

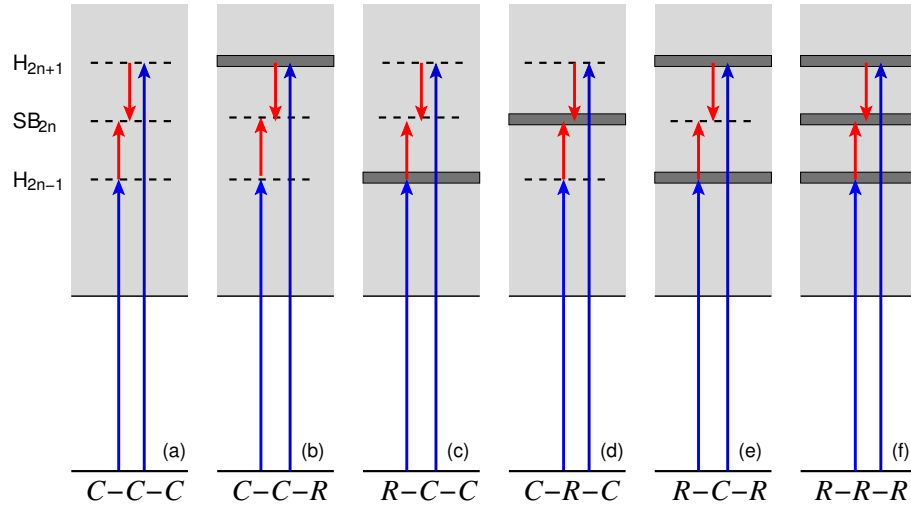


FIGURE 4.6: Different types of resonant transitions. The thick dark bars represent a doubly excited state and the dashed lines a purely continuum state. For all cases we start from the same state and, by means of a two-photon transition, we populate the final state  $SB_{2n}$ . This final state can be populated via two different paths, either by absorption of an XUV photon with energy  $\omega_{2n-1}$  plus an absorption of an IR photon of energy  $\omega$ , or by an absorption of an XUV photon of energy  $\omega_{2n-1}$  plus a stimulated emission of an IR photon of energy  $\omega$ . (a) corresponds to the case in which all populated states (intermediate and final) are purely continuum C states. (b) and (c) describe the cases in which a doubly excited resonant R state is contained in an upper and lower intermediate state, respectively. In (d) the final state contains a doubly excited state, (e) has one doubly excited state in each of the intermediate states and (f) has doubly excited states in both intermediate states as well as in the final state.

continuum ( $H_{43}$  lies above the  $N=2$  threshold). The multichannel case is beyond the scope of this master thesis and will not be examined further. In Fig.(4.7) we report the total photoelectron spectrum as a function of the time delay between pump and probe pulses. We notice thin intense lines in correspondence of the autoionizing states, which would lead to enhanced multiphoton transitions (REMPI), as in the case of bound Rydberg states. A closer look at sideband 40 (Fig.(4.8)) shows a clear phase shift of the resonant part (the  $2p^2$  DES) of the sideband. However, resolving energetically this thin intense state requires an energy resolution finer than the width of the resonance (of the order of  $10^{-3}$  a.u.), which is still not available at high harmonic facilities. To show this effect can still be experimentally observed, we integrated over all the energies of the sideband for different time delays. Making the discrete fourier transform (DFT) of these values, gave us a global phase of each sideband that we show in Table 4.1.

The phase dependence on the detuning from a resonance can be inferred from the third value in Table 4.1. In this case, we have a C-C-R transition, but the DES is populated by the tail of the harmonic, since the detuning is of the order of the spectral bandwidth of the pulse. Due to this, we only see a small phase change with respect to a C-C-C transition. Finally, we would like to remark that the phase due to C-C-C transitions

( $\sim 3.21\text{rad}$ ) differs slightly from the soft photon value  $\pi$ . Indeed, the phase shift of continuum states in absence of resonances, though smoothly, still vary with energy.

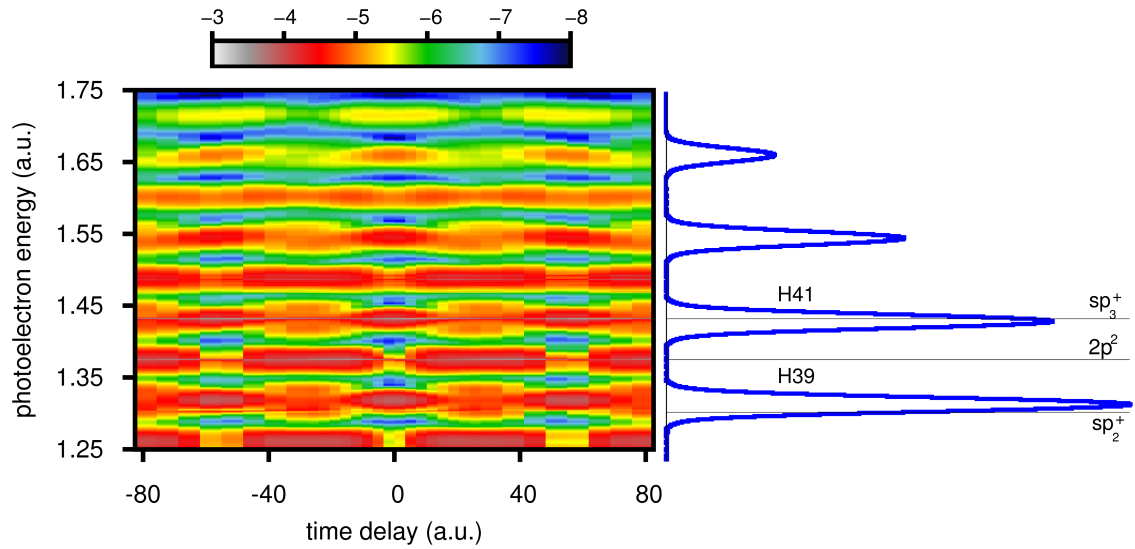


FIGURE 4.7: Photoelectron spectrum as a function of pump-probe time delay in logarithmic scale below and above the  $N=2$  single ionization threshold ( $E=1.5$  a.u.) of helium for a RABITT scheme with the parameters:  $\omega_{\text{IR}} = 0.05711986$  a.u.,  $\omega_{\text{xUV}} = 2.21576$  a.u.,  $fwhm_{\text{IR}} = 5.36$  fs,  $fwhm_{\text{xUV}} = 6$  fs. Both harmonics and sidebands oscillate as a function of the time delay between both pulses due to the interference of the two quantum paths (see Fig.(4.6)).

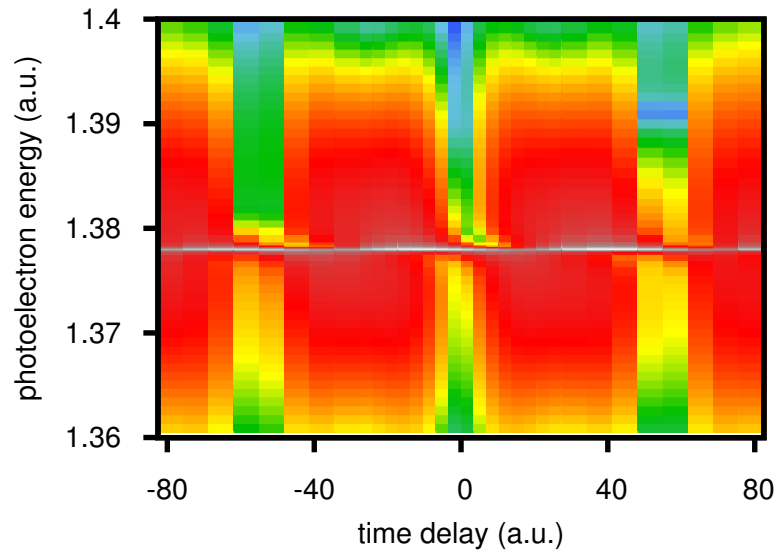


FIGURE 4.8: Close up of Fig.(4.7) in the energy region corresponding to sideband 40, which contains the doubly excited state  $2p^2$  (grey line). The doubly excited state oscillates with a different phase than the continuum background it is embedded in.

Transition	Detuning	$\varphi_{\text{SB}}$ (rad)
C-C-C	-	3.21
C-R-C	0.002	3.23
C-C-R	0.017	3.19
R-R-R	0.017-0.006-0.002	2.82
R-R-MC	0.006-0.002	3.40

TABLE 4.1: Phases of the sidebands obtained by the simulation for five different types of transitions (see Fig.(4.6)). In the left column we indicate the type of transition; in the center column we show the detuning from the resonance (of the harmonic, the sideband or both) in those cases where there is one or more resonant transitions; and in the right column we report the global phase of the sideband, obtained by integrating over all the sideband energies for different phase time delays and making a discrete fourier transform.

### A particular case. The C-R-C transition.

Fig. (4.8) showed that resonances in the final states contribute with an additional phase shift beyond the one that is observed when the autoionizing state is only in the intermediate state. In this particular example, the  $2p^2$  state induced a further shift on the already shifted background. However, if DES are present *only* in the final states, no phase shift occurs. We carried out another simulation in which we kept the same parameters as in the previous simulation with the exception that the driving laser frequency was now tuned to  $\omega_{\text{IR}} = 0.05067$  a.u., in order that SB 42 corresponded to a C-R-C transition. The phase shift for this transition is shown in the third value of Table 4.1, where we see that, eventhough the detuning of the sideband with respect to the resonance energy is small, there is no appreciable phase shift induced.

### 4.2.3 Photoelectron Angular Distributions.

The signatures of doubly excites states are particularly evident in the photoelectron angular distribution (PAD) at resonant energies. Resonant PADs are very sensitive to the time delay between both pulses, and often deviate dramatically from nonresonant PAD shapes, which tend to concentrate along the polarization axis of the impinging laser. Fig.(4.9) shows the PAD at the energy of the  $2p^2$  DES, which corresponds to sideband SB40 (mixture of S and D waves), for nine different pump-probe time delays.

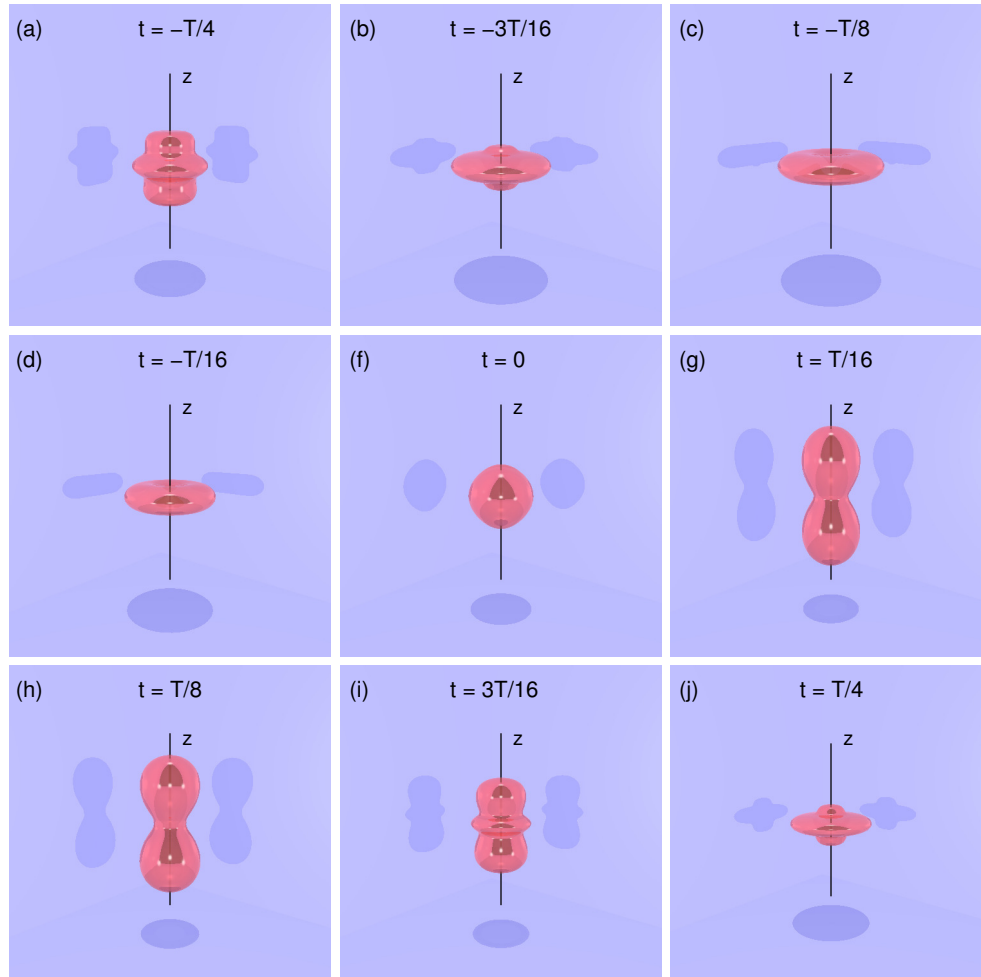


FIGURE 4.9: Photoelectron angular distribution (PAD) at the energy of the  $2p^2$  doubly excited state for nine time delays between the two pulses in steps of  $1/16$ th of the IR period. The three shadowed areas correspond to the 2-D projection of the distribution in each of the three axis (polarization is in the  $z$ -direction). The distributions correspond to a mixture of S and D waves, that change dramatically their relative weight as a function of the time delay.

#### 4.2.4 Transitions with an intermediate resonant state.

In order to isolate the effects of a single autoionizing state, we now propose to study how the sideband phase varies as a function of the detuning in a C-C-R transition, in which we have a resonance in an intermediate state (fig.(4.6b)). The same results apply for R-C-C transitions and they can be straightforwardly generalized to R-C-R transitions. In the *ab-initio* simulation, to reproduce a typical pump-probe experiment, we used finite pulses with a duration which is generally much shorter than the lifetime of the autoionizing states involved. Hence, finite-pulse effects are bound to appear. To study the relation between the phase shifts and the different parameters that appear in the radiative atomic transitions, we used the parametrized model developed in Section 3.5.

The phases thus calculated can then be related to the photo ejection time delays by Eq. (3.65).

#### 4.2.4.1 Ab-initio simulations.

We performed several simulations for the same pump-probe scheme for various values of the driving laser frequency. The XUV train central frequency and FWHM, and the FWHM of the IR field were kept the same for all simulations at the values of 2.1566 a.u., 4.6 fs ( $\Delta\omega_{\text{IR}} \approx 0.03$  a.u.) and 8 fs ( $\Delta\omega_{\text{XUV}} \approx 0.015$  a.u.), respectively. We chose to study the transitions involving the  $\text{sp}_2^+$  DES, which we populated with Harmonic 41 at different detunings (using different driving laser frequencies). We made sure that H 39 and SB 40 were not resonant with any DES. The phase shift of SB 40 was then studied as a function of the IR frequency for a range of frequencies that went from  $(E_r - 8\Gamma)$  to  $(E_r + 8\Gamma)$ , where  $E_r$  and  $\Gamma$  are the resonance energy and width, respectively. Fig.(4.10) reports the oscillation of SB 40 as a function of the time delay between pump and probe pulses for an interval of half an IR period. We observe a clear deviation of the maximum as the detuning is lowered. To see the phase shift more clearly, we performed a discrete fourier transform to this oscillations to obtain the phase and compared the results with those that come out of SB 38, which was a pure C-C-C transition. These results are shown in Fig.(4.11), in which we indicated with two dashed lines the range of frequencies,  $\omega_{\text{IR}}$ , for which  $41\omega_{\text{IR}}$  (the center of the 41st harmonics) overlaps with the resonance (that spans the energy region from  $E_r - \Gamma/2$  to  $E_r + \Gamma/2$ ). We observe that the phase dips for values of the laser frequency close to the resonance. When the 41st harmonic and the resonance overlap, the phase drops by  $\sim 0.6$  rad, which is experimentally observable. It is worth mentioning that the use of finite pulses washes-out the  $\pi$  phase shift observed by [32, 87] in bound states and shape resonances. Indeed, the pulsed radiation populates a coherent superposition of continuum states across a wide energy range, where the doubly excited states contribute only with a small fraction to the total oscillator strength (see fig.(4.8)). Hence, it is expected that the phase shift would be modified slightly, as it indeed is. This phase can be theoretically calculated using the expression for the time-dependent second-order perturbative transition amplitude for finite pulses (Eq. (3.64)). In the next section, we will examine the effects of using monochromatic light with the model developed in Sec.(3.5). We anticipate that even in the limit of monochromatic light, one should not expect a  $\pi$  jump to occur in transitions involving autoionizing states.

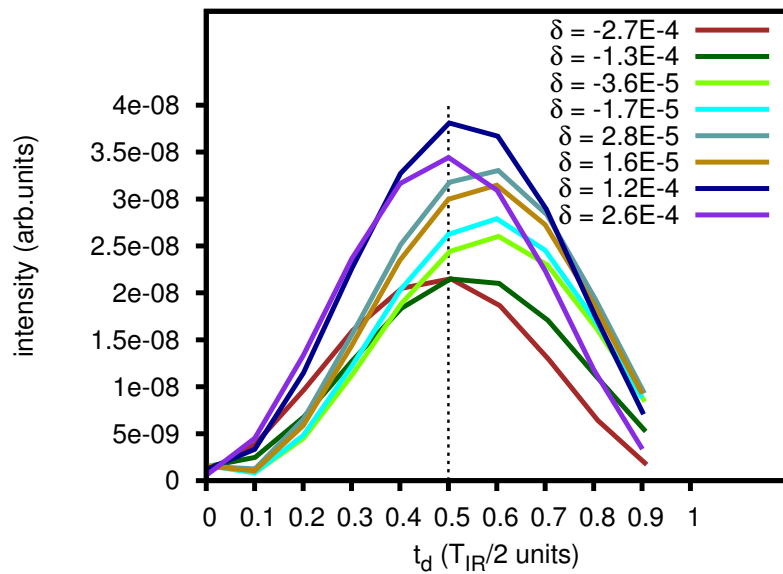


FIGURE 4.10: Oscillation of the 40th sideband for eight different IR frequencies calculated by the simulation as a function of the time delay across an interval of half IR period. For a structureless continuum, the maximum of the sideband should correspond to  $0.5 \cdot T_{\text{IR}}/2$  (dotted black line). We notice that the closer the frequency is to the resonance, the more shifted is the peak of the sideband from this value.

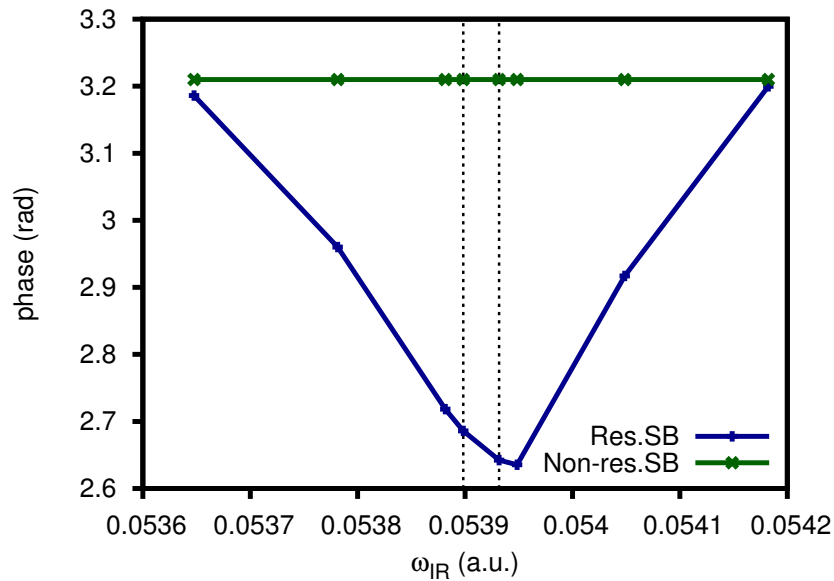


FIGURE 4.11: Variation of the phases of two sidebands as a function of the IR laser frequency. The two dashed lines correspond to the range in which the center of the spectrum of the 41st harmonics overlaps with the  $sp_2^+$  resonance. The blue line corresponds to a sideband populated by a C-C-R transition, while the green line is populated by a C-C-C transition. For the resonant case, as the 41st harmonic frequency of the laser gets closer to the energy region of the resonance, a clear phase shift is observed.

#### 4.2.4.2 Monochromatic Model.

We now propose to study more in depth the connection between the atomic phases and the transition matrix elements involving doubly excited states with the parameters of the model described in Sec.3.5. To do this, we analyze a variety of cases, in which the transition matrix elements from the ground to the bound-component of the resonant state,  $\mathcal{O}_{ai}$ , and from the bound-component to the final continuum state,  $\mathcal{O}_{E_f a}^S$ , are varied. For all of the cases except the first we plotted the argument of the two-photon transition matrix element in Eq. (3.62) as a function of the laser frequency (and, thus, of the detuning from the resonance). The resonance parameters were taken to be those of  $sp_2^+$ , which were discussed above. The frequencies used ranged from  $(E_a - 8\Gamma)$  to  $(E_a + 8\Gamma)$ . Figs. (4.12-4.17) show the phase variation of the six individual terms in Eq. (3.62) in the frequency region of interest. The different proportion of these terms, governed by the strengths of  $\mathcal{O}_{ai}$  and  $\mathcal{O}_{E_f a}^S$ , in the final transition matrix element will dictate the final phase of the sideband in the monochromatic limit.

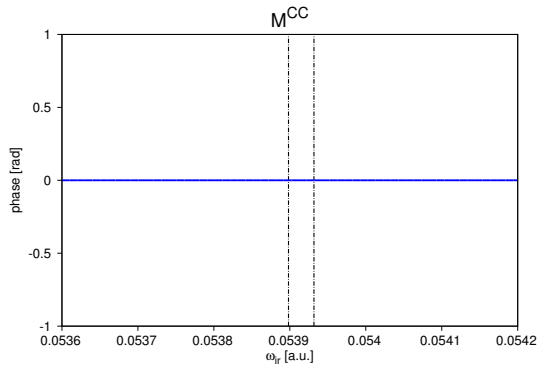


FIGURE 4.12

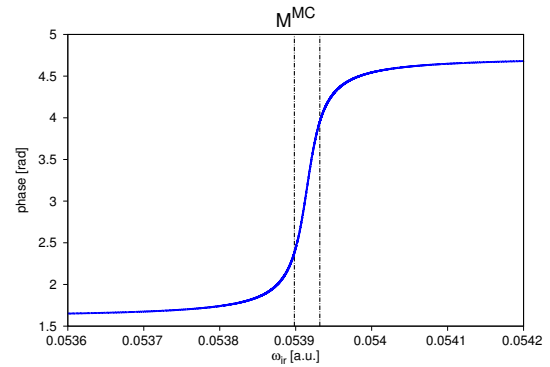


FIGURE 4.13

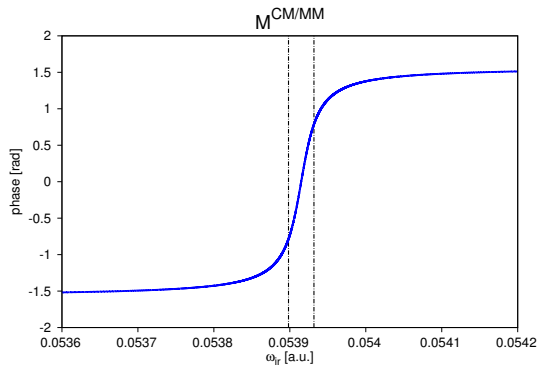


FIGURE 4.14

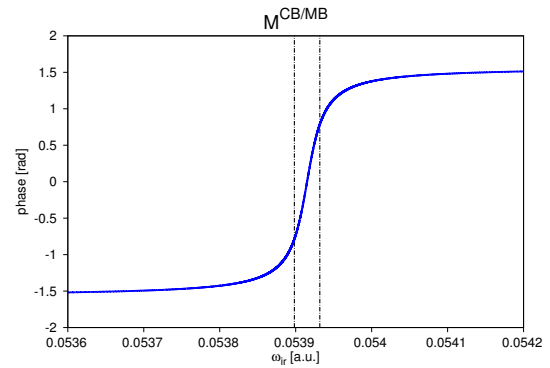


FIGURE 4.15

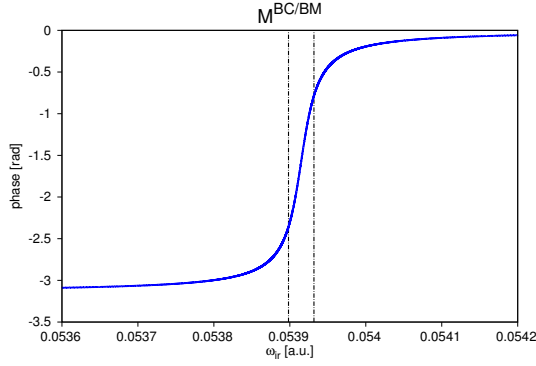


FIGURE 4.16

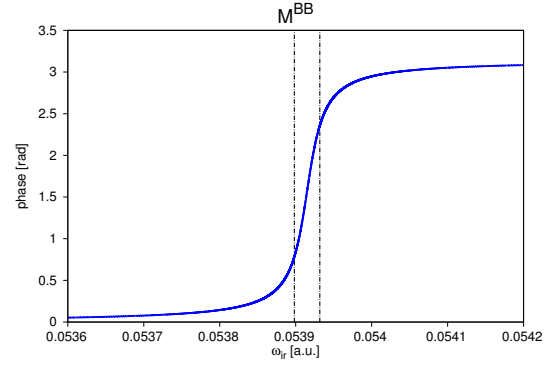
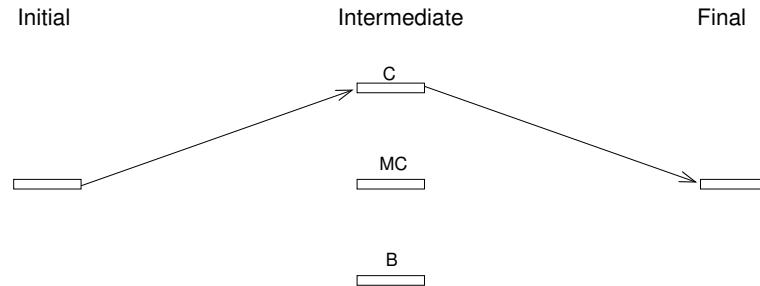


FIGURE 4.17

(i).  $\Gamma_a = 0$ ,  $\mathcal{O}_{ai} = 0$ ,  $\mathcal{O}_{Efa} = 0$

This case corresponds to a non-interacting bound component  $|a\rangle$  and continuum  $|E\rangle$  ( $V_{aE} = 0$ ), and no transition from the ground to the bound component ( $\mathcal{O}_{ai} = 0$ ), i.e., a pure continuum-continuum transition (see Fig.(4.18)). In this case, the only non-vanishing term in the model is  $M^{CC}$ . It is the limit of the non-resonant case, in which  $\varphi^{at.} = 0$ .



(i)

FIGURE 4.18: Sketch of the possible incoming/outgoing amplitudes for (i). The transition takes place from the initial state to the continuum component of the intermediate state and from this to the final state. There is no interaction between the different components of the intermediate state.

(ii).  $\Gamma_a = 0$ ,  $\mathcal{O}_{ai} \neq 0$ ,  $\mathcal{O}_{Efa}^S \neq 0$

The transition through the unperturbed continuum and the resonance are independent and interfere in the final state. Thus, the two-photon transition matrix element in this case comprises only two terms:  $M^{CC}$  and  $M^{BB}$  (fig.(4.19)). The sideband phase-shift for these conditions are shown in Fig. (4.20). We chose two values of  $\mathcal{O}_{ai}$  and  $\mathcal{O}_{Efa}^S$  (0.1

a.u., blue solid line, and 1.0 a.u., green dashed line) that are indicative of the phase behaviour in this case. For  $\omega_{\text{IR}} < (E_a - IP)/41 = 0.053915$  a.u., both values give the same behaviour, the atomic phase is zero. As the laser frequency crosses the center of the resonance, a brusque  $\pi$  jump occurs due to the change of sign of the  $M^{BB}$  term (see Fig. (4.17)). The jump is sudden due to the fact that the width of the resonance is zero. The change of phase indicates that for the value of  $\mathcal{O}_{ai}$  and  $\mathcal{O}_{E_f a}^S$  and at this energy, the bound term is dominant with respect to the continuum term. As we tune-out from resonance, the blue solid line falls again to zero phase at the upper limit of the resonance. This means that the continuum term is again dominant, so the phase is dictated by the sign of it (Fig. (4.21)). For the green dashed line, the bound term continued being dominant in the energy range chosen (Fig. (4.22)). The energy range in which the phase of the sideband is  $\pi$  thus dictates the strength of the bound transitions.

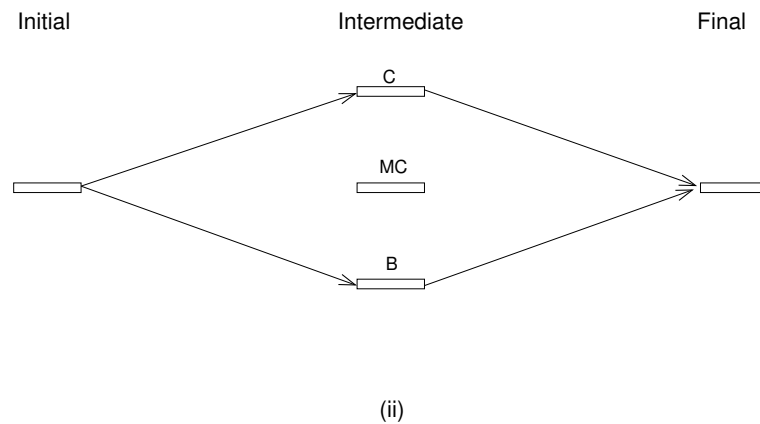


FIGURE 4.19: Sketch of the possible incoming/outgoing amplitudes for (ii). The bound and continuum component of the intermediate state can be populated, but they do not interact, leading to independent paths that interfere in the final state.

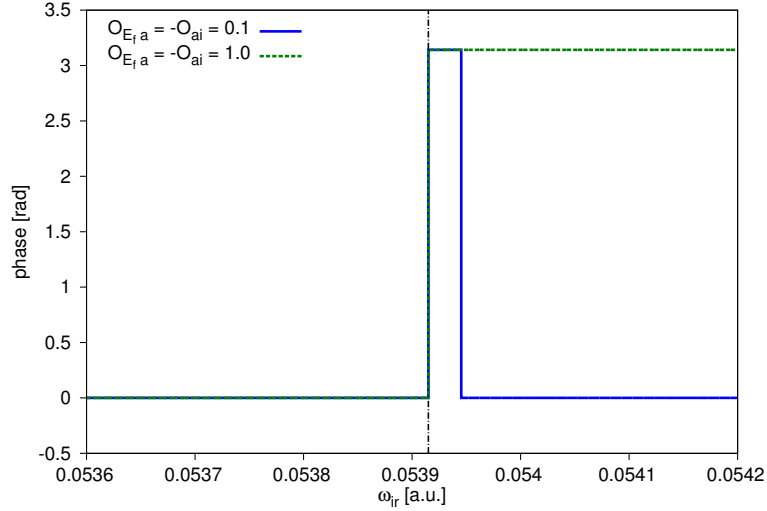


FIGURE 4.20: Phase of the sideband,  $\phi_{SB}^{at} = \arg[M_{2n+1}]$ , as a function of the laser frequency  $\omega_{IR}$  for the conditions in (ii). Two values for the transition matrix elements  $\mathcal{O}_{Efa}^S$  and  $\mathcal{O}_{ai}$  are shown. The dotted-dashed black line indicates the frequencies for which the upper harmonic is resonant with the doubly excited state  $sp_2^+$ . When  $\mathcal{O}_{Efa} = -\mathcal{O}_{ai} = 0.1$  a.u. (blue solid line), the phase changes abruptly by  $\pi$  at the frequency for which  $\omega_{2n+1} = E_a - IP$ , i.e., for which the term  $M^{BB}$  changes sign, and falls again to zero quickly when the  $M^{CC}$  term dominates again. When  $\mathcal{O}_{Efa}^S = -\mathcal{O}_{ai} = 1$  a.u. (green dashed line), there is a  $\pi$  shift at the same frequency as in the previous case, but the  $\pi$  phase of the sideband continues throughout the frequencies shown, indicating that the  $M^{BB}$  term is dominant.

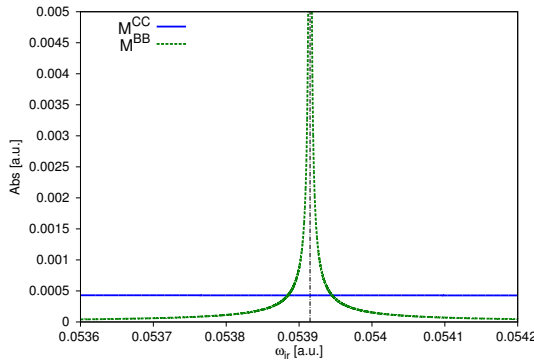


FIGURE 4.21: Absolute value of the two contributing terms as a function of the driving laser frequency for  $\mathcal{O}_{Efa} = -\mathcal{O}_{ai} = 0.1$  a.u. The dominant contribution far from resonance is the continuum-continuum term, while near resonance it is the bound-bound term.

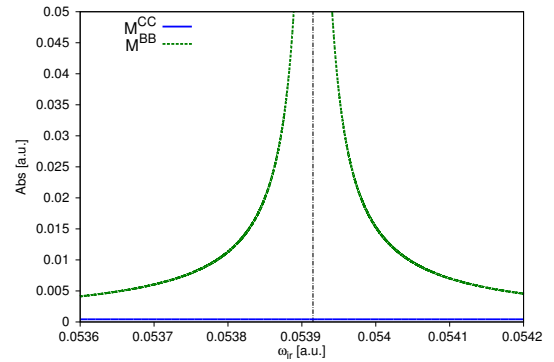


FIGURE 4.22:  $\mathcal{O}_{Efa} = -\mathcal{O}_{ai} = 1$  a.u. For such values of the matrix elements, the bound-bound term dominates over all frequencies shown.

(iii).  $\Gamma_a \neq 0$ ,  $\mathcal{O}_{ai} = 0$ ,  $\mathcal{O}_{Efa}^S \neq 0$ .

In this case, we have the coupling between the bound and continuum components (resonance width is not zero). The transition from the ground to the bound component of the intermediate state is forbidden, while the transition from the bound component to the final continuum is permitted. Hence, the resonance is dark-in/bright-out (see fig.(4.23)). The non-vanishing terms are

$$M_{2n+1} = M^{CC} + M^{MC} + M^{CM/MM} + M^{BC/BM}. \quad (4.5)$$

The contribution to the total matrix element of each term on the RHS of (4.5) is given in Figs.(4.25-4.27) as a function of the laser frequency for three representative values of  $\mathcal{O}_{Efa}$ . The resulting phase of the total matrix element  $M_{2n+1}$  as a function of the detuning is plotted in Fig.(4.24).

When the coupling between the bound and continuum is strong, the total transition matrix element is dominated by the  $M^{BC/BM}$  component (Fig. (4.27)). Thus, the phase should be that of Fig. (4.16). Indeed, this is what we observe in the red dotted line of Fig. (4.24), for a value of  $\mathcal{O}_{Efa} = 10$ a.u. For more moderate values of the bound-continuum coupling, the total transition matrix element is a mixture of the four different components in Eq. (4.5), and thus the phase will not follow any of the profiles given by Figs. (4.12-4.17). Such cases represent transitions in which the continuum contribution to the total transition matrix element competes with the bound contribution in similar amounts. In these cases, which are the norm rather than the exception in transitions involving autoionizing states, the phase will generally not show the characteristic  $\pi$  jump observed in transitions with null or negligible contribution of the continuum [32, 87].

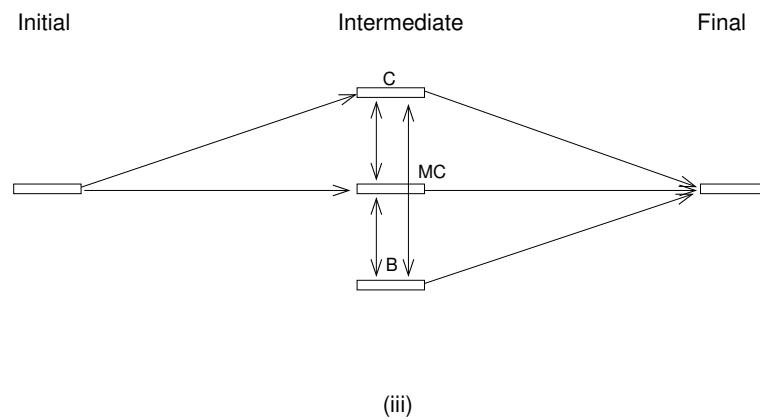


FIGURE 4.23: Sketch of the possible incoming/outgoing amplitudes for (iii). The continuum and modified continuum components of the intermediate state are populated from the ground state. Interaction between the three components in the intermediate state take place and the final state is populated from all the three intermediate components.

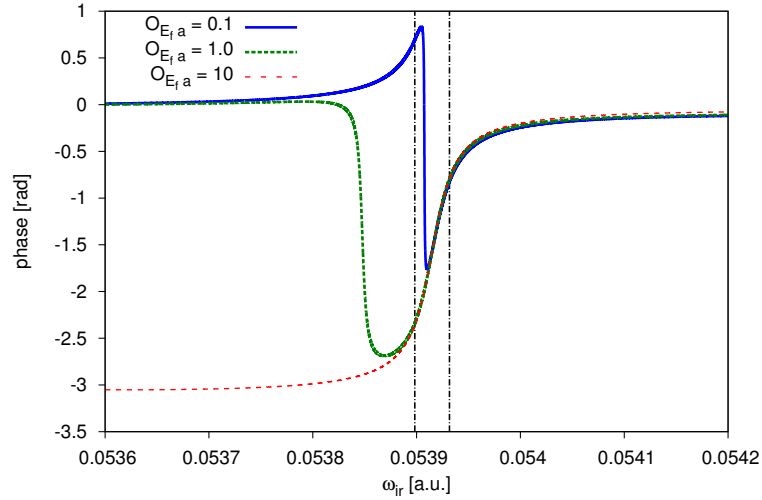


FIGURE 4.24: Phase of the sideband as a function of the laser frequency for the conditions in (iii). Three values of the transition matrix element  $\mathcal{O}_{E_f a}^S$  are shown: 0.1 a.u. (blue solid line), 1 a.u. (green dotted line) and 10 a.u. (red dashed line). The region in which the upper harmonic is resonant with the  $sp_2^+$  doubly excited state is delimited by the black dotted lines. When the coupling between the bound component and the continuum is strong enough, we obtain the  $-\pi$  to 0 jump associated to the  $M^{BC/BM}$  term. For weaker bound-continuum couplings, the result is a mixture of all contributing terms leading to radically different phase profiles.

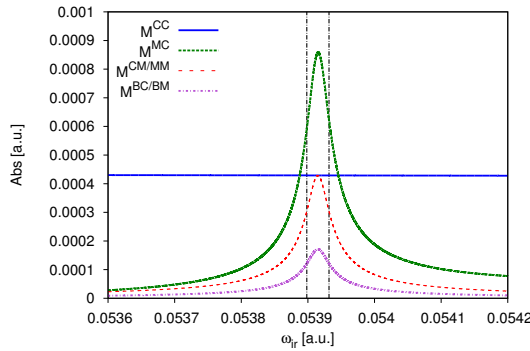


FIGURE 4.25:  $\mathcal{O}_{E_f a}^S = 0.1$  a.u. The dominant contribution far from resonance is the continuum-continuum term, while near resonance it is the  $M^{MC}$  term.

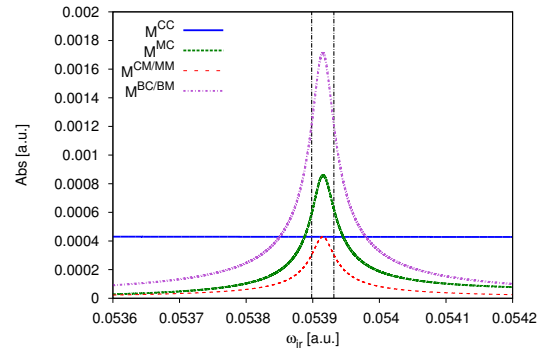


FIGURE 4.26:  $\mathcal{O}_{E_f a}^S = 1$  a.u. Far from resonance the continuum-continuum term dominates. As the laser frequency gets closer to the resonance, the term  $M^{BC/BM}$  dominates.

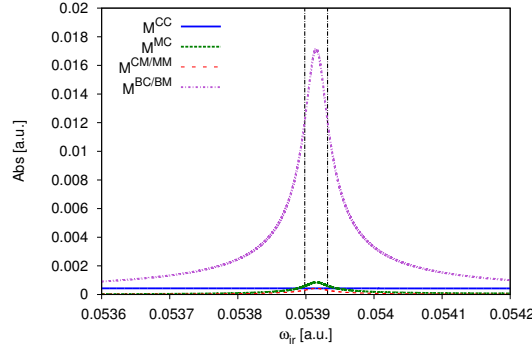


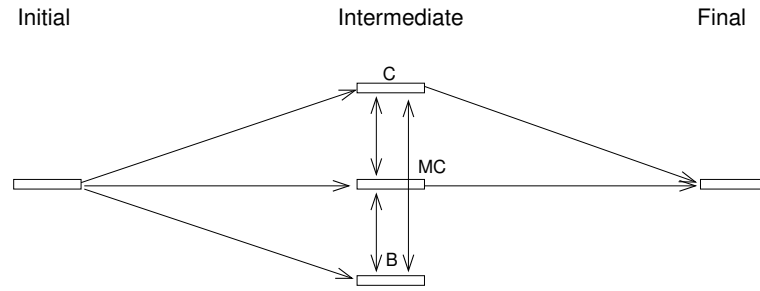
FIGURE 4.27:  $\mathcal{O}_{Efa}^S = 10$  a.u. In this case, the dominant term is  $M^{BC/BM}$  for all frequencies.

(iv).  $\Gamma_a \neq 0$ ,  $\mathcal{O}_{ai} \neq 0$ ,  $\mathcal{O}_{Efa}^S = 0$ .

The bound state is bright-in, i.e., the transition from the ground state to the bound state can occur, but it is dark-out, i.e., the transition amplitude between the bound and final state is zero. The terms that remain are

$$M_{2n+1} = M^{CC} + M^{MC} + M^{CM/MM} + M^{MB}. \quad (4.6)$$

In fig.(4.29) we show the variation of the phase as a function of the laser frequency for three values of  $\mathcal{O}_{ai}$ , while Figs.(4.30-4.32) show the contributions to the total matrix element of the different terms in Eq. (4.6). As in the previous case, when the coupling between the ground and bound part is strong, there is one dominant term,  $M^{CB/MB}$ . The phase variation is thus that of Fig. (4.15) and we see it coincides with the red dotted line in Fig. (4.29) where  $\mathcal{O}_{ai} = 10$ a.u. For weaker ground-bound couplings, where the continuum path contributes, the phase profile is again the result of the combination of all the terms in Eq. (4.6).



(iv)

FIGURE 4.28: Sketch of the possible incoming/outgoing amplitudes for (iv). The initial state populates the three components of the intermediate state. Later, they interact, and only the continuum and modified continuum components contribute to the outgoing amplitude.

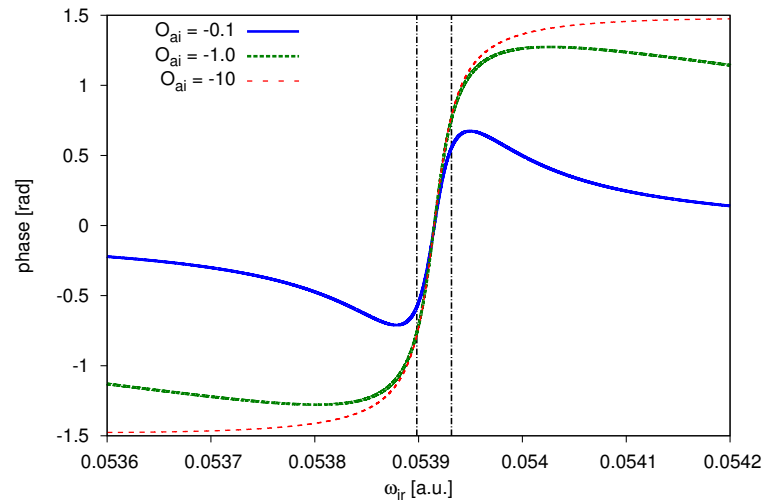


FIGURE 4.29: Phase of the sideband as a function of the laser frequency for the conditions in (iv). Three values of  $\mathcal{O}_{ai}$  are shown: -0.1 a.u. (blue solid line), -1 a.u. (green dotted line) and -10 a.u. (red dashed line). The dotted-dashed black lines indicate the frequencies for which the 41st Harmonics are resonant with the doubly excited state. A global  $\pi$  jump is observed only if the transition from the ground to the continuum is negligible.

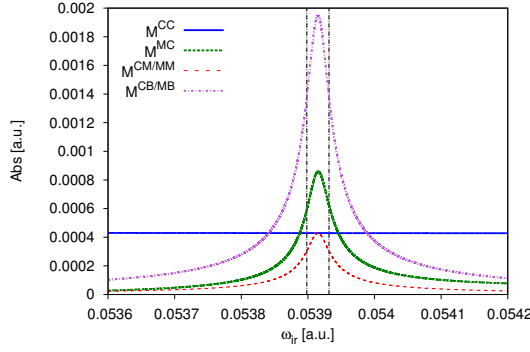


FIGURE 4.30:  $\mathcal{O}_{ai} = 0.1$  a.u. The dominant contribution far from resonance is the continuum-continuum term, while near resonance it is the  $M^{CB/MB}$  term. Still, the phase near the resonance will not be purely dictated by the  $M^{CB/MB}$  phase since the other terms are not negligible.

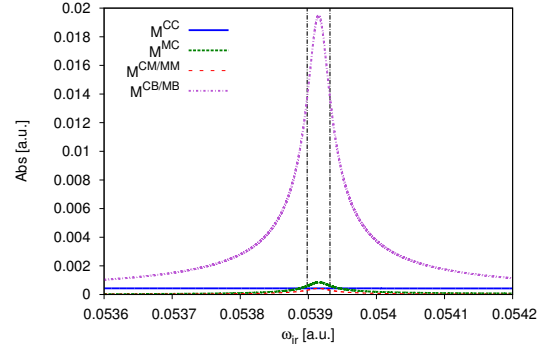


FIGURE 4.31:  $\mathcal{O}_{ai} = 1$  a.u. The  $M^{CB/MB}$  term dominates over all frequencies. Far from resonance the phase will not be dictated by this term alone since the  $M^{CC}$  contribution is not negligible.

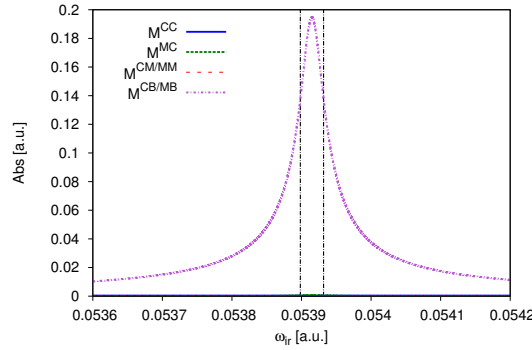


FIGURE 4.32:  $\mathcal{O}_{ai} = 10$  a.u.  $M^{CB/MB}$  is dominant over all frequencies and the other terms are negligible.

(v).  $\Gamma_a \neq 0$ ,  $\mathcal{O}_{ai} \neq 0$ ,  $\mathcal{O}_{Efa}^S \neq 0$ .

In the final case we consider, all possible transitions are active. As in the previous cases, we show the phase variation as a function of the laser frequency and the intensity of the different terms. When the transition matrix elements from and to the bound component,  $\mathcal{O}_{ai}$  and  $\mathcal{O}_{Efa}^S$ , are of the order of 0.1 a.u., the continuum phase dominates far from resonance, while near resonance it is other terms that count (mainly  $M^{CB/MB}$ ); the contribution of which are responsible for the shift of  $\sim 1.5$  rad in the blue solid line of Fig. (4.34). As we approach the limit of  $\mathcal{O}_{Efa}^S = \mathcal{O}_{ai} \sim \infty$ , i.e., a transition through a purely bound state, we recover the  $\pi$  jump observed in [32, 87]. In essence, different radiative couplings produce different outcomes in the final sideband phase. This makes

the latter a useful observable to quantify the otherwise very hard to obtain radiative transitions between autoionizing states.

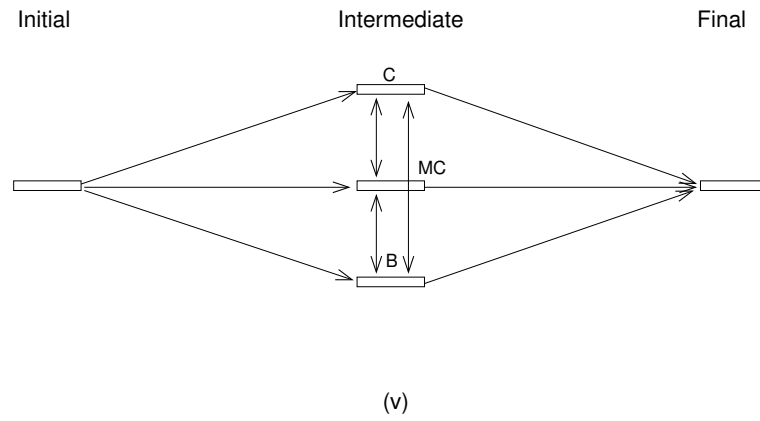


FIGURE 4.33: Sketch of the possible incoming/outgoing amplitudes for (v). All three components of the intermediate state are populated from the ground state, they interact, and they all populate the final state.

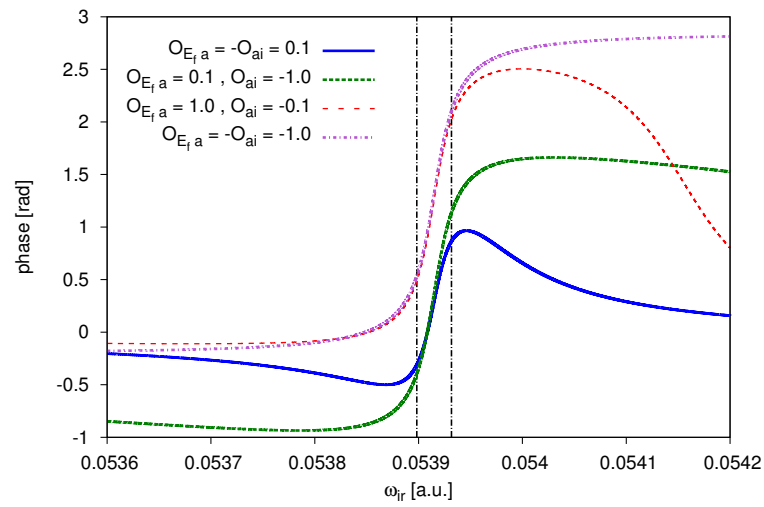
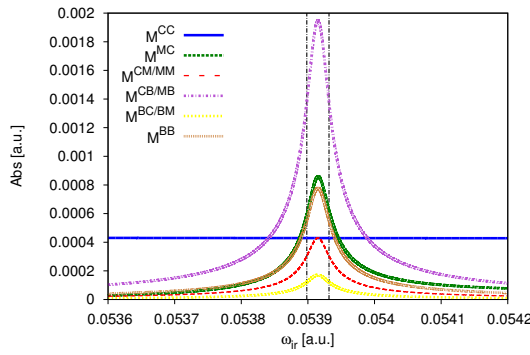
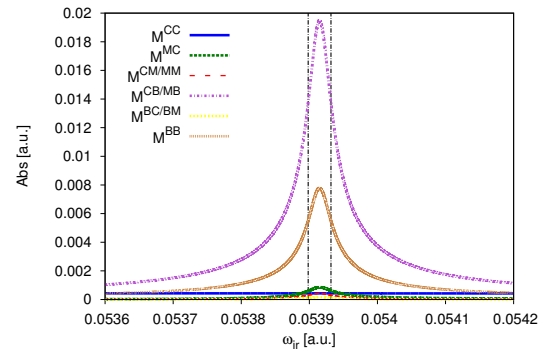
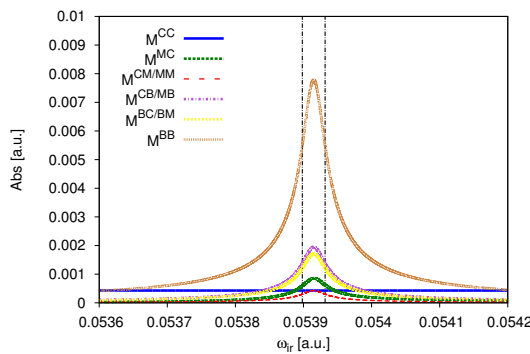
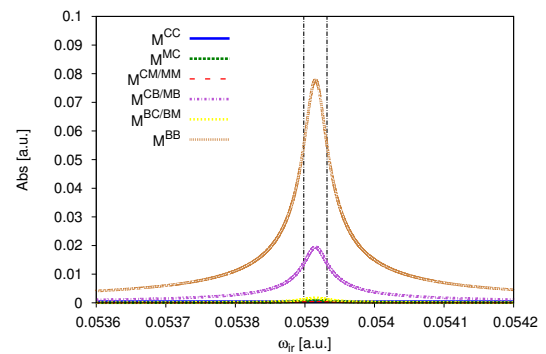


FIGURE 4.34: Phase of the sideband as a function of the laser frequency for the conditions in (v). For a value of  $O_{E_f a}^S = -O_{a i} = 0.1$ , the phase is modified slightly near the resonance. As the values of  $O_{a i}$  and  $O_{E_f a}^S$  increase, the phase suffers a bigger variation converging to the  $\pi$  jump observed for transitions through purely bound states.

FIGURE 4.35:  $\mathcal{O}_{Efa}^S = -\mathcal{O}_{ai} = 0.1$  a.u.FIGURE 4.36:  $\mathcal{O}_{Efa} = 0.1$  a.u.,  $\mathcal{O}_{ai} = -1$  a.u.FIGURE 4.37:  $\mathcal{O}_{Efa} = 1$  a.u.,  $\mathcal{O}_{ai} = -0.1$  a.u.FIGURE 4.38:  $\mathcal{O}_{Efa} = -\mathcal{O}_{ai} = 1$  a.u.

#### 4.2.4.3 Separated pulses.

The purely localized components of the autoionizing states manifest not only in the phases of the photoelectron sidebands, but also in their intensity. Let us consider the case of two separated, non-overlapping pump and probe pulses. In this case, the contribution of the non-localized component of the excited intermediate state rapidly vanishes and the bound component alone survives. In spectral terms, during the time gap between pump and probe, the continuum component acquires a phase  $e^{-i\omega t_d}$  which varies rapidly with energy and thus effectively kills all coherent contributions to subsequent transitions except those from features in the spectrum that are sharp if compared to  $1/t_d$ . Hence, from the intensity of the sideband that originates when both pulses are separated, one can have an estimate of the transition elements  $\mathcal{O}_{Efa}^\ell$ .

Furthermore, when both intermediate states are resonant, the sidebands will oscillate due uniquely to the interference between the bound components of the intermediate states. In Fig.(4.39) we illustrate the oscillations of the sidebands in a R-C-R and in a

R-R-R transition (with different doubly excited states) when both pulses are separated sufficiently so that they do not overlap.

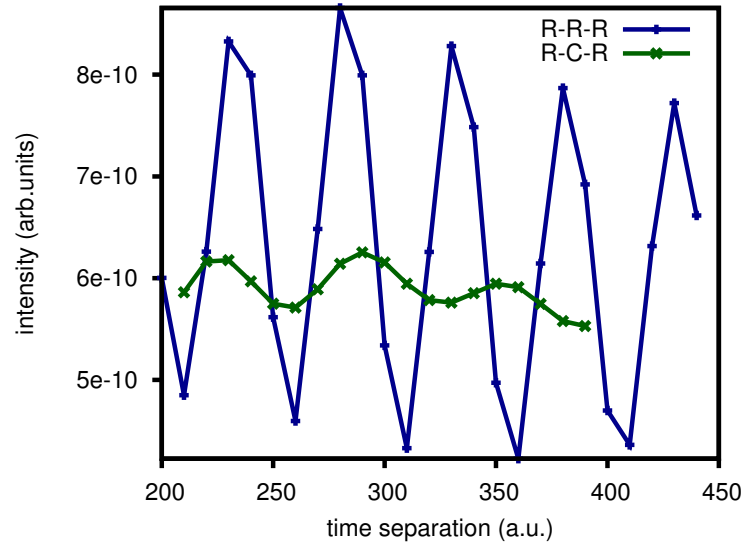


FIGURE 4.39: Sideband oscillations when both pulses are separated (only bound-component part contributes to the oscillations). In the x-axis we indicate the separation of the pulses (from tail to tail) in atomic units. The blue and green lines correspond to a R-R-R and R-C-R transition, respectively. In the case of the R-C-R transition, the upper harmonic is resonant with the  $sp_3^-$  ( $\Gamma = 3.8 \cdot 10^{-6}$  a.u.) while in the R-R-R transition the upper harmonic is resonant with  $sp_3^+$  ( $\Gamma = 3 \cdot 10^{-4}$  a.u.). The lower harmonic for both cases was resonant with the  $sp_2^+$  DES, and the central DES for the R-R-R transition was  $2p^2$ .

## Chapter 5

# Conclusions and perspectives

The work produced in this master thesis detailed the radiative transitions that occur in the continuum by means of novel attosecond pump-probe techniques. Its results are devoted to be used as a theoretical framework for future attosecond experiments. In particular, we contributed to the attosecond science field by extending the soft photon approximation to be used with novel experiments and by developing a model that will permit us to study electronic correlation with the experimental techniques available today.

In the extension of the soft photon approximation, we applied the results to two typical pump-probe schemes, streaking and RABITT, in the single ionization threshold of helium. The results showed that all single particle effects can be well accounted for within this approximation either in the strong field or perturbative regimes for both pump-probe schemes. Moreover, we predicted effects due to the finiteness of the IR pulse and its intensity. In reference to the latter, we developed a model that could possibly lead to the extension of the RABITT technique beyond the perturbative limit in which it is established. This work was presented at the EGAS (European Group of Atomic Systems) 2012 congress and at the International Workshop on Atomic Physics in 2012. It has also led to the production of a paper that has been submitted [90].

Regarding the two-photon perturbative model, we determined a relation between the observed phase shifts in the RABITT technique and a set of parameters that measure the electronic correlation of the system. In particular, we showed how the phase that can be extracted with such technique varies dramatically with the introduction of transitions from and to the bound component of a doubly excited state. Such transitions are prohibited in the single particle picture, and appear due to correlation. This observation opens a new way to study many-body effects in radiative continuum-continuum transitions. This work was presented at the ATTO 2013 conference and will be the subject of two future publications.

The line of research initiated during this work of master thesis can be developed along manifold directions. First, the analysis of the resonant model can be extended to the case of several resonant states, a circumstance that, as we showed in Sec.4.2.2, occurs frequently. The model can be also extended to the case of non-monochromatic pulses to make a comparison with the outcome of ab-initio simulations. So far, we considered the effect of electronic correlation on the photoejection time delay only in the case of one open channel. A natural continuation of this study is to consider the case of several open channels, where the time delay is expressed in terms of a matrix and the simple correspondence with the energy derivative of the phase-shift is consequently lost. In a similar way, it is interesting to consider whether the autoionization branching ratio of autoionizing states embedded in a multichannel continuum can be controlled.

A line of investigation complementary to the one considered so far, where the only observable is the distribution of the photofragments at the end of the ionization event, is to monitor the change in the state of the light transmitted through the sample. Two major experimental techniques based on this idea have acquired considerable importance in attosecond time-resolved studies: high harmonic generation (HHG) and attosecond transient absorption spectroscopy (ATAS) [21, 91]. HHG has been used in the past to record so-called molecular movies. It would be conceivable to extend the recollision process on which it is based to the case of excited parent ions. Indeed, resonant HHG is an active field of research where reliable theoretical support is still largely missing. ATAS, on the other hand, manifests itself already in perturbative conditions. In contrast to HHG, this technique is based on the assumption that only pre-existing XUV light can be altered by means of stimulated emission/absorption induced by the interaction with a dressing field. It has been recently shown that ATAS can provide information on electronic coherence in neutral transiently bound states. The technique, however, would apply equally well in the case of a train of attosecond pulses as only coherences between states separated by twice the frequency of the dressing field are detected. Yet, ab-initio predictions of ATAS of multiply-excited states recorded with APT have not been considered so far.

## Appendix A

# Monochromatic two photon perturbative model

### A.1 Scalar product of plane and spherical waves

Based on the expansion of a plane wave in spherical waves,

$$\exp(i \vec{k} \cdot \vec{r}) = 4\pi \sum_{\ell=0}^{\infty} \sum_{m=-\ell}^{\ell} i^{\ell} Y_{\ell m}^*(\hat{k}) Y_{\ell m}(\hat{r}) j_{\ell}(kr), \quad (\text{A.1})$$

the scalar product of a plane wave and a spherical wave can be derived,

$$\begin{aligned} \langle \vec{k} | k' \ell m \rangle &= \sqrt{\frac{2}{\pi}} \sum_{\ell=0}^{\infty} \sum_{\mu=-\ell}^{\ell} -i^{\ell} \int d^3r Y_{\ell \mu}(\hat{k}) Y_{\ell \mu}^*(\hat{r}) j_{\ell}(kr) \sqrt{\frac{2k^2}{\pi}} Y_{\ell m}(\hat{r}) j_{\ell}(k'r) = \\ &= \frac{2k}{\pi} \sum_{\ell \mu} -i^{\ell} Y_{\ell \mu}(\hat{k}) \langle Y_{\ell \mu} | Y_{\ell m} \rangle \int dr r^2 j_{\ell}(kr) j_{\ell}(k'r) = \\ &= -\frac{i^{\ell}}{k'} Y_{\ell m}(\hat{k}) \delta(k - k'), \end{aligned} \quad (\text{A.2})$$

where we made use of the orthogonality relation between spherical Bessel functions

$$\int dr r^2 j_{\ell}(kr) j_{\ell}(k'r) = \pi/2 \frac{1}{k k'} \delta(k - k'). \quad (\text{A.3})$$

## A.2 Explicit derivation

### A.2.1 CC matrix element

$$\mathcal{M}_\omega^{CC} = \alpha^2 \int dE' \langle E_f \ell m | p_z | E' 10 \rangle \langle E' 10 | p_z | \phi_0 \rangle \frac{1}{\omega_i + \omega_{2n\pm 1} - E' + i0^+} \quad (\text{A.4})$$

The first dipole transition matrix element is given by

$$\begin{aligned} \langle E' 10 | p_z | \phi_0 \rangle &= \int d^3 k \langle E' 10 | \vec{k} \rangle \langle \vec{k} | p_z | \phi_0 \rangle \\ &= \int d^3 k \frac{1}{\sqrt{k}} \langle k'_m 10 | \vec{k} \rangle k \cos \theta \langle \vec{k} | \phi_0 \rangle \\ &= i \sqrt{\frac{4\pi}{3}} \int d\Omega Y_{10} Y_{10}^* \int dk k^{3/2} \phi_0(k) \delta(k'_m - k) \\ &= i \sqrt{\frac{4\pi}{3}} (2E')^{3/4} \phi_0(\sqrt{2E'}). \end{aligned} \quad (\text{A.5})$$

The second is

$$\begin{aligned} \langle E_f \ell m | p_z | E' 10 \rangle &= \int d^3 k \langle E_f \ell m | \vec{k} \rangle \langle \vec{k} | p_z | E' 10 \rangle \\ &= \int d^3 k \frac{1}{k} \langle k_f \ell m | \vec{k} \rangle k \cos \theta \langle \vec{k} | k' 10 \rangle \\ &= (-i) i^\ell \sqrt{\frac{4\pi}{3}} \int d\Omega Y_{10} Y_{10}^* Y_{\ell m} \int dk \delta(k_f - k) \delta(k' - k) \\ &= (-i) i^\ell \sqrt{\frac{4\pi}{3}} \int d\Omega \left( \frac{1}{\sqrt{4\pi}} Y_{00} + \frac{1}{\sqrt{5\pi}} Y_{20} \right) Y_{\ell m} \int dk \delta(k_f - k) \delta(k'_m - k). \end{aligned} \quad (\text{A.6})$$

We thus can separate the final state into an S or a D wave. The matrix elements for the two symmetries read,

$$\langle E_f 00 | p_z | E' 10 \rangle = -\frac{i}{\sqrt{3}} \delta(k' - k_f) = -\frac{i}{\sqrt{3}} \sqrt{2E_f} \delta(E' - E_f), \quad (\text{A.7})$$

$$\langle E_f 20 | p_z | E' 10 \rangle = i \sqrt{\frac{4}{15}} \delta(k' - k_f) = i \sqrt{\frac{4}{15}} \sqrt{2E_f} \delta(E' - E_f), \quad (\text{A.8})$$

where we made use of the relation  $\cos \theta = \sqrt{\frac{4\pi}{3}} Y_{10}$  and  $Y_{10}^2 = \frac{1}{\sqrt{4\pi}} Y_{00} + \frac{1}{\sqrt{5\pi}} Y_{20}$  and of Eq. (A.2). The CC contribution with a final S symmetry is thus

$$\begin{aligned} \mathcal{M}_{E_f 00 \leftarrow 1S}^{CC} &= \alpha^2 \int dE' \frac{\left( i\sqrt{\frac{4\pi}{3}} (2E')^{3/4} \phi_0(\sqrt{2E'}) \right) \left( -\frac{i}{\sqrt{3}} \sqrt{2E_f} \delta(E_f - E') \right)}{\omega_i + \omega_{2n\pm 1} - E' + i0^+} = \\ &= \alpha^2 \frac{\sqrt{4\pi}}{3} (2E_f)^{5/4} \phi_0(\sqrt{2E_f}) \frac{1}{\omega_i + \omega_{2n\pm 1} - E_f + i0^+} = \\ &= \pm \alpha^2 \frac{\sqrt{4\pi}}{3} (2E_f)^{5/4} \phi_0(\sqrt{2E_f}) \omega_{ir}^{-1}. \end{aligned} \quad (\text{A.9})$$

The corresponding matrix element for a final D symmetry differs from the previous one by a factor of  $(-\frac{2}{\sqrt{5}})$ ,

$$\mathcal{M}_{E_f 20 \leftarrow 1S}^{CC} = -\alpha^2 \frac{\sqrt{4\pi}}{3} \frac{2}{\sqrt{5}} (2E_f)^{5/4} \phi_0(\sqrt{2E_f}) \frac{1}{\omega_i + \omega_{2n\pm 1} - E_f + i0^+}. \quad (\text{A.10})$$

We must notice that the final eigenstate is a free electron eigenstate and, thus, the final energy  $E_f$  corresponds to the photoelectron energy.

### A.2.2 CM matrix element

$$\begin{aligned} \mathcal{M}_{\omega}^{CM} &= \alpha^2 \int dE' \int d\epsilon' \langle E_f 00 | p_z | E' 10 \rangle \langle \epsilon' 10 | p_z | \phi_0 \rangle \times \\ &\frac{V_{\epsilon'a}}{E' - \epsilon' - i0^+} \frac{V_{aE'}}{E' - E_a - i\Gamma_a/2} \frac{1}{\omega_i + \omega_{2n\pm 1} - E' + i0^+} = \\ &= \alpha^2 \int dE' \int d\epsilon' \left( -\frac{i}{\sqrt{3}} \sqrt{2E_f} \delta(E_f - E') \right) \left( i\sqrt{\frac{4\pi}{3}} (2\epsilon')^{3/4} \phi_0(\epsilon') \right) \times \\ &\frac{V_{\epsilon'a}}{E' - \epsilon' - i0^+} \frac{V_{aE'}}{E' - E_a - i\Gamma_a/2} \frac{1}{\omega_i + \omega_{2n\pm 1} - E' + i0^+} = \\ &= \alpha^2 \frac{\sqrt{4\pi}}{3} \sqrt{2E_f} \int dE' \delta(E_f - E') \frac{V_{aE'}}{E' - E_a - i\Gamma_a/2} \frac{1}{\omega_i + \omega_{2n\pm 1} - E' + i0^+} \times \\ &\int d\epsilon' (2\epsilon')^{3/4} \phi_0(\epsilon') \frac{V_{\epsilon'a}}{E' - \epsilon' - i0^+}. \end{aligned} \quad (\text{A.11})$$

In the last distribution, the function of the energy  $V_{\epsilon'a}$  can be taken constant and equal to  $\sqrt{\frac{\Gamma_a}{2\pi}}$  in the domain of interest. Moreover, we can express the distribution as a principal part plus a delta contribution in the form:

$$\int \frac{f(x)}{a - x - i0^+} dx = \text{P.P.} \underbrace{\int \frac{f(x)}{a - x} dx}_{\Delta_{PP}(a)} + i\pi f(a). \quad (\text{A.12})$$

In this way, we write

$$\begin{aligned}
\mathcal{M}_\omega^{CM} &= \alpha^2 \frac{\sqrt{4\pi}}{3} \sqrt{2E_f} \int dE' \delta(E_f - E') \frac{V_{aE'}}{E' - E_a - i\Gamma_a/2} \frac{1}{\omega_i + \omega_{2n\pm 1} - E' + i0^+} \times \\
&\quad \left( \Delta_{PP}(E') + i\pi(2E')^{3/4} \phi_0(\sqrt{2E'}) V_{E'a} \right) = \\
&= \alpha^2 \frac{\sqrt{4\pi}}{3} \frac{1}{E_f - E_a - i\Gamma_a/2} \frac{\sqrt{2E_f}}{\omega_i + \omega_{2n\pm 1} - E_f + i0^+} \frac{\Gamma_a}{2\pi} \left( \Delta_{PP}(E_f) + i\pi(2E_f)^{3/4} \phi_0(\sqrt{2E_f}) \right) = \\
&= \pm i \frac{\sqrt{\pi}}{3} \alpha^2 \Gamma_a \omega_{ir}^{-1} \frac{(2E_f)^{5/4} \phi_0(\sqrt{2E_f})}{E_f - E_a - i\Gamma_a/2}.
\end{aligned} \tag{A.13}$$

Where we assumed that the function  $f(E) = (2E)^{3/4} \phi_0(\sqrt{2E}) V_{Ea}$  varies smoothly with  $E$  across an interval of  $\Delta E = 2\omega_{ir}$ , and hence  $\Delta_{PP}(E_f) \approx 0$ .

### A.2.3 CB matrix element

$$\begin{aligned}
\mathcal{M}_\omega^{CB} &= \alpha^2 \int dE' \langle E_f 00 | p_z | E' 10 \rangle \langle a | p_z | \phi_0 \rangle \frac{V_{aE'}}{E' - E_a - i\Gamma_a/2} \frac{1}{\omega_i + \omega_{2n\pm 1} - E' + i0^+} = \\
&= \alpha^2 \int dE' \left( -\frac{i}{\sqrt{3}} \sqrt{2E_f} \delta(E_f - E') \right) \mathcal{O}_{ai} \frac{V_{aE'}}{E' - E_a - i\Gamma_a/2} \frac{1}{\omega_i + \omega_{2n\pm 1} - E' + i0^+} = \\
&= -\alpha^2 \frac{i}{\sqrt{3}} \sqrt{2E_f} \mathcal{O}_{ai} \sqrt{\frac{\Gamma_a}{2\pi}} \frac{1}{E_f - E_a - i\Gamma_a/2} \frac{1}{\omega_i + \omega_{2n\pm 1} - E_f + i0^+} = \\
&= \mp i \alpha^2 \sqrt{\frac{2E_f}{3}} \omega_{ir}^{-1} \sqrt{\frac{\Gamma_a}{2\pi}} \frac{\mathcal{O}_{ai}}{E_f - E_a - i\Gamma_a/2},
\end{aligned} \tag{A.14}$$

where we have introduced the parameter  $\langle a | p_z | \phi_0 \rangle \equiv \mathcal{O}_{ai}$ .

### A.2.4 MC matrix element

$$\begin{aligned}
\mathcal{M}_\omega^{MC} &= \alpha^2 \int dE' \int d\epsilon' \langle E_f 00 | p_z | \epsilon' 10 \rangle \langle E' 10 | p_z | \phi_0 \rangle \times \\
&\quad \frac{V_{\epsilon'a}}{E' - \epsilon' + i0^+} \frac{V_{aE'}}{E' - E_a + i\Gamma_a/2} \frac{1}{\omega_i + \omega_{2n\pm 1} - E' + i0^+} = \\
&= \alpha^2 \int dE' \int d\epsilon' \left( -\frac{i}{\sqrt{3}} \sqrt{2E_f} \delta(E_f - \epsilon') \right) \left( i \sqrt{\frac{4\pi}{3}} (2E')^{3/4} \phi_0(\sqrt{2E'}) \right) \times \\
&\quad \frac{V_{\epsilon'a}}{E' - \epsilon' + i0^+} \frac{V_{aE'}}{E' - E_a + i\Gamma_a/2} \frac{1}{\omega_i + \omega_{2n\pm 1} - E' + i0^+} = \\
&= \alpha^2 \frac{\sqrt{4\pi}}{3} \sqrt{2E_f} \int dE' (2E')^{3/4} \phi_0(\sqrt{2E'}) \times \\
&\quad \frac{V_{Efa}}{E' - E_f + i0^+} \frac{V_{aE'}}{E' - E_a + i\Gamma_a/2} \frac{1}{\omega_i + \omega_{2n\pm 1} - E' + i0^+}.
\end{aligned} \tag{A.15}$$

Now we need to calculate the product of three distributions,

$$\begin{aligned}
& \frac{V_{E_f a}}{E' - E_f + i0^+} \frac{V_{a E'}}{E' - E_a + i\Gamma_a/2} \frac{1}{\omega_i + \omega_{2n\pm 1} - E' + i0^+} = \\
& - \frac{\Gamma_a}{2\pi} \frac{1}{E_f - E_a + i\Gamma_a/2} \left[ \frac{1}{E_f - E' - i0^+} + \frac{1}{E' - E_a + i\Gamma_a/2} \right] \frac{1}{\omega_i + \omega_{2n\pm 1} - E' + i0^+} = \\
& - \frac{\Gamma_a}{2\pi} \frac{1}{E_f - E_a + i\Gamma_a/2} \left[ - \frac{1}{\omega_i + \omega_{2n\pm 1} - E_f + i0^+} \left( \frac{1}{E' - E_f + i0^+} + \frac{1}{\omega_i - E' + i0^+} \right) + \right. \\
& \left. + \frac{1}{\omega_i + \omega_{2n\pm 1} - E_a + i\Gamma_a/2} \left( \frac{1}{E' - E_a + i\Gamma_a/2} + \frac{1}{\omega_i + \omega_{2n\pm 1} - E' + i0^+} \right) \right].
\end{aligned} \tag{A.16}$$

We now assume that

$$\text{P.P.} \int \frac{f(x)}{a-x} - \text{P.P.} \int \frac{f(x)}{b-x} \approx 0 \quad \text{for } |a-b| \approx \omega_{ir}. \tag{A.17}$$

This approximation is only valid when  $f(x)$  does not oscillate or change abruptly in the energy region considered, which is a valid approximation for the function  $f(x) = (2x)^{3/4} \phi_0(\sqrt{2x})$ . In this case, we have

$$\begin{aligned}
& \frac{1}{E' - E_f + i0^+} + \frac{1}{\omega_i + \omega_{2n\pm 1} - E' + i0^+} \approx -2i\pi\delta(E' - E_f) \\
& \frac{1}{E' - E_a + i\Gamma_a/2} + \frac{1}{\omega_i + \omega_{2n\pm 1} - E' + i0^+} \approx -2i\pi\delta(E' - E_a).
\end{aligned} \tag{A.18}$$

We are left with

$$\frac{i\Gamma_a\delta(E' - E_f)}{E_f - E_a + i\Gamma_a/2} \left[ \frac{1}{\omega_i + \omega_{2n\pm 1} - E_a + i\Gamma_a/2} - \frac{1}{\omega_i + \omega_{2n\pm 1} - E_f + i0^+} \right]. \tag{A.19}$$

If we introduce this result in the transition matrix element, we obtain

$$\begin{aligned}
\mathcal{M}_{E00 \leftarrow 1S}^{MC} &= \alpha^2 \frac{\sqrt{4\pi}}{3} (2E_f)^{5/4} \phi_0(\sqrt{2E_f}) \times \\
& \frac{i\Gamma_a}{E_f - E_a + i\Gamma_a/2} \left[ \frac{1}{\omega_i + \omega_{2n\pm 1} - E_a + i\Gamma_a/2} - \frac{1}{\omega_i + \omega_{2n\pm 1} - E_f + i0^+} \right] = \\
& = i\alpha^2 \Gamma_a \frac{\sqrt{4\pi}}{3} (2E_f)^{5/4} \phi_0(\sqrt{2E_f}) \left[ \frac{1}{\omega_i + \omega_{2n\pm 1} - E_a + i\Gamma_a/2} \mp \omega_{ir}^{-1} \right].
\end{aligned} \tag{A.20}$$

## A.2.5 MM matrix element

$$\begin{aligned}
\mathcal{M}_\omega^{MM} &= \alpha^2 \int dE' \int d\epsilon' \int d\epsilon'' \langle E_f 00 | p_z | \epsilon' 10 \rangle \langle \epsilon'' 10 | p_z | \phi_0 \rangle \times \\
&\quad \frac{V_{\epsilon' a}}{E' - \epsilon' + i0^+} \frac{V_{a E'}}{E' - E_a - i\Gamma_a/2} \frac{V_{\epsilon'' a}}{E' - \epsilon'' - i0^+} \times \\
&\quad \frac{V_{a E'}}{E' - E_a + i\Gamma_a/2} \frac{1}{\omega_i + \omega_{2n\pm 1} - E' + i0^+} = \\
&= \alpha^2 \int dE' \int d\epsilon' \int d\epsilon'' \left( -\frac{i}{\sqrt{3}} \sqrt{2\epsilon'} \delta(E_f - \epsilon') \right) \left( i \sqrt{\frac{4\pi}{3}} (2\epsilon'')^{3/4} \phi_0(\epsilon'') \right) \times \\
&\quad \frac{V_{\epsilon' a}}{E' - \epsilon' + i0^+} \frac{V_{a E'}}{E' - E_a - i\Gamma_a/2} \frac{V_{\epsilon'' a}}{E' - \epsilon'' - i0^+} \times \\
&\quad \frac{V_{a E'}}{E' - E_a + i\Gamma_a/2} \frac{1}{\omega_i + \omega_{2n\pm 1} - E' + i0^+} = \\
&= \alpha^2 \frac{\sqrt{4\pi}}{3} \sqrt{2E_f} \left( \frac{\Gamma_a}{2\pi} \right)^2 \int dE' \int d\epsilon'' (2\epsilon'')^{3/4} \phi_0(\epsilon'') \times \\
&\quad \frac{1}{E' - E_f + i0^+} \frac{1}{E' - E_a - i\Gamma_a/2} \frac{1}{E' - \epsilon'' - i0^+} \times \\
&\quad \frac{1}{E' - E_a + i\Gamma_a/2} \frac{1}{\omega_i + \omega_{2n\pm 1} - E' + i0^+}.
\end{aligned} \tag{A.21}$$

The distribution in  $\epsilon''$  can again be casted in the form of a principal part and a delta function,

$$\begin{aligned}
\mathcal{M}_\omega^{MM} &= \alpha^2 \frac{\sqrt{4\pi}}{3} \sqrt{2E_f} \left( \frac{\Gamma_a}{2\pi} \right)^2 \int dE' \left( \Delta_{PP}(E') + i\pi (2E')^{3/4} \phi_0(\sqrt{2E'}) \right) \times \\
&\quad \frac{1}{E' - E_f + i0^+} \frac{1}{E' - E_a - i\Gamma_a/2} \frac{1}{E' - E_a + i\Gamma_a/2} \frac{1}{\omega_i + \omega_{2n\pm 1} - E' + i0^+}.
\end{aligned} \tag{A.22}$$

The product of the four distributions are calculated in the following way

$$\begin{aligned}
&\frac{1}{\omega - E' + i0^+} \frac{1}{E' - E_f + i0^+} \frac{1}{E' - E_a + i\Gamma_a/2} \frac{1}{E' - E_a - i\Gamma_a/2} = \\
&= -\frac{1}{\omega - E_f + i0^+} \left[ \frac{1}{\omega - E' + i0^+} + \frac{1}{E' - E_f + i0^+} \right] \frac{i}{\Gamma_a} \times \\
&\quad \left[ \frac{1}{E_a - E' - i\Gamma_a/2} + \frac{1}{E' - E_a - i\Gamma_a/2} \right] = \\
&\frac{1}{i\Gamma_a} \frac{1}{\omega - E_f + i0^+} \left[ \frac{2i\pi\delta(E' - E_a)}{\omega - E_a + i\Gamma/2} - \frac{2i\pi\delta(E' - E_a)}{E_f - E_a - i\Gamma_a/2} \right] = \\
&\frac{2\pi}{\Gamma_a} \frac{\delta(E' - E_f)}{\omega - E_f + i0^+} \left[ \frac{1}{\omega - E_a + i\Gamma_a/2} - \frac{1}{E_f - E_a - i\Gamma_a/2} \right],
\end{aligned} \tag{A.23}$$

where we have again taken advantage of the property in Eq.(A.17) for the functions  $f(x) = (2x)^{3/4}\phi_0(\sqrt{2x})$  and  $f(x) = \Delta_{PP}(x)$ . Thus the transition matrix element reads

$$\begin{aligned}
\mathcal{M}_{E00\leftarrow 1S}^{MM} &= \alpha^2 \frac{\sqrt{4\pi}}{3} \frac{\Gamma_a}{2\pi} \frac{\sqrt{2E_f}}{\omega - E_f + i0^+} \left( \Delta_{PP}(E_f) + i\pi(2E_f)^{3/4}\phi_0(\sqrt{2E_f}) \right) \times \\
&\quad \left[ \frac{1}{\omega - E_a + i\Gamma_a/2} - \frac{1}{E_f - E_a - i\Gamma_a/2} \right] = \\
&= \pm i\alpha^2 \frac{\sqrt{\pi}}{3} \Gamma_a \omega_{ir}^{-1} (2E_f)^{5/4} \phi_0(\sqrt{2E_f}) \times \\
&\quad \left[ \frac{1}{\omega_i + \omega_{2n\pm 1} - E_a + i\Gamma_a/2} - \frac{1}{E_f - E_a - i\Gamma_a/2} \right].
\end{aligned} \tag{A.24}$$

### A.2.6 MB matrix element

$$\begin{aligned}
\mathcal{M}_\omega^{MB} &= \alpha^2 \int dE' \int d\epsilon' \langle E_f 00 | p_z | \epsilon' 10 \rangle \langle a | p_z | \phi_0 \rangle \times \\
&\quad \frac{V_{\epsilon'a}}{E' - \epsilon' + i0^+} \frac{V_{aE'}}{E' - E_a - i\Gamma_a/2} \frac{V_{aE'}}{E' - E_a + i\Gamma_a/2} \frac{1}{\omega_i + \omega_{2n\pm 1} - E' + i0^+} = \\
&= \alpha^2 \int dE' \int d\epsilon' \left( -\frac{i}{\sqrt{3}} \sqrt{2\epsilon'} \delta(E_f - \epsilon') \right) \mathcal{O}_{ai} \times \\
&\quad \frac{V_{\epsilon'a}}{E' - \epsilon' + i0^+} \frac{V_{aE'}}{E' - E_a - i\Gamma_a/2} \frac{V_{aE'}}{E' - E_a + i\Gamma_a/2} \frac{1}{\omega_i + \omega_{2n\pm 1} - E' + i0^+} = \\
&= -i \frac{\alpha^2}{\sqrt{3}} \sqrt{2E_f} \mathcal{O}_{ai} \left( \frac{\Gamma_a}{2\pi} \right)^{3/2} \int dE' \frac{1}{E' - E_f + i0^+} \times \\
&\quad \frac{1}{E' - E_a - i\Gamma_a/2} \frac{1}{E' - E_a + i\Gamma_a/2} \frac{1}{\omega_i + \omega_{2n\pm 1} - E' + i0^+}.
\end{aligned} \tag{A.25}$$

The product of distributions is identical to the  $MM$  term. The result of the transition matrix element is then

$$\begin{aligned}
\mathcal{M}_{E00\leftarrow 1S}^{MB} &= -i \frac{\alpha^2}{\sqrt{3}} \sqrt{2E_f} \mathcal{O}_{ai} \left( \frac{\Gamma_a}{2\pi} \right)^{1/2} \times \\
&\quad \frac{1}{\omega - E_f + i0^+} \left[ \frac{1}{\omega - E_a + i\Gamma_a/2} - \frac{1}{E_f - E_a - i\Gamma_a/2} \right] = \\
&= \mp i\alpha^2 \sqrt{\frac{2E_f}{3}} \mathcal{O}_{ai} \sqrt{\frac{\Gamma_a}{2\pi}} \omega_{ir}^{-1} \left[ \frac{1}{\omega_i + \omega_{2n\pm 1} - E_a + i\Gamma_a/2} - \frac{1}{E_f - E_a - i\Gamma_a/2} \right].
\end{aligned} \tag{A.26}$$

### A.2.7 BC matrix element

$$\begin{aligned}
\mathcal{M}_\omega^{BC} &= \alpha^2 \int dE' \langle E_f 00 | p_z | a \rangle \langle E' 10 | p_z | \phi_0 \rangle \times \\
&\quad \frac{V_{aE'}}{E' - E_a + i\Gamma_a/2} \frac{1}{\omega_i + \omega_{2n\pm 1} - E' + i0^+} = \\
&= \alpha^2 \int dE' \mathcal{O}_{E_f a}^S i \sqrt{\frac{4\pi}{3}} (2E')^{3/4} \phi_0(\sqrt{2E'}) \left(\frac{\Gamma_a}{2\pi}\right)^{1/2} \times \\
&\quad \frac{1}{\omega_i + \omega_{2n\pm 1} - E_a + i\Gamma_a/2} \left[ \frac{1}{\omega_i + \omega_{2n\pm 1} - E' + i0^+} + \frac{1}{E' - E_a + i\Gamma_a/2} \right] = \\
&= -\alpha^2 \mathcal{O}_{E_f a}^S i \sqrt{\frac{4\pi}{3}} (2E_f)^{3/4} \phi_0(\sqrt{2E_f}) \left(\frac{\Gamma_a}{2\pi}\right)^{1/2} \frac{2i\pi}{\omega_i + \omega_{2n\pm 1} - E_a + i\Gamma_a/2}.
\end{aligned} \tag{A.27}$$

We have introduced a new parameter in our model,  $\langle E_f \ell 0 | p_z | a \rangle = \mathcal{O}_{E_f a}^\ell$ , where the superscript denotes the symmetry of the final state.

### A.2.8 BM matrix element

$$\begin{aligned}
\mathcal{M}_\omega^{BM} &= \alpha^2 \int dE' \int d\epsilon' \langle E_f 00 | p_z | a \rangle \langle \epsilon' 10 | p_z | \phi_0 \rangle \times \\
&\quad \frac{V_{a\epsilon'}}{E' - \epsilon' - i0^+} \frac{V_{aE'}}{E' - E_a - i\Gamma_a/2} \frac{V_{aE'}}{E' - E_a + i\Gamma_a/2} \frac{1}{\omega_i + \omega_{2n\pm 1} - E' + i0^+} = \\
&= \alpha^2 \mathcal{O}_{E_f a}^S i \sqrt{\frac{4\pi}{3}} \left(\frac{\Gamma_a}{2\pi}\right)^{3/2} \int dE' \int d\epsilon' (2\epsilon')^{3/4} \phi_0(\epsilon') \times \\
&\quad \frac{1}{E' - \epsilon' - i0^+} \frac{1}{E' - E_a - i\Gamma_a/2} \frac{1}{E' - E_a + i\Gamma_a/2} \frac{1}{\omega_i + \omega_{2n\pm 1} - E' + i0^+}.
\end{aligned} \tag{A.28}$$

Rewriting again the distribution in  $\epsilon'$  as principal part and delta,

$$\begin{aligned}
\mathcal{M}_\omega^{BM} &= \alpha^2 \mathcal{O}_{E_f a}^S i \sqrt{\frac{4\pi}{3}} \left(\frac{\Gamma_a}{2\pi}\right)^{3/2} \int dE' \left( \Delta_{PP}(E') + i\pi (2E')^{3/4} \phi_0(\sqrt{2E'}) \right) \times \\
&\quad \frac{1}{E' - E_a - i\Gamma_a/2} \frac{1}{E' - E_a + i\Gamma_a/2} \frac{1}{\omega_i + \omega_{2n\pm 1} - E' + i0^+}.
\end{aligned} \tag{A.29}$$

We are left to calculate the product of the three distributions

$$\begin{aligned}
& \frac{1}{E' - E_a - i\Gamma_a/2} \frac{1}{E' - E_a + i\Gamma_a/2} \frac{1}{\omega_i + \omega_{2n\pm 1} - E' + i0^+} = \\
& = \frac{1}{E' - E_a - i\Gamma_a/2} \left[ \frac{1}{\omega_i + \omega_{2n\pm 1} - E_a + i\Gamma_a/2} \left( \frac{1}{\omega_i + \omega_{2n\pm 1} - E' + i0^+} + \frac{1}{E' - E_a + i\Gamma_a/2} \right) \right] = \\
& = \frac{1}{\omega_i + \omega_{2n\pm 1} - E_a + i\Gamma_a/2} \left[ \frac{1}{\omega_i + \omega_{2n\pm 1} - E_a - i\Gamma_a/2} \underbrace{\left( \frac{1}{\omega - E' + i0^+} + \frac{1}{E' - E_a - i\Gamma_a/2} \right)}_{\approx 0} \right] - \\
& \frac{1}{-i\Gamma_a} \underbrace{\left( \frac{1}{E_a - E' - i\Gamma_a/2} + \frac{1}{E' - E_a - i\Gamma_a/2} \right)}_{\approx 2i\pi} = \\
& = \frac{2\pi}{\Gamma_a} \frac{\delta(E' - E_a)}{\omega - E_a + i\Gamma_a/2}.
\end{aligned} \tag{A.30}$$

Finally, the transition matrix element can be written as

$$\mathcal{M}_\omega^{BM} = \alpha^2 \mathcal{O}_{E_f a}^S i \sqrt{\frac{4\pi}{3}} \left( \frac{\Gamma_a}{2\pi} \right)^{1/2} \left( i\pi (2E_a)^{3/4} \phi_0(\sqrt{2E_a}) \right) \frac{1}{\omega_i + \omega_{2n\pm 1} - E_a + i\Gamma_a/2}. \tag{A.31}$$

Again, we have approximated  $\Delta_{PP}(E_a) \approx 0$ .

### A.2.9 BB matrix element

$$\begin{aligned}
\mathcal{M}_\omega^{BB} &= \alpha^2 \int dE' \langle E_f 00 | p_z | a \rangle \langle a | p_z | \phi_0 \rangle \times \\
& \frac{V_{aE'}}{E' - E_a - i\Gamma_a/2} \frac{V_{aE'}}{E' - E_a + i\Gamma_a/2} \frac{1}{\omega_i + \omega_{2n\pm 1} - E' + i0^+} = \\
& = \alpha^2 \mathcal{O}_{E_f a}^S \mathcal{O}_{ai} \left( \frac{\Gamma_a}{2\pi} \right) \times \\
& \int dE' \frac{1}{E' - E_a - i\Gamma_a/2} \frac{1}{E' - E_a + i\Gamma_a/2} \frac{1}{\omega_i + \omega_{2n\pm 1} - E' + i0^+}.
\end{aligned} \tag{A.32}$$

The distributions are the same as in the *BM* case,

$$\mathcal{M}_\omega^{BB} = \alpha^2 \mathcal{O}_{E_f a}^S \mathcal{O}_{ai} \frac{1}{\omega_i + \omega_{2n\pm 1} - E_a + i\Gamma_a/2}. \tag{A.33}$$

# Bibliography

- [1] A. Einstein. On a Heuristic Point of View about the Creation and Conversion of Light. *Annalen der Physik*, 17:132–148, 1905.
- [2] Synchrotron Soleil. URL <http://www.synchrotron-soleil.fr/portal/page/portal/SourceAccelérateur>.
- [3] A. Eppink and D.H. Parker. Velocity map imaging of ions and electrons using electrostatic lenses: Application in photoelectron and photofragment ion imaging of molecular oxygen. *Rev.Sci.Instrum.*, 68(9), 1997.
- [4] J Ullrich, R Moshhammer, a Dorn, R D rner, L Ph H Schmidt, and H Schmidt-B cking. Recoil-ion and electron momentum spectroscopy: reaction-microscopes. *Reports on Progress in Physics*, 66(9):1463–1545, September 2003. ISSN 0034-4885. doi: 10.1088/0034-4885/66/9/203. URL <http://stacks.iop.org/0034-4885/66/i=9/a=203?key=crossref.4f0ed0c11253bbad6096727290d95871>.
- [5] P. O’Keeffe, V. Feyer, P. Bolognesi, M. Coreno, C. Callegari, G. Cautero, a. Moise, K.C. Prince, R. Richter, R. Sergo, M. Alagia, M. de Simone, a. Kivimäki, M. Devetta, T. Mazza, P. Piseri, V. Lyamayev, R. Katzy, F. Stienkemeier, Y. Ovcharenko, T. Möller, and L. Avaldi. A velocity map imaging apparatus for gas phase studies at FERMI@Elettra. *Nuclear Instruments and Methods in Physics Research Section B: Beam Interactions with Materials and Atoms*, 284:69–73, August 2012. ISSN 0168583X. doi: 10.1016/j.nimb.2011.07.020. URL <http://linkinghub.elsevier.com/retrieve/pii/S0168583X11006641>.
- [6] A. Matsuda, M. Fushitani, C. Tseng, Y. Hikosaka, J. Eland, and A. Hishikawa. A magnetic-bottle multi-electron-ion coincidence spectrometer. *Rev.Sci.Instrum.*, 82(10):103–105, 2011.
- [7] H.D. Cohen and U. Fano. Interference in the Photo-Ionization of Molecules. *Phys. Rev.*, 150(1), 1966.
- [8] Sophie E Canton, Etienne Plésiat, John D Bozek, Bruce S Rude, Piero Decleva, and Fernando Martín. Direct observation of Young’s double-slit interferences in

- vibrationally resolved photoionization of diatomic molecules. *Proceedings of the National Academy of Sciences of the United States of America*, 108(18):7302–6, May 2011. ISSN 1091-6490. doi: 10.1073/pnas.1018534108. URL <http://www.ncbi.nlm.nih.gov/pubmed/21498686>.
- [9] Etienne Plésiat, Luca Argenti, Edwin Kukk, Catalin Miron, Kiyoshi Ueda, Piero Decleva, and Fernando Martín. Intramolecular electron diffraction in vibrationally resolved K-shell photoionization of methane. *Physical Review A*, 85(2):023409, February 2012. ISSN 1050-2947. doi: 10.1103/PhysRevA.85.023409. URL <http://link.aps.org/doi/10.1103/PhysRevA.85.023409>.
- [10] K Ueda, C Miron, L Argenti, M Patanen, K Kooser, D Ayuso, S Mondal, M Kimura, K Sakai, O Travnikova, A Palacios, P Decleva, E Kukk, and F Martín. The fingerprint of molecular structure in vibrationally resolved photoelectron spectra. *To be published*, 2013.
- [11] Ferenc Krausz and Misha Ivanov. Attosecond physics. *Rev. Mod. Phys.*, 81(1):163–234, February 2009. ISSN 0034-6861. doi: 10.1103/RevModPhys.81.163. URL <http://link.aps.org/doi/10.1103/RevModPhys.81.163>.
- [12] P F Moulton. Spectroscopic and laser characteristics of Ti:A1 2 0 3. *J.Opt.Soc.Am.B*, 3(1):125–133, 1986.
- [13] P.A. Franken, A.E. Hill, C.W. Peters, and G. Weinreich. Generation of optical harmonics. *Phys.Rev.Lett.*, 7(1):118–120, 1961.
- [14] P. B. Corkum. Plasma Perspective on Strong-Field Multiphoton Ionization. *Phys. Rev. Lett.*, 71(13):1994–1997, 1993.
- [15] R. Kienberger, E. Goulielmakis, M. Uiberacker, A. Baltuska, V. Yakovlev, F. Bammer, A. Scrinzi, Th. Westerwalbesloh, U. Kleineberg, U Heinzmann, M Drescher, and F. Krausz. Atomic transient recorder. *Nature*, 427:817–821, 2004.
- [16] E Goulielmakis, M Schultze, M Hofstetter, V S Yakovlev, J Gagnon, M Uiberacker, a L Aquila, E M Gullikson, D T Attwood, R Kienberger, F Krausz, and U Kleineberg. Single-cycle nonlinear optics. *Science*, 320(5883):1614–7, June 2008. ISSN 1095-9203. doi: 10.1126/science.1157846. URL <http://www.ncbi.nlm.nih.gov/pubmed/18566281>.
- [17] G Sansone, E Benedetti, F Calegari, C Vozzi, L Avaldi, R Flammini, L Poletto, P Villoresi, C Altucci, R Velotta, S Stagira, S De Silvestri, and M Nisoli. Isolated single-cycle attosecond pulses. *Science*, 314(5798):443–6, October 2006. ISSN 1095-9203. doi: 10.1126/science.1132838. URL <http://www.ncbi.nlm.nih.gov/pubmed/17053142>.

- [18] S. Haessler, J. Caillat, W. Boutu, C. Giovanetti-Teixeira, T. Ruchon, T. Auguste, Z. Diveki, P. Breger, a. Maquet, B. Carré, R. Taïeb, and P. Salières. Attosecond imaging of molecular electronic wavepackets. *Nature Physics*, 6(3):200–206, January 2010. ISSN 1745-2473. doi: 10.1038/nphys1511. URL <http://www.nature.com/doifinder/10.1038/nphys1511>.
- [19] M Uiberacker, Th. Uphues, M Schultze, A J Verhoef, V Yakovlev, M F Kling, J Rauschenberger, N M Kabachnik, H Schroder, M Lezius, K L Kompa, H.-G. Muller, M J J Vrakking, S Hendel, U Kleineberg, U Heinzmann, M Drescher, and F Krausz. Attosecond real-time observation of electron tunnelling in atoms. *Nature*, 446(7136):627–632, April 2007. ISSN 0028-0836. URL <http://dx.doi.org/10.1038/nature05648>[http://www.nature.com/nature/journal/v446/n7136/supinfo/nature05648\\_S1.html](http://www.nature.com/nature/journal/v446/n7136/supinfo/nature05648_S1.html).
- [20] M Drescher, M Hentschel, R Kienberger, M Uiberacker, V Yakovlev, a Scrinzi, Th Westerwalbesloh, U Kleineberg, U Heinzmann, and F Krausz. Time-resolved atomic inner-shell spectroscopy. *Nature*, 419(6909):803–7, October 2002. ISSN 0028-0836. doi: 10.1038/nature01143. URL <http://www.ncbi.nlm.nih.gov/pubmed/12397349>.
- [21] Eleftherios Goulielmakis, Zhi-Heng Loh, Adrian Wirth, Robin Santra, Nina Rohringer, Vladislav S. Yakovlev, Sergey Zherebtsov, Thomas Pfeifer, Abdallah M. Azzeer, Matthias F. Kling, Stephen R. Leone, and Ferenc Krausz. Real-time observation of valence electron motion. *Nature*, 466(7307):739–743, August 2010. ISSN 0028-0836. doi: 10.1038/nature09212. URL <http://www.nature.com/doifinder/10.1038/nature09212>.
- [22] T. Remetter, P. Johnsson, J. Mauritsson, K. Varjú, Y. Ni, F. Lépine, E. Gustafsson, M. Kling, J. Khan, R. López-Martens, K. J. Schafer, M. J. J. Vrakking, and a. LHuillier. Attosecond electron wave packet interferometry. *Nature Physics*, 2(5):323–326, April 2006. ISSN 1745-2473. doi: 10.1038/nphys290. URL <http://www.nature.com/doifinder/10.1038/nphys290>.
- [23] J. Mauritsson, P. Johnsson, E. Mansten, M. Swoboda, T. Ruchon, A. LHuillier, and K. Schafer. Coherent Electron Scattering Captured by an Attosecond Quantum Stroboscope. *Phys. Rev. Lett.*, 100(7):073003, February 2008. ISSN 0031-9007. doi: 10.1103/PhysRevLett.100.073003. URL <http://link.aps.org/doi/10.1103/PhysRevLett.100.073003>.
- [24] R. Trebino, K.W. DeLong, D.N. Fittinghoff, J.N. Sweetser, M.A. Krumbügel, B.A. Richman, and D.J. Kane. Measuring ultrashort laser pulses in the time-frequency

- domain using frequency-resolved optical gating. *Rev.Sci.Instrum.*, 68(9):3277–3295, 1997.
- [25] P M Paul, E S Toma, P Breger, G Mullot, F Auge, P Balcou, H G Muller, and P Agostini. Observation of a train of attosecond pulses from high harmonic generation. *Science (New York, N.Y.)*, 292(5522):1689–92, June 2001. ISSN 0036-8075. doi: 10.1126/science.1059413. URL <http://www.ncbi.nlm.nih.gov/pubmed/11387467>.
- [26] F. Faisal. *Theory of Multiphoton Processes*. Springer, 1987. ISBN 978-0306423178.
- [27] R. López-Martens, J. Mauritsson, P. Johnsson, K. Varjú, a. LHuillier, W. Kornelis, J. Biegert, U. Keller, M. Gaarde, and K. Schafer. Characterization of high-order harmonic radiation on femtosecond and attosecond time scales. *Applied Physics B*, 78(7-8):835–840, April 2004. ISSN 0946-2171. doi: 10.1007/s00340-004-1485-7. URL <http://link.springer.com/10.1007/s00340-004-1485-7>.
- [28] Rodrigo López-Martens, Katalin Varjú, Per Johnsson, Johan Mauritsson, Yann Mairesse, Pascal Salières, Mette B. Gaarde, Kenneth J. Schafer, Anders Persson, Sune Svanberg, Claes-Göran Wahlström, and Anne L’Huillier. Amplitude and Phase Control of Attosecond Light Pulses. *Phys. Rev. Lett.*, 94:033001, 2005. doi: 10.1103/PhysRevLett.94.033001.
- [29] Johan Mauritsson, Mette Gaarde, and Kenneth Schafer. Accessing properties of electron wave packets generated by attosecond pulse trains through time-dependent calculations. *Physical Review A*, 72(1):013401, July 2005. ISSN 1050-2947. doi: 10.1103/PhysRevA.72.013401. URL <http://link.aps.org/doi/10.1103/PhysRevA.72.013401>.
- [30] Y Mairesse, a de Bohan, L J Frasinski, H Merdji, L C Dinu, P Monchicourt, P Breger, M Kovacev, R Taïeb, B Carré, H G Muller, P Agostini, and P Salières. Attosecond synchronization of high-harmonic soft x-rays. *Science (New York, N.Y.)*, 302(5650):1540–3, November 2003. ISSN 1095-9203. doi: 10.1126/science.1090277. URL <http://www.ncbi.nlm.nih.gov/pubmed/14645841>.
- [31] J Mauritsson, J M Dahlström, E Mansten, and T Fordell. Sub-cycle control of attosecond pulse generation using two-colour laser fields. *Journal of Physics B: Atomic, Molecular and Optical Physics*, 42(13):134003, July 2009. ISSN 0953-4075. doi: 10.1088/0953-4075/42/13/134003. URL <http://stacks.iop.org/0953-4075/42/i=13/a=134003?key=crossref.673b46c6bc2bcd3151b8eca9f6cc7a0d>.

- [32] M. Swoboda, T. Fordell, K. Klünder, J. M. Dahlström, M. Miranda, C. Buth, K. J. Schafer, J. Mauritsson, a. LHuillier, and M. Gisselbrecht. Phase Measurement of Resonant Two-Photon Ionization in Helium. *Phys. Rev. Lett.*, 104(10):12–15, March 2010. ISSN 0031-9007. doi: 10.1103/PhysRevLett.104.103003. URL <http://link.aps.org/doi/10.1103/PhysRevLett.104.103003>.
- [33] D. Guénot, K. Klünder, C. Arnold, D. Kroon, J. Dahlström, M. Miranda, T. Fordell, M. Gisselbrecht, P. Johnsson, J. Mauritsson, E. Lindroth, a. Maquet, R. Taïeb, a. LHuillier, and a. Kheifets. Photoemission-time-delay measurements and calculations close to the 3s-ionization-cross-section minimum in Ar. *Physical Review A*, 85(5):1–8, May 2012. ISSN 1050-2947. doi: 10.1103/PhysRevA.85.053424. URL <http://link.aps.org/doi/10.1103/PhysRevA.85.053424>.
- [34] X. Feng, S. Gilbertson, H. Mashiko, S. Khan, H. Wang, M. Chini, Y. Wu, and Z. Chang. Single Isolated Attosecond Pulses Generation with Double Optical Gating. *Chemical Physics*, 99:89–111, 2010.
- [35] Steve Gilbertson, Michael Chini, Ximao Feng, Sabih Khan, Yi Wu, and Zenghu Chang. Monitoring and Controlling the Electron Dynamics in Helium with Isolated Attosecond Pulses. *Phys. Rev. Lett.*, 105(26):1–4, December 2010. ISSN 0031-9007. doi: 10.1103/PhysRevLett.105.263003. URL <http://link.aps.org/doi/10.1103/PhysRevLett.105.263003>.
- [36] Ahmed H Zewail. Four-dimensional electron microscopy. *Science (New York, N.Y.)*, 328(5975):187–93, April 2010. ISSN 1095-9203. doi: 10.1126/science.1166135. URL <http://www.ncbi.nlm.nih.gov/pubmed/20378810>.
- [37] A. Vredenburg, C.S. Lehmann, D. Irimia, W.G. Roeterdink, and M.H.M. Janssen. The Reaction Microscope: Imaging and Pulse Shaping Control in Photodynamics. *Chem.Phys.Chem.*, 12, 2011.
- [38] Rajdeep Saha and Victor S Batista. Tunneling under coherent control by sequences of unitary pulses. *The journal of physical chemistry. B*, 115(18):5234–42, May 2011. ISSN 1520-5207. doi: 10.1021/jp108331x. URL <http://www.ncbi.nlm.nih.gov/pubmed/21384933>.
- [39] R. Madden and K. Codling. New autoionizing atomic energy levels in He, Ne and Ar. *Phys. Rev. Lett.*, 1963.
- [40] U. Fano. Sullo spettro di assorbimento dei gas nobili presso il limite dello spettro d’arco. *Nuovo Cimento*, 12:154–161, 1935.
- [41] U. Fano. Effects of configuration interaction on intensities and phase shifts. *Phys. Rev.*, 124:1866, 1961.

- [42] P. Lambropoulos and P. Zöller. Autoionizing states in strong laser fields. *Phys. Rev. A*, 24(1), 1981.
- [43] Eugene Wigner. Lower Limit for the Energy Derivative of the Scattering Phase Shift. *Physical Review*, 98(1):145–147, April 1955. ISSN 0031-899X. doi: 10.1103/PhysRev.98.145. URL <http://link.aps.org/doi/10.1103/PhysRev.98.145>.
- [44] M. Schultze, M. Fiess, N. Karpowicz, J. Gagnon, M. Korbman, M. Hofstetter, S. Neppl, a. L. Cavalieri, Y. Komninos, T. Mercouris, C. a. Nicolaides, R. Pazourek, S. Nagele, J. Feist, J. Burgdorfer, a. M. Azzeer, R. Ernstorfer, R. Kienberger, U. Kleineberg, E. Goulielmakis, F. Krausz, and V. S. Yakovlev. Delay in Photoemission. *Science*, 328(5986):1658–1662, June 2010. ISSN 0036-8075. doi: 10.1126/science.1189401. URL <http://www.sciencemag.org/cgi/doi/10.1126/science.1189401>.
- [45] J. Breidbach and L. Cederbaum. Universal Attosecond Response to the Removal of an Electron. *Physical Review Letters*, 94(3):033901, January 2005. ISSN 0031-9007. doi: 10.1103/PhysRevLett.94.033901. URL <http://link.aps.org/doi/10.1103/PhysRevLett.94.033901>.
- [46] Felix T. Smith. Lifetime Matrix in Collision Theory. *Physical Review*, 118(1), 1960.
- [47] N. Kelkar and M. Nowakowski. Analysis of averaged multichannel delay times. *Physical Review A*, 78(1):012709, July 2008. ISSN 1050-2947. doi: 10.1103/PhysRevA.78.012709. URL <http://link.aps.org/doi/10.1103/PhysRevA.78.012709>.
- [48] J M Dahlström, a LHuillier, and a Maquet. Introduction to attosecond delays in photoionization. *Journal of Physics B: Atomic, Molecular and Optical Physics*, 45(18):183001, September 2012. ISSN 0953-4075. doi: 10.1088/0953-4075/45/18/183001. URL <http://stacks.iop.org/0953-4075/45/i=18/a=183001?key=crossref.c064b9e1f1761bc7e34faada211145d5>.
- [49] L. R. Moore, M. a. Lysaght, J. S. Parker, H. W. van der Hart, and K. T. Taylor. Time delay between photoemission from the 2p and 2s subshells of neon. *Physical Review A*, 84(6):061404, December 2011. ISSN 1050-2947. doi: 10.1103/PhysRevA.84.061404. URL <http://link.aps.org/doi/10.1103/PhysRevA.84.061404>.
- [50] Suren Sukiasyan, Kenichi L. Ishikawa, and Misha Ivanov. Attosecond cascades and time delays in one-electron photoionization. *Physical Review A*, 86(3):033423, September 2012. ISSN 1050-2947. doi: 10.1103/PhysRevA.86.033423. URL <http://link.aps.org/doi/10.1103/PhysRevA.86.033423>.

- [51] Renate Pazourek, Johannes Feist, Stefan Nagele, and Joachim Burgdörfer. Attosecond Streaking of Correlated Two-Electron Transitions in Helium. *Physical Review Letters*, 108(16):163001, April 2012. ISSN 0031-9007. doi: 10.1103/PhysRevLett.108.163001. URL <http://link.aps.org/doi/10.1103/PhysRevLett.108.163001>.
- [52] S Nagele, R Pazourek, J Feist, K Doblhoff-Dier, C Lemell, K Tkési, and J Burgdörfer. Time-resolved photoemission by attosecond streaking: extraction of time information. *Journal of Physics B: Atomic, Molecular and Optical Physics*, 44(8):081001, April 2011. ISSN 0953-4075. doi: 10.1088/0953-4075/44/8/081001. URL <http://stacks.iop.org/0953-4075/44/i=8/a=081001?key=crossref.c56d1467cb7f685278df1f53ffd231b7>.
- [53] Luca Argenti and Eva Lindroth. Ionization Branching Ratio Control with a Resonance Attosecond Clock. *Phys. Rev. Lett.*, 105(5):053002, July 2010. ISSN 0031-9007. doi: 10.1103/PhysRevLett.105.053002. URL <http://link.aps.org/doi/10.1103/PhysRevLett.105.053002>.
- [54] Alfred Maquet and Richard Taïeb. Two-colour IR + XUV spectroscopies: the soft-photon approximation. *Journal of Modern Optics*, 54(13-15):1847–1857, September 2007. ISSN 0950-0340. doi: 10.1080/09500340701306751. URL <http://www.tandfonline.com/doi/abs/10.1080/09500340701306751>.
- [55] *Springer Handbook of Atomic, Molecular and Optical Physics*. 2006. ISBN 978-0-387-33634-3.
- [56] J.W. Cooper, U. Fano, and F. Prats. Classification of two-electron excitation levels of helium. *Phys. Rev. Lett.*, 10(12):10–13, 1963.
- [57] C.D. Lin. Classification of doubly excited states of two-electron atoms. *Phys. Rev. Lett.*, 51, 1983.
- [58] D.A. Varshalovich. *Quantum Theory of Angular Momentum*. World Scientific, 1988. ISBN 978-9971501075.
- [59] H. Bachau, E. Cormier, P. Decleva, J.E. Hansen, and F. Martín. Applications of B-splines in atomic and molecular physics. *Rep. Prog. Phys.*, 1815, 2001.
- [60] R.G. Newton. *Scattering Theory of Waves and Particles*. Dover Publications, 1982. ISBN 978-0486425351.
- [61] J.D. Jackson. *Classical Electrodynamics*. John Wiley & Sons, 1962. ISBN 978-0471309321.

- [62] B.H. Bransden and C.J. Joachain. *Physics of Atoms and Molecules*. Prentice Hall, 1983. ISBN 978-0582356924.
- [63] A. Messiah. *Quantum Mechanics*. 1958. ISBN 9780486409245.
- [64] F Ferrari, F Calegari, M Lucchini, C Vozzi, Salvatore Stagira, Giuseppe Sansone, and Mauro Nisoli. High-energy isolated attosecond pulses generated by above-saturation few-cycle fields. *Nature Photonics*, (AOL):1–5, 2010. doi: 10.1038/NPHOTON.2010.250. URL <http://dx.doi.org/10.1038/nphoton.2010.250>.
- [65] M Lewenstein, Philippe Balcou, Misha Yu. Ivanov, Anne L’Huillier, and Paul B. Corkum. Theory of high-harmonic generation by low-frequency laser fields. *Phys. Rev. A*, 49(3):2117, 1994.
- [66] Giuseppe Sansone, F. Kelkensberg, J. F. Pérez-Torres, Felipe Morales, Matthias F. Kling, W. Siu, Omair Ghafur, Per Johnsson, Marko Swoboda, E. Benedetti, F. Ferrari, F. Lépine, José Luis Sanz-Vicario, Sergey Zherebtsov, I. Znakovskaya, Anne L’huillier, Misha Yu. Ivanov, Mauro Nisoli, Fernando Martín, and Marc J. J. Vrakking. Electron localization following attosecond molecular photoionization. *Nature*, 465(7299):763, June 2010. ISSN 0028-0836. doi: 10.1038/nature09084. URL <http://www.nature.com/doifinder/10.1038/nature09084><http://www.ncbi.nlm.nih.gov/pubmed/20535207>.
- [67] M. Schultze, Markus Fiess, N. Karpowicz, Justin Gagnon, M. Korbman, M. Hofstetter, S. Neppl, A. L. Cavalieri, Yannis Komninos, Theodoros Mercouris, Cleanthes A. Nicolaides, Renate Pazourek, Stefan Nagele, Johannes Feist, Joachim Burgdörfer, Abdallah M. Azzeer, R. Ernstorfer, Reinhard Kienberger, Ulf Kleineberg, Eleftherios Goulielmakis, Ferenc Krausz, and Vladislav S. Yakovlev. Delay in photoemission. *Science*, 328:1658, 2010.
- [68] F. Kelkensberg, W. Siu, J. F. Pérez-Torres, Felipe Morales, G. Gademann, Arnaud Rouzée, Per Johnsson, M. Lucchini, F. Calegari, José Luis Sanz-Vicario, Fernando Martín, and Marc J. J. Vrakking. Attosecond Control in Photoionization of Hydrogen Molecules. *Phys. Rev. Lett.*, 107(4):043002, July 2011. ISSN 0031-9007. doi: 10.1103/PhysRevLett.107.043002. URL <http://link.aps.org/doi/10.1103/PhysRevLett.107.043002>.
- [69] L V Keldysh. Ionization in the field of a strong electromagnetic wave. *JETP*, 20(5):1307–1314, 1965.
- [70] Farhad H. M. Faisal. Multiple absorption of laser photons by atoms. *J. Phys. B: At. Mol. Opt. Phys.*, 6:L89, 1973.

- [71] Howard R. Reiss. Effect of an intense electromagnetic field on a weakly bound system. *Phys. Rev. A*, 22(5):1786, 1980.
- [72] Maciej Lewenstein, Pascal Salieres, and Anne L’Huillier. Phase of the atomic polarization in high-order harmonic generation. *Phys. Rev. A*, 52(6):4747–4754, 1995.
- [73] Lars Bojer Madsen. Strong-field approximation in laser-assisted dynamics. *Am. J. Phys.*, 73(1):57, 2005. ISSN 00029505. doi: 10.1119/1.1796791. URL <http://link.aip.org/link/AJPIAS/v73/i1/p57/s1&Agg=doi>.
- [74] Farhad H. M. Faisal. *Theory of multiphoton processes*. Plenum Press, New York, 1987.
- [75] Alfred Maquet and Richard Taïeb. Two-colour IR + XUV spectroscopies: the ”soft-photon approximation”. *J. Mod. Opt.*, 54(13-15):1847–1857, September 2007. ISSN 0950-0340. doi: 10.1080/09500340701306751. URL <http://www.tandfonline.com/doi/abs/10.1080/09500340701306751>.
- [76] Aurelia Cionga, Viorica Florescu, Alfred Maquet, Richard Taïeb, and Richard Taieb. Target dressing effects in laser-assisted x-ray photoionization. *Phys. Rev. A*, 47(3):1830, 1993.
- [77] Chang-Hua Zhang and Uwe Thumm. Electron-ion interaction effects in attosecond time-resolved photoelectron spectra. *Phys. Rev. A*, 82:043405, 2010. doi: 10.1103/PhysRevA.82.043405.
- [78] Milton Abramowitz and Irene A. Stegun. *Handbook of Mathematical Functions with Formulas, Graphs, and Mathematical Tables*. Dover Publications, Inc., New York, 1965. doi: 10.1119/1.15378. URL <http://link.aip.org/link/?AJP/56/958/4&Agg=doi>.
- [79] M. Swoboda, J.M. Dahlström, T. Ruchon, J. Mauritsson, A. L’Huillier, and K. J. Schafer. Intensity dependence of two-color laser-assisted photoionization spectra. *Laser Physics*, 19:1591–1599, 2009.
- [80] Katalin Varjú, Per Johnsson, Johan Mauritsson, T. Remetter, Thierry Ruchon, Y Ni, F. Lépine, Matthias F. Kling, J. I. Khan, Kenneth J. Schafer, Marc J. J. Vrakking, and Anne L’Huillier. Angularly resolved electron wave packet interferences. *J. Phys. B: At. Mol. Opt. Phys.*, 39:3983, 2006. doi: 10.1088/0953-4075/39/18/026.
- [81] P Radcliffe, M Arbeiter, W B Li, S Düsterer, H Redlin, P Hayden, P Hough, V Richardson, J T Costello, T Fennel, and M Meyer. Atomic photoionization in combined intense XUV free-electron and infrared laser fields. *New Journal*

- of Physics*, 14(4):043008, April 2012. ISSN 1367-2630. doi: 10.1088/1367-2630/14/4/043008. URL <http://stacks.iop.org/1367-2630/14/i=4/a=043008?key=crossref.8018ae46abb817a2319ab327fb94e8e1>.
- [82] A. K. Kazansky, I. P. Sazhina, and N. M. Kabachnik. Angle-resolved electron spectra in short-pulse two-color XUV+IR photoionization of atoms. *Phys. Rev. A*, 82(3):033420, September 2010. ISSN 1050-2947. doi: 10.1103/PhysRevA.82.033420. URL <http://link.aps.org/doi/10.1103/PhysRevA.82.033420>.
- [83] Marc J. J. Vrakking. An iterative procedure for the inversion of two-dimensional ion/photoelectron imaging experiments. *Rev. Sci. Instrum.*, 72:4084, 2001.
- [84] A. Kazansky, I. Sazhina, and N. Kabachnik. Angle-resolved electron spectra in short-pulse two-color XUV+IR photoionization of atoms. *Physical Review A*, 82(3):1–8, September 2010. ISSN 1050-2947. doi: 10.1103/PhysRevA.82.033420. URL <http://link.aps.org/doi/10.1103/PhysRevA.82.033420>.
- [85] O Guyétand, M. Gisselbrecht, a Huetz, Pierre Agostini, Richard Taïeb, Valérie Véniard, Alfred Maquet, L Antonucci, O Boyko, C. Valentin, and D Douillet. Multicolour above-threshold ionization of helium: quantum interference effects in angular distributions. *J. Phys. B: At. Mol. Opt. Phys.*, 38(22):L357–L363, November 2005. ISSN 0953-4075. doi: 10.1088/0953-4075/38/22/L01. URL <http://stacks.iop.org/0953-4075/38/i=22/a=L01?key=crossref.0735ab958087e900a7134ada62354623>.
- [86] O Guyétand, M Gisselbrecht, a Huetz, P Agostini, R Taïeb, Alfred Maquet, B Carré, P Breger, O Gobert, D Garzella, J-F Hergott, O Tcherbakoff, H Merdji, M Bougeard, H Rottke, M Böttcher, Z Ansari, and P Antoine. Evolution of angular distributions in two-colour, few-photon ionization of helium. *J. Phys. B: At. Mol. Opt. Phys.*, 41(5):051002, March 2008. ISSN 0953-4075. doi: 10.1088/0953-4075/41/5/051002. URL <http://stacks.iop.org/0953-4075/41/i=5/a=051002?key=crossref.c23adee4c160f24bedb8bbaa248cee5f>.
- [87] Jérémie Caillat, Alfred Maquet, Stefan Haessler, Baptiste Fabre, Thierry Ruchon, Pascal Salières, Yann Mairesse, and Richard Taïeb. Attosecond Resolved Electron Release in Two-Color Near-Threshold Photoionization of N<sub>2</sub>. *Phys. Rev. Lett.*, 106:093002, 2011. doi: 10.1103/PhysRevLett.106.093002.
- [88] J.M. Rost, K. Schultz, M. Domke, and G. Kaindl. Resonance parameters of photo doubly excited helium. *J. Phys. B: At. Mol. Opt. Phys.*, 4663, 1997.
- [89] E. Lindroth. Calculation of doubly excited states of helium with a finite discrete spectrum. *Physical Review A*, 49(6), 1994.

- 
- [90] A. Jiménez, L. Argenti, and F. Martín. Strong field effects in IR-laser-assisted atomic ionization induced by XUV attosecond-pulse trains. *Submitted.*, 2013.
- [91] C. Ott, A. Kaldun, P. Raith, K. Meyer, M. Laux, J. Evers, C.H. Keitel, C.H. Greene, and T. Pfeifer. Lorentz Meets Fano in Spectral Line Shapes: A Universal Phase and Its Laser Control. *Science*, 340:716–720, 2013.